UNIVERSITY OF SOUTHAMPTON

FACULTY OF PHYSICAL SCIENCES AND ENGINEERING

Optoelectronics Research Centre

Nonlinear Properties of Optical Microfibres

by

Timothy Lee

Supervisor: Dr Gilberto Brambilla

Thesis for the degree of Doctor of Philosophy

Internal Examiner: Prof. James S. Wilkinson
External Examiner: Prof. Philippe Grelu

July 2013

ABSTRACT

Glass microfibre waveguides offer an intriguing platform for the investigation of nonlinear effects, due to their high effective nonlinearity which arises from the tight modal confinement down to dimensions comparable to the wavelength of guided light. This thesis presents theoretical and experimental work towards achieving efficient third and second harmonic generation in silica microfibres, as well as in microfibre loop resonators for enhancing the conversion. Since microfibre resonators themselves exhibit interesting nonlinear behaviour, the polarisation dependent properties of microcoil resonators were also studied.

Efficient third harmonic generation is possible through intermodal phase matching, and experiments using short tapers have demonstrated significant efficiencies up to 10^{-3} over a uniform 4 mm waist. On the other hand, the interrogation of longer tapers, in which the harmonic generation occurs within the taper transition regions of several cm rather than the waist, allows for a broadband conversion observed to exceed 36 nm at the 5 dB bandwidth level. A straightforward technique to improve efficiency using microfibre loop resonators was also investigated. Near resonance, the recirculation of the pump power inside the resonator was experimentally shown to increase conversion by 7.7 dB higher than that of the straight microfibre, similar to simulated predictions, and by optimising the loop geometry the resonant efficiency enhancement can potentially reach 20 dB.

Simulations on second harmonic generation in microfibres indicate that the second order nonlinearity originates primarily from the structural anisotropy at the glass-air boundary (which exploits the high surface electric field strength of microfibres) as well as multipolar effects within the bulk. To overcome the inherent weakness of these effects, experiments focused on conversion enhancement via the aforementioned technique using loop resonators, with a measured 7.6 dB efficiency improvement.

In addition, an accurate polarisation dependent model for microcoils was developed for both the linear and nonlinear regimes by incorporating the effects of fibre twist and birefringence. The coupling between orthogonally polarised modes propagating along the microcoil results in a strongly polarisation sensitive transmission, especially near resonances, which in turn influences the nonlinear hysteresis characteristics.

Contents

List of Figures

List of Tables

Declaration of Authorship

I, Timothy Lee, declare that the thesis entitled *Nonlinear Properties of Optical Microfibres* and the work presented in the thesis are both my own, and have been generated by me as the result of my own original research. I confirm that:

- this work was done wholly or mainly while in candidature for a research degree at this University;
- where any part of this thesis has previously been submitted for a degree or any other qualification at this University or any other institution, this has been clearly stated;
- where I have consulted the published work of others, this is always clearly attributed;
- where I have quoted from the work of others, the source is always given. With the exception of such quotations, this thesis is entirely my own work;
- I have acknowledged all main sources of help;
- where the thesis is based on work done by myself jointly with others, I have made clear exactly what was done by others and what I have contributed myself;
- parts of this work have been published as: [1, 2, 3, 4, 5, 6, 7, 8]

Signed:.....

Date:.....

Acknowledgements

Over the course of my studies at Southampton University, I am extremely grateful to have met a number of individuals who have assisted me throughout the years.

Firstly, I would like to thank my supervisor, Gilberto Brambilla, for the trust he put in me as well as his technical and moral support. His advice and knowledge have proven invaluable time and again. I am also grateful to Neil G. R. Broderick, who co-supervised me in the early years of the Ph.D. and continued to provide excellent advice after his departure to sunnier climes. Neil also taught me much of my optics knowledge, during my undergraduate study.

Within our microfibres research group, there are many whom I would like to acknowledge. In no particular order, I am grateful to Yongmin Jung, who taught me the skills of taper fabrication and assisted me with experiments when I first began. I am especially thankful to Rand Ismaeel and Marcelo A. Gouveia, who helped fabricate many, many microfibres and resonators for the harmonic generation experiments on which we collaborated, and also Ming Ding, who provided scanning electron microscope imaging. I am also fortunate to have had the chance to undertake experiments and work closely with George Chen, on microcoil experiments, and Pengfei Wang, on several microsphere projects. Together with M. Imran M. Abdul Khudus, we formed a microfibre research group which I feel lucky to have been a part of, and their friendship is something which I will not forget.

Also, I would like to express my gratitude to Christophe A. Codemard, Shaif-ul Alam and Johan Nilsson, who generously lent me equipment for the high power source, as well as Kotya Karapetyan, for useful collaborations and discussions on both the theoretical and experimental aspects of third harmonic generation. For financial support, I acknowledge the Optoelectronics Research Centre (ORC) who provided a generous scholarship.

Finally, I am indebted to my family and friends, for their encouragement and companionship.

Nomenclature

Abbreviations

AOM	Acousto-optic modulator
ASE	Amplified spontaneous emission
EDFA	Erbium doped fibre amplifier
EOM	Electro-optic modulator
EVE	Eigenvalue equation
FSR	Free spectral range
FWHM	Full-width at half-maximum (linewidth)
FWM	Four wave mixing
GVD	Group velocity dispersion
IR	Infrared
LP	Linearly polarised (mode)
ODE	Ordinary differential equation
OM	Optical microfibre
OMR	Optical microcoil resonator
ORC	Optoelectronics Research Centre
OSA	Optical spectrum analyser
OTHG	One-third harmonic generation
RK	Runge-Kutta
SHG	Second harmonic generation
SMF	Single mode fibre
SPM	Self-phase modulation
SVEA	Slowly varying envelope approximation
TE	Transverse electric (mode)
THG	Third harmonic generation
TM	Transverse magnetic (mode)
TLS	Tunable laser source/seed
UV	Ultraviolet
XPM	Cross-phase modulation

Mathematical symbols (Latin)

A	Complex field amplitude

a	Radius (e.g. of microfibre)
$\mathbf{B}$	Magnetic induction vector
c	Speed of light in vacuum
C	Curvature of microfibre (e.g. in microcoil)
D	Diameter (e.g. of microfibre, loop resonator)
$\mathbf{D}$	Electric displacement vector
$\mathbf{E}$	Electric field vector
$\mathbf{H}$	Magnetic field vector
J_i	Overlap integral (between two modes)
k	Free space propagation constant
K	Effective coupling ($K = \kappa L_c$)
L, L_0, L_c	Length; Length of loop; Coupling length
m	Radial mode-order number
n	Linear refractive index
$n^{(2)}$	Nonlinear refractive index
n_{eff}	Effective (mode) index
$\mathbf{P}$, $\mathbf{P}_{\text{NL}}$	Polarisation vector, Nonlinear polarisation vector
P, P_0, P_{circ}	Power; Input power; Circulating power (in resonator)
Q	Quality factor (of a resonance)
$\mathbf{S}$	Poynting vector
Z_0	Vacuum impedance

Mathematical symbols (Greek)

α	Optical loss (for electric field amplitude)
α_t	Microfibre diameter profile coefficient
β	Propagation constant in waveguide
γ	Effective nonlinearity (of waveguide); Bulk $\chi^{(2)}$ coefficient
δ	Bulk $\chi^{(2)}$ coefficient
$\delta\beta$	Detuning
$\delta\lambda$	Resonance detuning (difference between pump and a resonant wavelength)
ΔK	Proximity to critical coupling (for a resonator)
ϵ_0	Vacuum permittivity
ϵ_r	Relative (linear) dielectric permittivity
ζ	Enhancement in efficiency
η	Efficiency; Fraction of total power in one polarisation; Contrast ratio between transmission from two bistable states
κ	Coupling coefficient
μ_0	Permeability of free space
ν	Azimuthal mode-order number
ρ_2	Overlap integral between second harmonic mode

	and 2$^{\text{nd}}$ order nonlinear polarisation.
ρ_b, ρ_s	Bulk component, surface component of ρ_2.
τ	Torsion (twisting) of fibre
τ_h	Torsion of a helix
$\chi^{(i)}$	The i^{th} order susceptibility tensor
ω	Angular frequency

Chapter 1

Introduction

1.1 Motivation and aims

In recent years, optical microfibres (OMs) have attracted attention for a range of nonlinear applications such as supercontinuum generation [9, 10], pulse shaping [11], second harmonic generation (SHG) [12, 13, 14] and third harmonic generation (THG) [11, 14, 15, 16, 17, 18]. OMs are typically fabricated by heating and pulling optical fibres down to a diameter comparable to the wavelength, which in conjunction with the large glass-air refractive index contrast offers modal confinement as low as a few square microns for silica. The resulting taper structure shown in Fig. 1.1 consists of a narrow waist (usually with a uniform or slightly parabolic diameter profile) connected on both sides to transition regions.

For OMs fabricated from standard silica single mode fibre (SMF), the effective nonlinearity γ can be enhanced by approximately 2 orders of magnitude [1, 19]. Furthermore, the large evanescent field in the surrounding air may be easily accessed and exploited to self-couple light between different segments of the OM and thus form loop [20, 21], knot [22]

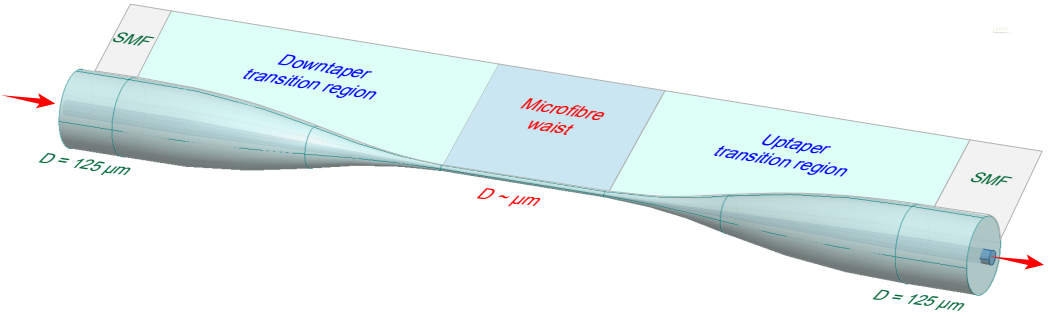

FIGURE 1.1: A schematic of a taper, showing a uniform microfibre waist region in the centre and two transition regions (the downtaper and uptaper) connected to the original untapered fibre.

and microcoil [23] resonators in which the high internal amplitudes near resonance would be ideal for reducing the input threshold powers required to observe nonlinear effects.

The fabrication of such microfibres and their resonators is relatively low-cost and straightforward compared to that of microstructured fibres or integrated micro/nano-scale waveguides and microresonators (which often involve lithographic processes), and the input and output coupling losses can be almost negligible since the light can be launched and collected by splicing the fiberised pigtails to regular fibre.

Microfibres thus serve as an excellent candidate for studying nonlinear effects, and the aim of this thesis will be to contribute to the growing body of research in three key subject areas by investigating the following nonlinear phenomena using silica microfibres:

1. *Third harmonic generation.*
2. *Second harmonic generation.*
3. *Nonlinear effects in microfibre resonators.*

A main objective of this work will be to model and investigate third harmonic generation. It is known that microfibres can be used to phase match the fundamental pump with higher order third harmonic modes at critical diameters [17], with predicted conversion efficiencies up to 80% over several cm. In practice, the surface quality of microfibres and the tapering rig fabrication tolerances would limit the achievable conversion, but the microfibre would nonetheless provide a low cost source for the third harmonic wavelength, offering an alternative to traditional frequency triplers which often rely on a two-stage conversion process. As we shall see, the use of tapers also allows for a wide conversion bandwidth.

The second goal is to study second harmonic generation in the silica microfibre. Whilst SHG in an isotropic glass is usually assumed to be impossible owing to the centrosymmetric structure, the anisotropy at the air-glass interface [24] and multipolar contributions from the bulk [25, 26] contribute to give a non-zero second order susceptibility $\chi^{(2)}$ which permits second harmonic generation. Microfibres are especially well suited for studying surface SHG owing to their large field strength at the surface. To date, there has been limited literature on SHG in microfibres [13, 14] and hence this work shall endeavour to model and experimentally characterise the second harmonic.

The third aim, to study the nonlinear behaviour in resonators, is comprised of two parts: (i) To use loop resonators for improving the efficiency of second and third harmonic generation, and (ii) to develop the nonlinear model of optical microcoil resonators (OMRs). Loop resonators can be formed by simply twisting and pushing a microfibre towards itself, to form a loop and coupling region. Though simple in concept and fabrication, the loop resonator can offer a Q factor of at least 10^4–10^5 in experiments even

when manufactured manually without any specialist equipment. As such, a pump wavelength residing near a resonance would be recirculated within the loop, which greatly increases the pump power inside the resonator. Assuming that the harmonic is phase matched along a section of microfibre within the loop, this would consequently enhance the conversion since the second and third harmonic power would respectively increase quadratically and cubically with increasing pump power.

Coiling a microfibre around a rod results in a unique resonator geometry known as the optical microcoil resonator, in which light can evanescently couple between adjacent turns to produce high Q resonances. OMR applications in a wide range of fields, such as sensing [27] and signal processing [28], have previously been studied at the Optoelectronics Research Centre (ORC), and a detailed understanding of OMR optical characteristics is crucial for further development. This work therefore aims to extend the theoretical models of OMRs published in literature [29, 30] by incorporating and assessing polarisation effects due to twist and birefringence, in both the linear and nonlinear domains.

1.2 Thesis structure

After this introduction, the thesis contains 6 chapters. We begin with an overview of the modal, nonlinear, and dispersive properties of microfibres in Chapter 2. In order to provide a technical reference for subsequent chapters, a detailed summary of the modes' electric fields and relevant formulae are also provided for convenience.

Next, Chapter 3 discusses both the theoretical and experimental results for third harmonic generation, including experiments towards increasing the bandwidth. For clarity, resonantly-enhanced THG, using loop resonators, is presented separately in Chapter 4, which theoretically studies the influence of the resonator geometry on the potential enhancement before discussing an experimental demonstration. Chapter 5 describes the theory and simulation work for second harmonic generation in both microfibres and loop resonators, as well as an experimental observation of the second harmonic in both cases.

In Chapter 6, the focus shifts to theoretically explore the polarisation dependent nonlinear properties of microcoil resonators. The behaviour is complex and so we first analyse the simpler linear regime in sec. 6.2.1, as well as Berry's phase effects in sec. 6.2.2, before proceeding to the nonlinear case in sec. 6.3.

Finally, Chapter 7 summarises the results achieved in this thesis and proposes several exciting areas in which the current work could be extended. In addition, three appendices are included for readers inclined or curious to read more about the high power pump source used in the experiments (Appendix A), derivation of the third harmonic generation differential equations (Appendix B) and numerical techniques used to solve the microcoil equations (Appendix C).

Chapter 2

Optical Properties of Microfibres

The attraction of microfibres for nonlinear experiments lies in the unusual combination of optical properties which include tight modal confinement, high effective nonlinearity, large evanescent field and a tailorable dispersion profile. In this chapter, these key linear and nonlinear optical characteristics will be explained, beginning with a discussion of the different modes supported by microfibres, followed by their nonlinear and dispersive properties. Since the experimental OMs described in this work are pulled from standard single mode fibre (SMF), emphasis will be given towards the differences between the properties of SMF and OMs. In addition, as a reference aid, the formulae describing the modal distributions (pertinent to Chapters 3, 4 and 5) are collectively presented here.

2.1 Optical guidance

Typically, a taper consists of a narrow microfibre waist region in between two transition regions connected to the original untapered fibre pigtails. As we are most interested in the propagation behaviour near the waist where the confinement is stronger, we model the OM as a homogenous uniform cylindrical waveguide, shown in Fig. 2.1, with a silica

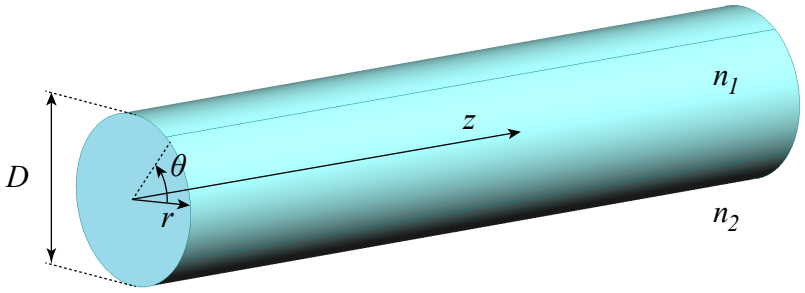

FIGURE 2.1: Schematic of the ideal silica microfibre in air, with a uniform diameter D and refractive index of $n_1 \approx 1.44$ surrounded by air ($n_2 = 1.0$).

core refractive index of $n_1 \approx 1.44$ at $\lambda = 1.55$ μm surrounded by the air cladding of $n_2 = 1.0$. The diameters D of interest, with regards to the work discussed in subsequent chapters, range from several microns down to a few hundred nm, and due to the structural symmetry it is convenient to describe the system using cylindrical coordinates (r, θ, z). Although the following discussions focus on silica OMs, the underlying theory remains nonetheless valid for other materials, such as chalcogenide and soft-glasses, as well as for OMs embedded low-index surroundings such as polymer for protective purposes.

The modes in a microfibre fall into 3 families, categorized according to the direction of their electric and magnetic field vector:

- Hybrid (HE, EH) modes, which possess non-zero electric and magnetic field vector components in all three r, θ and z directions.
- Transverse magnetic (TM) modes, for which the magnetic field vector lies only in the $r - \theta$ plane.
- Transverse electric (TE) modes, for which the electric field vector lies only in the $r - \theta$ plane.

In order to determine which modes are supported by the OM and their propagation constants β, for each mode family there exists an eigenvalue equation (EVE) expressable in the form $f(\beta) = 0$ whose real roots correspond to the β values of supported modes. For guided modes, these will always lie in the range $2\pi n_2/\lambda < \beta < 2\pi n_1/\lambda$.

The EVEs can be derived via an approach similar to that used for standard SMF since both the OM and SMF resemble step-index profile waveguides, and the standard textbook derivation beginning from Maxwell's equations can be found for example in [31] and [32]. However, whereas the weakly-guiding approximation $n_1 \approx n_2$ holds true for SMF (in which the core-cladding index difference $\Delta n = n_1 - n_2$ between a fused silica cladding and germanium-doped silica core is typically only $\Delta n \approx 10^{-3}$), the Δn of microfibres is over a hundred-fold greater, and consequently the EVEs must be derived and solved in their rigorous form.

Firstly, to clarify the notation, the propagating electric and magnetic fields are assumed to take the form:

$$\widetilde{\mathbf{E}}(r, \theta, z, t) = \frac{1}{2} A(z, t) \mathbf{E}(r, \theta) e^{i(\omega t - \beta z)} + c.c. \tag{2.1a}$$

$$\widetilde{\mathbf{H}}(r, \theta, z, t) = \frac{1}{2} A(z, t) \mathbf{H}(r, \theta) e^{i(\omega t - \beta z)} + c.c. \tag{2.1b}$$

where $A(z, t)$ denotes the slowly-varying 'pulse envelope' amplitude, $\exp(i(\omega t - \beta z))$ accounts for the rapid phase oscillation in time and space, and $\mathbf{E}(r, \theta)$ describes the modal distribution in the transverse plane, which is independent of z for a longitudinally

invariant waveguide cross-section and can be further decomposed into its constituent vector components:

$$\mathbf{E}(r,\theta) = \hat{\mathbf{r}}E_r(r,\theta) + \hat{\boldsymbol{\theta}}E_\theta(r,\theta) + \hat{\mathbf{z}}E_z(r,\theta) \tag{2.2}$$

(a similar formula expresses the modal magnetic field $\mathbf{H}(r,\theta)$). Substituting Eqns. 2.1 into Maxwell's equations yields the familiar wave equations:

$$\frac{\partial^2 E_z}{\partial r^2} + \frac{1}{r}\frac{\partial E_z}{\partial r} + \frac{1}{r^2}\frac{\partial^2 E_z}{\partial \theta^2} + [k^2 n(r,\theta)^2 - \beta^2]E_z = 0 \tag{2.3a}$$

$$\frac{\partial^2 H_z}{\partial r^2} + \frac{1}{r}\frac{\partial H_z}{\partial r} + \frac{1}{r^2}\frac{\partial^2 H_z}{\partial \theta^2} + [k^2 n(r,\theta)^2 - \beta^2]H_z = 0 \tag{2.3b}$$

The only physical solutions to Eqn. 2.3 satisfying $|\mathbf{E}| \to 0$ as r tends to ∞ are functions of Bessel functions of the first kind J (in the core) and modified Bessel functions of the second kind K (in the cladding). Combining this knowledge with the boundary conditions, which stipulate continuity of the tangential electric field, radial displacement field $D_r = \epsilon E_r$ and all magnetic field components at the glass-air interface, allows the full field expressions as well as the eigenvalue equations to be deduced. The resulting EVE for hybrid $\mathrm{HE}_{\nu m}$ and $\mathrm{EH}_{\nu m}$ modes, where ν and m denote the modes' azimuthal and radial order respectively, is expressed as [31]:

$$\left[\frac{J'_\nu(U)}{UJ_\nu(U)} + \frac{K'_\nu(W)}{WK_\nu(W)}\right]\left[\frac{J'_\nu(U)}{UJ_\nu(U)} + \left(\frac{n_2}{n_1}\right)^2\frac{K'_\nu(W)}{WK_\nu(W)}\right] = \left(\frac{\nu\beta}{kn_1}\right)^2\left(\frac{V}{UW}\right)^4 \tag{2.4}$$

where U, W and the normalised frequency V-parameter are related to β and the free space propagation constant $k = 2\pi/\lambda$ as follows:

$$U = a\sqrt{k^2 n_1^2 - \beta^2} \tag{2.5a}$$

$$W = a\sqrt{\beta^2 - k^2 n_2^2} \tag{2.5b}$$

$$V^2 = U^2 + W^2 \tag{2.5c}$$

with a denoting the microfibre radius. The EVE is transcendental in β and hence the supported propagation constants are solved for numerically. Similarly, for TE_{0m} modes the EVE is:

$$\frac{J_1(U)}{UJ_0(U)} + \frac{K_1(W)}{WK_0(W)} = 0 \tag{2.6}$$

and for TM_{0m} modes:

$$\frac{J_1(U)}{UJ_0(U)} + \left(\frac{n_2}{n_1}\right)^2\frac{K_1(W)}{WK_0(W)} = 0 \tag{2.7}$$

At the telecoms wavelength of $\lambda = 1.55$ μm, solving Eqns. 2.4, 2.6 and 2.7 for different OM diameters yields the modes shown in Fig. 2.2. When the diameter is below the threshold of 1.15 μm, the microfibre is single-moded as only the fundamental HE_{11} mode is supported. This critical diameter corresponds to the V-number of approximately

$V = 2.405$, which is the cut off of the lowest order TE/TM modes (given by first root of $J_0(U) = 0$ when $U = V$, as seen from Eqn. 2.6). The fundamental mode is strongly guided at a diameter of $D = 1.0$ μm and so the bend loss remains negligible even for curvature-radii down to ≈ 0.1 mm [33]; a feature which lends OMs to the fabrication of compact microresonators. However, for $D < 0.5$ μm the guidance is much weaker, with the effective index being only marginally above that of the surrounding air, and the light may radiate out from any sharp turns or structural perturbations.

At larger diameters of several μm, a variety of higher order modes are supported and due to the high numerical aperture of $NA = \sqrt{n_1^2 - n_2^2} = 1.04$, the number of modes grows rapidly with increasing diameter. For instance, increasing D from 2.5 to 3.0 μm introduces an additional 4 modes. It should be noted that all the modes are mutually non-degenerate. By comparison, the higher order modes in SMF may be degenerate and thus grouped under linear-polarisation (LP) mode designations – as an example, the LP_{11} multiplet in an SMF consists of the TE_{01}, TM_{01} and HE_{21} modes, whereas in an OM these modes would each follow entirely distinct dispersion curves. It is possible to limit the number of supported modes in the OM by controlling the diameter in order to filter out higher order modes, or to extend the single-mode operation bandwidth to shorter wavelengths [34, 35].

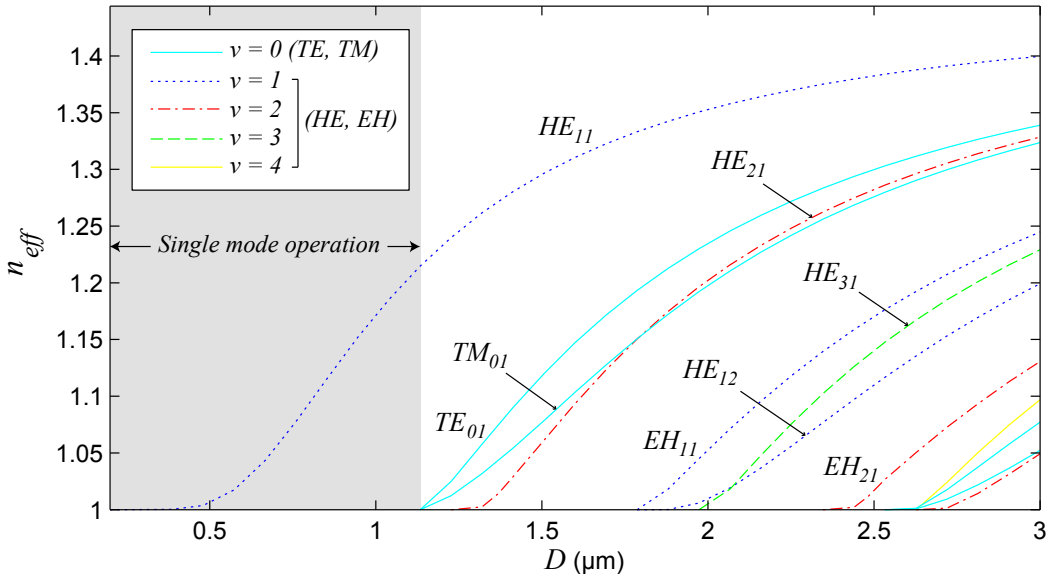

FIGURE 2.2: Mode dispersion n_{eff} curves showing effective index against microfibre diameter for the fundamental HE_{11} mode and various higher order modes. Azimuthal mode order number $\nu = 0$ corresponds to TE/TM transverse modes, whilst $\nu \geq 1$ corresponds to HE/EH hybrid modes. $\lambda = 1.55$ μm.

2.2 Mode properties

Having discussed how to determine which modes are supported by a microfibre in the previous section, to understand the properties of the modes further it is necessary to study their field distributions. For hybrid modes, the electric field has both transverse and longitudinal components; the latter being $+\pi/2$ out of phase [31]:

$$E_r = \begin{cases} -\frac{a_1 J_{\nu-1}(UR)+a_2 J_{\nu+1}(UR)}{J_\nu(U)} f_\nu(\theta) & r \le a \\ -\frac{U}{W}\frac{a_1 K_{\nu-1}(WR)-a_2 K_{\nu+1}(WR)}{K_\nu(W)} f_\nu(\theta) & r > a \end{cases} \tag{2.8a}$$

$$E_\theta = \begin{cases} -\frac{a_1 J_{\nu-1}(UR)-a_2 J_{\nu+1}(UR)}{J_\nu(U)} g_\nu(\theta) & r \le a \\ -\frac{U}{W}\frac{a_1 K_{\nu-1}(WR)+a_2 K_{\nu+1}(WR)}{K_\nu(W)} g_\nu(\theta) & r > a \end{cases} \tag{2.8b}$$

$$E_z = \begin{cases} -\frac{iU}{\rho\beta}\frac{J_\nu(UR)}{J_\nu(U)} f_\nu(\theta) & r \le a \\ -\frac{iU}{\rho\beta}\frac{K_\nu(WR)}{K_\nu(W)} f_\nu(\theta) & r > a \end{cases} \tag{2.8c}$$

where a is the core radius, $R = r/a$ is the normalised radial position, and the other parameters are listed below:

$$a_1 = \frac{F_2 - 1}{2} \quad , \quad a_2 = \frac{F_2 + 1}{2} \tag{2.9a}$$

$$F_1 = \left(\frac{UW}{V}\right)^2 \frac{b_1 + (1-2\Delta)b_2}{\nu} \quad , \quad F_2 = \left(\frac{V}{UW}\right)^2 \frac{\nu}{b_1 + b_2} \tag{2.9b}$$

$$b_1 = \frac{1}{2U}\left[\frac{J_{\nu-1}(U)}{J_\nu(U)} - \frac{J_{\nu+1}(U)}{J_\nu(U)}\right] \quad , \quad b_2 = -\frac{1}{2W}\left[\frac{K_{\nu-1}(W)}{K_\nu(W)} + \frac{K_{\nu+1}(W)}{K_\nu(W)}\right] \tag{2.9c}$$

$$\Delta = \frac{n_1^2 - n_2^2}{2n_1^2} \tag{2.9d}$$

and the fields vary sinuisoidally with azimuthal angle θ:

$$f_\nu(\theta) = \sin(\nu\theta + \Phi) \tag{2.10a}$$

$$g_\nu(\theta) = \cos(\nu\theta + \Phi) \tag{2.10b}$$

In the case of TE modes, the electric field only contains the E_θ component:

$$E_r, E_z = 0 \tag{2.11a}$$

$$E_\theta = \begin{cases} -\frac{J_1(UR)}{J_1(U)} & r \le a \\ -\frac{K_1(WR)}{K_1(W)} & r > a \end{cases} \tag{2.11b}$$

whereas for TM modes there exists a longitudinal E_z component in addition to a radial transverse field:

$$E_r = \begin{cases} \frac{J_1(UR)}{J_1(U)} & r \leq a \\ \left(\frac{n_1}{n_2}\right)^2 \frac{K_1(WR)}{K_1(W)} & r > a \end{cases} \tag{2.12a}$$

$$E_\theta = 0 \tag{2.12b}$$

$$E_z = \begin{cases} -\frac{iU}{\rho\beta} \frac{J_0(UR)}{J_1(U)} & r \leq a \\ -i\left(\frac{n_1}{n_2}\right)^2 \frac{W}{\rho\beta} \frac{K_0(WR)}{K_1(W)} & r > a \end{cases} \tag{2.12c}$$

Since the TE_{0m} and TM_{0m} field distributions are circularly symmetric, they are independent of θ and have $\nu = 0$ azimuthal order with reference to Eqns. 2.10. As we shall see in later chapters on harmonic generation, this symmetry of fields must be carefully considered in order to determine which higher order harmonic modes could potentially be generated, since only some will experience a non-zero overlap with the pump mode. Furthermore, the distribution and confinement of the pump mode itself is particularly important as it governs the effective nonlinearity γ. For the experiments in this work, the pump is always chosen as the fundamental HE_{11} mode and the typical $|\mathbf{E}|^2$ intensity

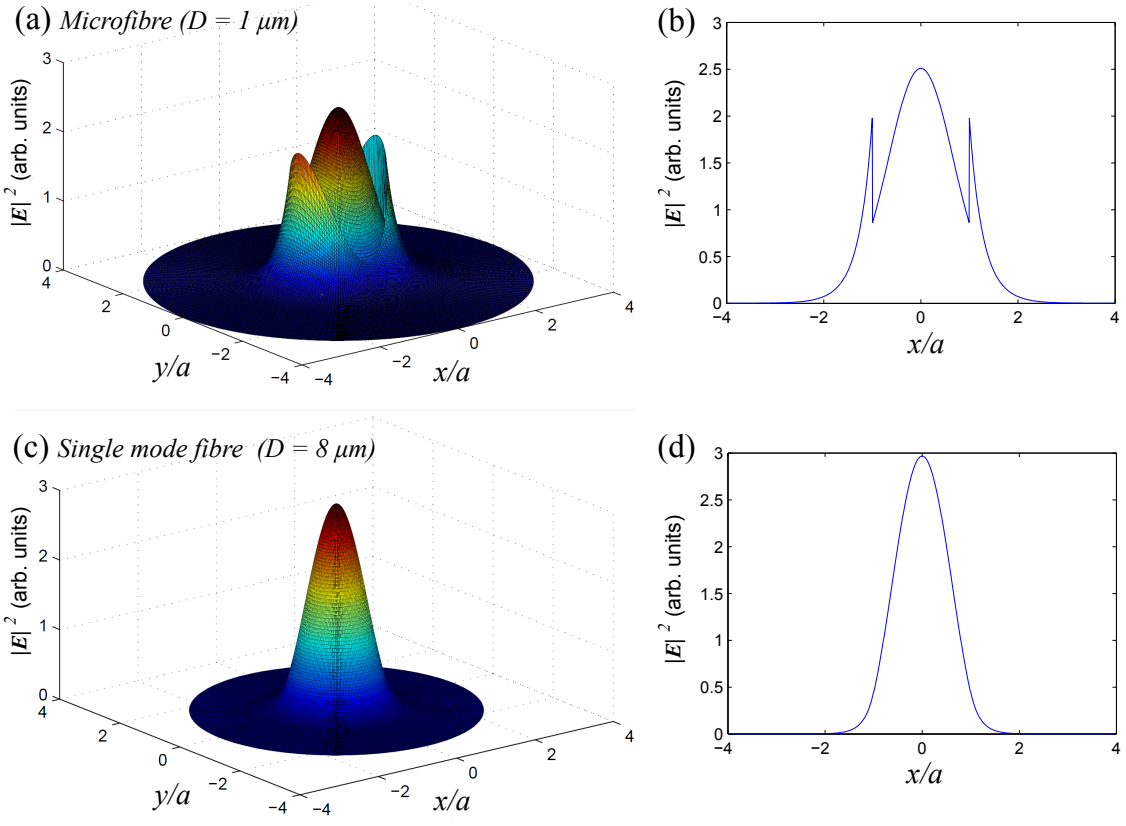

FIGURE 2.3: Mode field intensity $|\mathbf{E}|^2$ profiles for (a, b) a 1 μm diameter microfibre in air and (c, d) a typical telecoms single mode fibre with a $\Delta n = 0.01$ core-cladding index difference and 8 μm diameter core. Dimensions are normalised with respect to the core radius a. $\lambda = 1.55$ μm.

profile in a 1 μm diameter OM is shown in Fig. 2.3(a-b). Since the microfibres are fabricated from regular fibre, the fundamental mode in an 8 μm core diameter SMF is also shown in Fig 2.3(c-d) as a comparison.

Firstly, it can be seen that the mode in the OM is much more confined, spanning only over 2 μm or six times narrower at the full-width half-maximum (FWHM) than the SMF, due to the much higher index contrast. For the same reason, the field shows a large discontinuity at the microfibre surface and hence cannot be approximated to be a Gaussian function as is the case for optical fibre. The discontinuity arises from the boundary condition for the radial electric field, which states $E_r(r = a^+)/E_r(r = a^-) = (n_1/n_2)^2$ according to Gauss' Law in matter.

Secondly, the fraction of the mode in the evanescent field is much larger for the narrower microfibre than the SMF. Note that this does not contradict the aforementioned tight confinement – for an equivalent 8 micron diameter OM, the power would indeed remain tighter confined in the core than an 8 μm SMF. For a quantitative assessment, the ratio η of the power inside the OM over the total power P_0 can be defined as:

$$\eta = \frac{P_{\text{core}}}{P_0} = \frac{\iint_{\text{core}} S_z dA}{\iint_{-\infty}^{\infty} S_z dA} \tag{2.13}$$

where S_z denotes the time-averaged Poynting vector's longitudinal component which gives the propagating power per unit area:

$$S_z = \frac{1}{2}(\mathbf{E} \times \mathbf{H}^*) \cdot \hat{\mathbf{z}} = \frac{1}{2}(E_r H_\theta^* - E_\theta H_r^*) \tag{2.14}$$

As shown in Fig. 2.4, for diameters above 3 μm, close to $\eta = 100$ % of the power resides within the microfibre. When the diameter falls towards 1 μm however, η falls sharply with decreasing diameter and for a half micron diameter OM over 90 % of the light is in the evanescent field, as illustrated in Fig. 2.4(b). With such a large fraction of the power guided outside of the silica, it is perhaps more intuitive from a conceptual standpoint to conceive of the microfibre as a light rail, rather than a channel. It is also apparent from comparing Figs. 2.4(b-c) that narrower microfibres will experience a relatively higher field intensity at the glass surface, which for OMs with $D < 0.8$ μm will in fact exceed the intensity inside the core. Whilst this will enhance any interface effects, including surface-second harmonic generation, it also leaves the OM more susceptible to losses incurred by surface irregularities and contamination or bend loss. A narrower OM is also mechanically weaker, though this can be mitigated by embedding in a polymer if so required [36, 37, 38].

The large evanescent field itself is not amenable for nonlinear applications (unless the air is replaced by a nonlinear medium) but can be utilised for sensing or detection, since it is accessible to the environment. Examples of such devices include sensors based on

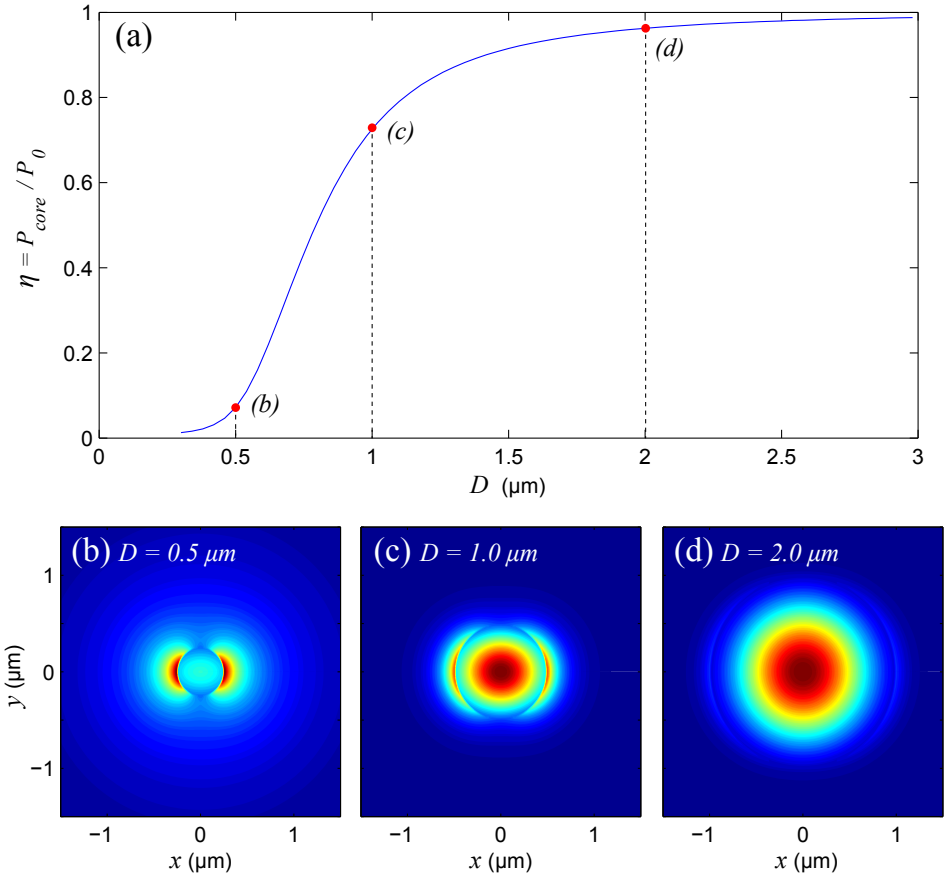

FIGURE 2.4: (a) Fraction of the power in the core, η, against diameter D for a silica microfibre in air, and the $|\mathbf{E}|^2$ field intensity distribution for microfibres with diameters of (b) $D = 0.5$ μm, (c) 1.0 μm and (d) 2.0 μm. $\lambda = 1.55$ μm.

absorption loss/spectroscopy [39, 40, 41] and refractometric sensors [27, 38, 42, 43]. The evanescent field does however allow resonators useful for nonlinear experiments to be realised, via evanescent coupling between different sections of the same microfibre, such as the microcoil [23] and loop resonators [21] as explained in Chapters 4, 5 and 6.

Modal confinement is also a strong function of diameter for wavelengths comparable to D/n_1, and is commonly measured by the effective area A_{eff} which essentially gives the power-weighted average area of the mode:

$$A_{\text{eff}} = \frac{|\iint_{-\infty}^{\infty}(\mathbf{E}\times\mathbf{H}^*)\cdot\hat{\mathbf{z}}dA|^2}{\iint_{-\infty}^{\infty}|(\mathbf{E}\times\mathbf{H}^*)\cdot\hat{\mathbf{z}}|^2dA} = \frac{|\iint_{-\infty}^{\infty}S_z dA|^2}{\iint_{-\infty}^{\infty}|S_z|^2dA} \tag{2.15}$$

For diameters of several microns, the effective area decreases with decreasing D as shown in Fig. 2.5, with the modal area limited by the waveguide cross section area. Near to $D = 1.0$ μm, A_{eff} reaches a minimum of approximately 1.1 μm^2 which corresponds to a $1/e^2$ intensity spot-size of approximately $\omega = 0.8$ μm. This point of maximum confinement is close to the diffraction limited value of $\omega_0 = \lambda/(2n_1)$, and the ability of microfibres to maintain such a tight modal confinement over potentially indefinite distances (limited only by the tapering rig equipment and loss) allows for long nonlinear

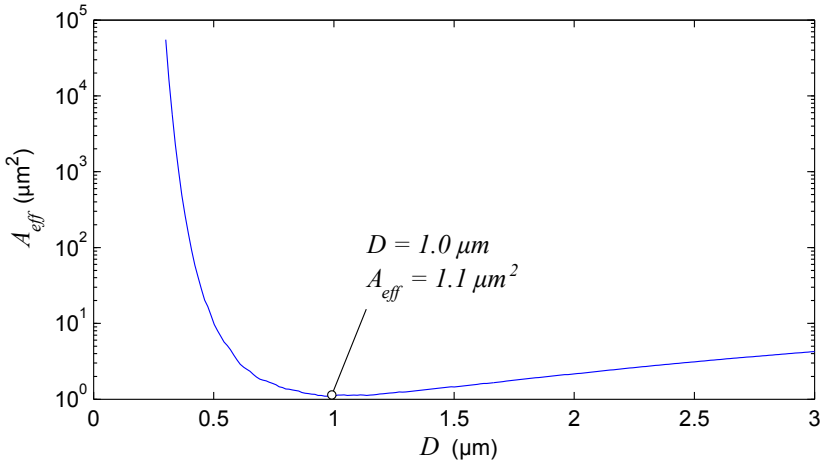

FIGURE 2.5: The effective area A_{eff} of the fundamental mode against diameter D for a silica microfibre. $\lambda = 1.55$ μm.

interaction lengths. Using higher index glasses would improve the confinement further, with the minimum A_{eff} occurring at a narrower diameter. The strong confinement permits tight turns, and indeed bend-radii down to $\rho = 100$ μm in coiled microfibres have been fabricated with negligible bend loss [33, 44]. For diameters narrower than 0.5 μm ($V < 1$) however, the evanescent field can extend far from the microfibre and grow unbound which causes A_{eff} to expand rapidly with decreasing diameter, increasing by over 3 orders of magnitude from $D = 0.5$ μm to 0.3 μm (in theory, $A_{\text{eff}} \to \infty$ in the limit $D \to 0$, although at a diameter of 100 nm the guidance will already be too weak for most practical purposes).

Reducing the diameter will not only increase the evanescent field fraction and alter the confinement by changing the power distribution of the mode, but will also affect the direction of the electric field vectors. For a large OM with $D \approx 10$ μm, the x-polarised fundamental mode vectors would be almost entirely unidirectional, much like a linearly polarised LP_{01} mode in SMF. However, when the OM diameter is comparable to λ/n_1 there is also a significant component of the transverse field vector which points orthogonally to the dominant polarisation as shown in 2.6(a). For this reason, the microfibre HE_{11} mode is sometimes termed 'quasi-x or y- polarised' [45]. Furthermore, the longitudinal component E_z cannot be neglected, since it can account for almost a third of the mode's power. The fraction of light in the transverse components can be evaluated by the transversality parameter [19], defined below and plotted against diameter in Fig. 2.6(b):

$$T = 1 - \frac{\int\int_{-\infty}^{\infty} |E_z^2| dA}{\int\int_{-\infty}^{\infty} |\mathbf{E}|^2 dA} \tag{2.16}$$

Whereas the transversality for large diameters is almost 100 %, since the power is largely contained in the transverse field components, for narrower diameters the longitudinal field becomes greater and near $D = 1$ μm the transversality reaches a minimum of

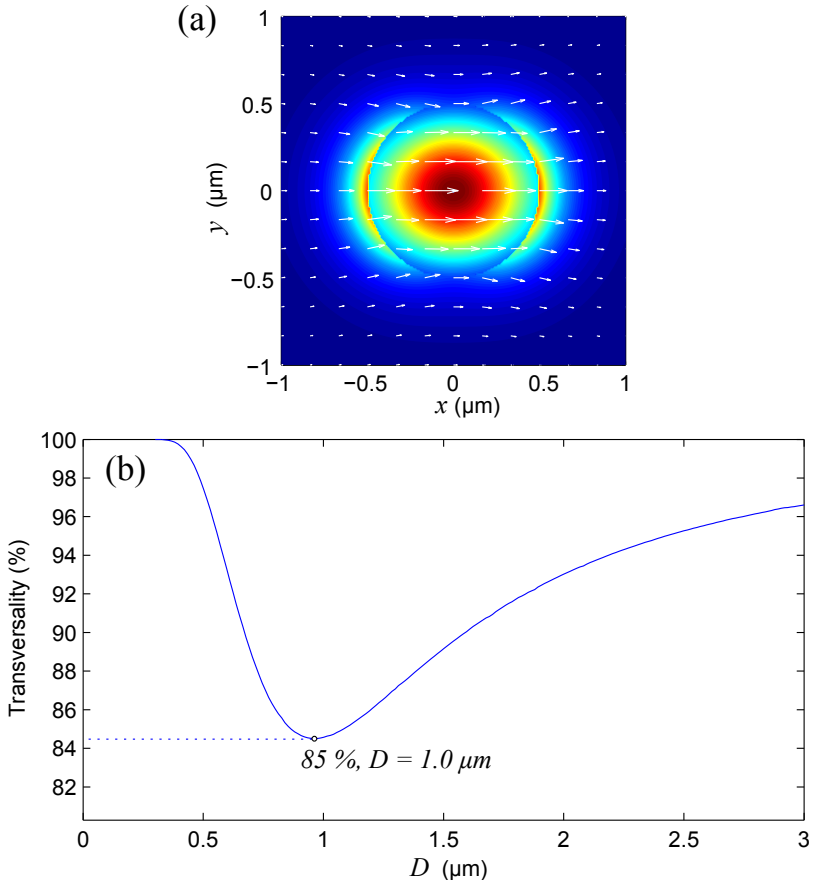

FIGURE 2.6: (a) Transverse electric field $[E_x, E_y]$ vector plot of the fundamental mode in a 1 μm diameter microfibre, showing quasi x polarisation. Background represents $|\mathbf{E}|^2$ total intensity. (b) The transversality (a measure of the fraction of power residing in the transverse, as opposed to longitudinal, field components defined in Eqn. 2.16) against diameter. $\lambda = 1.55$ μm.

85 % at the point coinciding with the tightest confinement. In higher index OMs this effect would be more pronounced; for example, the minimum transversality in a silicon microfibre would be only 64 % [19]. The multidimensional nature of the vector field must be considered for an accurate assessment of the OM's nonlinearity [19, 46, 47, 48] as discussed in the next section.

2.3 Nonlinearity

The high effective nonlinearity γ of the microfibre, being inversely proportional to the effective modal area, arises from the tight confinement offered by the large index contrast:

$$\gamma = \frac{2\pi}{\lambda} \frac{\overline{n^{(2)}}}{A_{\text{eff}}} \tag{2.17}$$

Eqn. 2.17 does not directly include the nonlinear refractive index coefficient of silica, $n^{(2)} = 2.7 \times 10^{16}$ cm^2 W^{-1} at $\lambda = 1.55$ μm, but instead uses its averaged counterpart

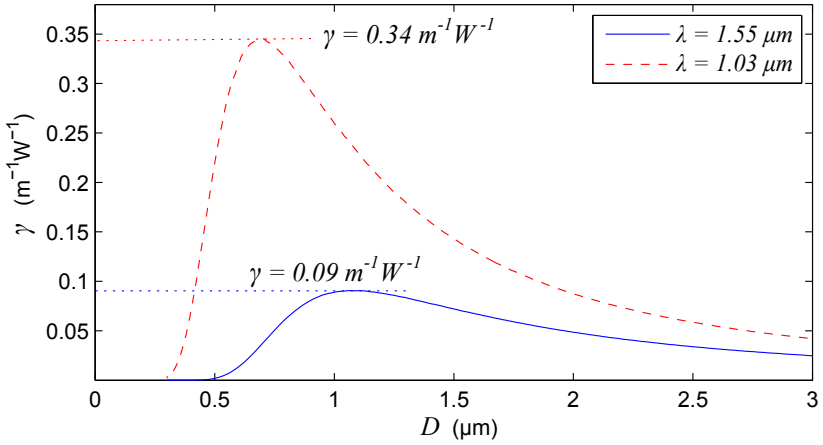

FIGURE 2.7: The effective nonlinearity γ against diameter D for a silica microfibre in air.

$\overline{n^{(2)}}$ which is weighted according to the fraction of power distributed within the core:

$$\overline{n^{(2)}} = k\left(\frac{\epsilon_0}{\mu_0}\right)\frac{\iint_{A_{\text{core}}} n_1^2(x,y)n^{(2)}(x,y)[2|\mathbf{E}|^4 + |\mathbf{E}\cdot\mathbf{E}|^2]dA}{3\iint_{-\infty}^{\infty}|(\mathbf{E}\times\mathbf{H}^*)\cdot\hat{\mathbf{z}}|^2 dA} \tag{2.18}$$

In contrast to the nonlinear model for SMF, this distinction is required for OMs to take into account the lack of nonlinearity for the evanescent field in air. Furthermore, both $\overline{n^{(2)}}$ and A_{eff} must be evaluated vectorially since the equivalent scalar calculations traditionally used for bulk/SMF, in which the fields are assumed entirely transverse, underestimate the nonlinearity by ignoring the sizable longitudinal field contribution [46, 48].

Figure 2.7 shows that the effective nonlinearity peaks as expected near the region of greatest confinement around $D = 1.1$ μm with $\gamma = 0.09$ m^{-1}W^{-1} for a 1.55 μm wavelength, which is 2 orders of magnitude greater than that of telecoms SMF [24]. Note that this diameter is in fact marginally wider than the point at which A_{eff} is minimal, since in the narrow core regime η and hence $\overline{n^{(2)}}$ both fall rapidly with narrowing diameter.

As explained Chapters 3 and 5, the high nonlinearity allows appreciable third and second harmonic to be generated in sub-micron diameter OMs over distances of several millimeters and relatively low peak pump powers down to 1 kW. For the shorter wavelength of 1.03 μm, the maximum possible modal confinement is tighter and so the nonlinearity peaks with a higher value of $\gamma = 0.34$ m^{-1}W^{-1} at a correspondingly narrower diameter of 0.7 μm. Yet higher nonlinearities are possible for highly nonlinear glasses, e. g. up to $\gamma = 93$ m^{-1}W^{-1} with chalcogenide microfibres [49].

Lastly, it is worth noting that the vectorial nonlinear model also implies an interesting anisotropy in the interaction of different polarisations for elliptical OMs: aside from each polarisation having different nonlinear coefficients $\gamma_x \neq \gamma_y$, the non-transversality breaks the usual orthogonality relationship, giving a non-zero $\iint_{\text{core}}|\mathbf{E}_x\cdot\mathbf{E}_y|dA$ overlap

which not only increases the cross phase modulation coefficients between orthogonally polarised waves but introduces a route for cross-polarisation power exchange mediated by their longitudinal field components [19, 50].

2.4 Dispersion

The chromatic dispersion of a microfibre, which causes different frequencies to propagate with different phase velocities and delays, comprises of two distinct contributions summed together:

1. *Material dispersion*, which arises from the variation of the glass' refractive index with wavelength ($n(\lambda)$ is often modelled empirically using a Sellmeier equation [51]). Since this is an intrinsic property of the glass, material dispersion would be present even for propagation in bulk media.

2. *Waveguide dispersion*. The modal distributions and hence the n_{eff} and propagation constant vary according to the size of the diameter relative to the wavelength, even if a constant material index were assumed. This dispersion is therefore governed by geometry, rather than the material properties.

Dispersive effects are especially important for short pulse nonlinear interactions (usually ps or shorter) involving spectrally-broad signals or multiple wavelengths such as supercontinuum generation [9, 10, 52], and even in many linear systems including communication networks where the pulse broadening from dispersion warrants consideration. In any case, a pulse in time cannot be perfectly monochromatic but will contain a finite bandwidth centred on a central frequency ω_0, with each frequency component experiencing a slightly different propagation constant $\beta(\omega)$. The model of chromatic dispersion is therefore based on expanding $\beta(\omega)$ as a Taylor series about ω_0:

$$\begin{aligned}\beta(\omega) &= \beta_0 + \beta_1(\omega-\omega_0) + \frac{1}{2}\beta_2(\omega-\omega_0)^2 + \frac{1}{6}\beta_3(\omega-\omega_0)^3\cdots \\ &= \beta_0 + \sum_{j=1}^{\infty}\frac{1}{j!}\beta_j(\omega-\omega_0)^j\end{aligned} \tag{2.19}$$

where the derivatives β_j define the j^{th} order dispersion coefficients:

$$\beta_j = \frac{\partial^j \beta(\omega)}{\partial \omega^j}\Big|_{\omega=\omega_0} \tag{2.20}$$

The first order dispersion gives the inverse of the group velocity v_g [24]:

$$\beta_1 = \frac{1}{v_g} = \frac{1}{c}\left(n + \omega\frac{dn}{d\omega}\right) \tag{2.21}$$

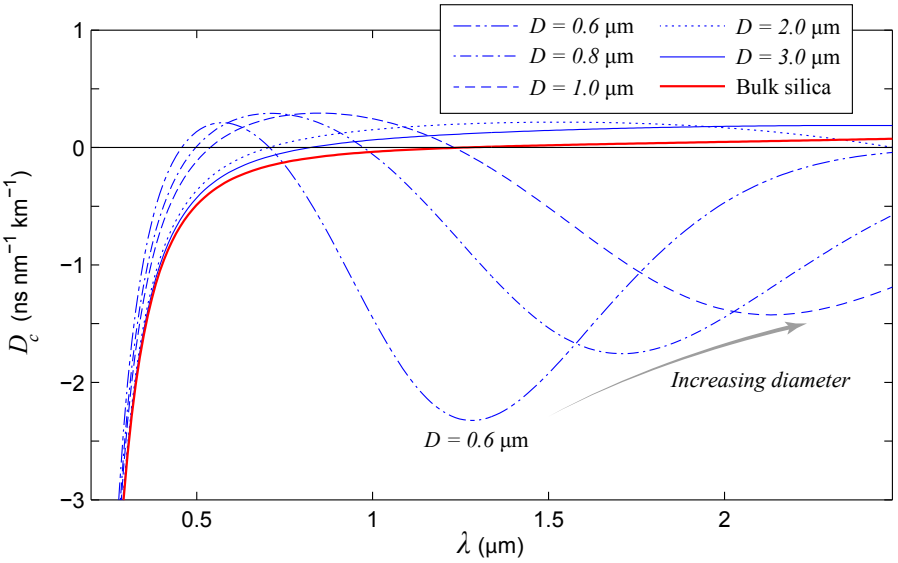

FIGURE 2.8: Second order chromatic dispersion D_c profiles for microfibre diameters between 0.6–3 μm. For comparison, the bulk silica material dispersion is given by the thick red line.

Physically, v_g represents the speed at which the pulse envelope travels along the OM. For very wide diameters the mode is largely contained within the OM and so v_g is close to c/n_1, whereas for narrow OMs ($D \ll \lambda/n_1$) v_g will approach c since the power propagates mostly in air. In between these extremes, v_g does not simply vary monotonically with diameter but instead reaches a minimum value slightly under c/n_1, at the diameter coinciding with greatest confinement [53].

The second order dispersion β_2 denotes the group velocity dispersion, which causes pulse broadening and is often expressed in the alternative form by the dispersion parameter D_c:

$$D_c = -\frac{2\pi c}{\lambda^2}\beta_2 \tag{2.22}$$

Figure 2.8 compares the dispersion profiles D_c of OMs with various diameters. For a large 3 μm diameter OM, D_c is close to the bulk material dispersion of silica since the mode resides mostly within the silica OM, and only one zero dispersion wavelength (ZDW) is present in the plotted wavelength range up to $\lambda = 2.5$ μm. For narrower diameters around 1 μm however, the waveguide dispersion component becomes dominant which drastically alters the profile by introducing a second ZDW at a longer wavelength as well as wide spectral regions of negative (i. e. 'normal') dispersion. As an example, the dispersion in a 600 nm diameter OM at $\lambda = 1.55$ μm is over 77 times greater in magnitude than that of bulk silica.

The first and second ZDWs divide the dispersion profile into a region of anomalous dispersion sandwiched between two normal dispersion regions as shown in Fig. 2.9. The spectral range of the anomalous region decreases for narrower OMs, until it disappears altogether for $D < 0.43$ μm which results in an wholly normal dispersion profile.

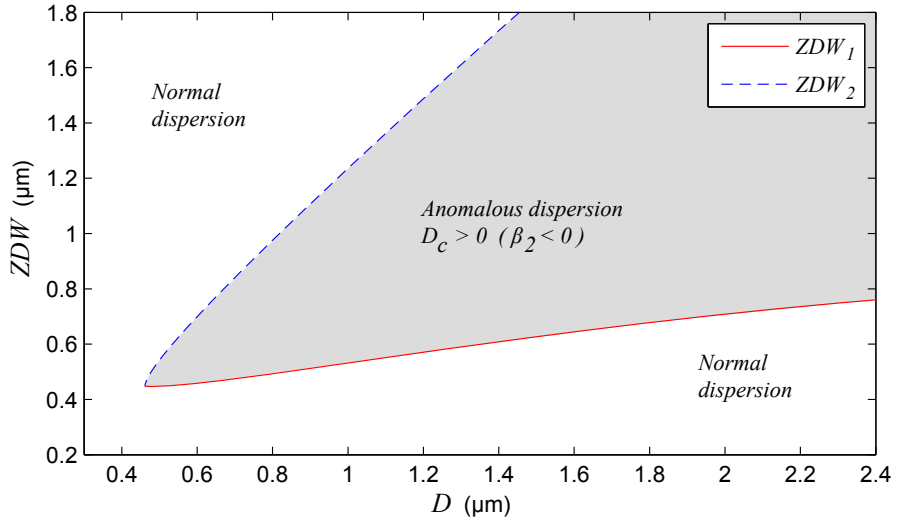

FIGURE 2.9: The dependency of the two zero dispersion wavelengths (ZDWs) on microfibre diameter. Shaded area indicates the anomalous dispersion region.

The higher order terms (β_j, $j \geq 4$) are less significant and generally neglected unless operating a few nanometers from a ZDW where $\beta_2 \approx 0$, or working in the ultrafast regime, where they can influence the pulse shape.

2.5 Summary

The modal properties of a microfibre differ significantly from standard single mode fibre due largely to the high index-contrast between the glass OM and surrounding air, which permits guidance even with sub-micron waveguide dimensions. It is consequently possible to achieve tight modal confinement down to $A_{\text{eff}} \approx (\lambda/n_1)^2$ μm^2 and a large effective nonlinearity close to $\gamma = 0.1$ W^{-1} m^{-1}, for a telecom wavelength of 1.55 μm. Furthermore, the strongly geometry-dependent dispersion profile can be engineered by simply adjusting the diameter, for example to shift the zero dispersion wavelength. For narrow microfibres $D \approx \lambda/n_1$, the external evanescent field is large and can be utilised for sensing.

Having established a theoretical background for the microfibre's optical characteristics in this chapter, the next section shall proceed to discuss, in detail, how the high nonlinearity can be applied for efficient third harmonic generation.

Chapter 3

Third Harmonic Generation in Microfibres

Efficient frequency tripling in microfibres is possible by utilising the inherent $\chi^{(3)}$ of silica for third harmonic generation. This chapter begins by providing an overview of the key concepts behind third harmonic generation (THG) in microfibres and a brief review of background literature. Next, the theoretical phase matching conditions are calculated, followed by an analysis of the conversion efficiency for different third harmonic modes. A selection of experimental THG results obtained using short and long microfibres are then discussed.

3.1 Overview

At the microscopic level, an electromagnetic field in a dielectric medium will induce a polarisation $\widetilde{\mathbf{P}}(\mathbf{r},t)$ by distorting the electron cloud distribution to give a dipole moment. Assuming a quasi-instantaneous response, the dependency on the electric field $\widetilde{\mathbf{E}}(\mathbf{r},t)$ can be expressed as a power series [54]:

$$\widetilde{\mathbf{P}}(\mathbf{r},t) = \chi^{(1)} \cdot \widetilde{\mathbf{E}}(\mathbf{r},t) + \chi^{(2)} : \widetilde{\mathbf{E}}(\mathbf{r},t)\widetilde{\mathbf{E}}(\mathbf{r},t) + \chi^{(3)} \vdots \widetilde{\mathbf{E}}(\mathbf{r},t)\widetilde{\mathbf{E}}(\mathbf{r},t)\widetilde{\mathbf{E}}(\mathbf{r},t) \cdots \tag{3.1}$$

where $\chi^{(1)}$ denotes the linear susceptibility, and the first term gives the linear polarisation $\widetilde{\mathbf{P}}_L$. The subsequent terms comprise the nonlinear polarisation $\widetilde{\mathbf{P}}_{\mathrm{NL}}$, and the notation ‘ : ’ and ‘ $\vdots$ ’ indicate they should be evaluated through the susceptibility $\chi^{(i)}$ tensor product with the electric fields. The second order susceptibility $\chi^{(2)}$ governs SHG and three wave interactions, and $\chi^{(3)}$ is responsible for THG and four wave mixing (FWM) processes. In general, $\chi^{(i)}$ represents a rank $(i+1)$ tensor with $3^{(i+1)}$ components, but for many materials the structural symmetry can be exploited to simplify analysis. In particular, the centrosymmetry of fused silica implies that $\widetilde{\mathbf{P}}(\widetilde{\mathbf{E}}) \equiv -\widetilde{\mathbf{P}}(-\widetilde{\mathbf{E}})$, which is only possible

if $\chi^{(2)}$ is identically zero[1], and also the $\chi^{(3)}$ tensor simplifies considerably. If the smaller contributions from higher order nonlinear processes are neglected, $\widetilde{\mathbf{P}}_{\mathrm{NL}}$ reduces to [19]:

$$\widetilde{\mathbf{P}}_{\mathrm{NL}} = \frac{1}{2}\epsilon_0 \chi^{(3)}_{xxxx}\left[(\widetilde{\mathbf{E}}\cdot\widetilde{\mathbf{E}}^*)\widetilde{\mathbf{E}} + \frac{1}{2}(\widetilde{\mathbf{E}}\cdot\widetilde{\mathbf{E}})\widetilde{\mathbf{E}}^*\right] \tag{3.2}$$

It is clear from Eqn. 3.2 that the nonlinear polarisation can mix an input pump beam $E \sim \exp(i\omega_1 t) + c.c.$ to generate new frequencies including a term at $\exp(i3\omega_1 t)$, which provides a route for coupling power into the third harmonic. However, since the pump and harmonic waves travel in the waveguide with different propagation constants β_1 and β_3 respectively, the harmonic can only grow if the waves are phase matched with each other, i.e. $\delta\beta = \beta_3 - 3\beta_1 \approx 0$, which is equivalent to ensuring their modes share the roughly the same effective index (a slight difference may be needed to offset nonlinear phase modulations, but for ∼kW power levels the correction is small).

Ideally, it would be preferable to phase match the fundamental pump mode with the fundamental harmonic mode, since their mode profile similarity guarantees a large overlap, but such a scheme is unfortunately unfeasible - even in the absence of material dispersion, a fundamental mode at a shorter wavelength would always be confined tighter within the core, and hence the n_{eff} of the fundamental harmonic mode would always exceed that of the fundamental pump regardless of the microfibre size or material.

On the other hand, it is possible to phase match the pump to a higher order harmonic mode with the same n_{eff} by carefully choosing the diameter of the microfibre and indeed this is the scheme which is employed in this work. The idea of intermodal phase matching has in the past been considered for various parametric processes such as four wave mixing in optical fibres, but the low modal confinement results in a poor overlap between the interacting waves, which severely limits the efficiency [55]. In microfibres however, the stronger confinement allows for much larger overlaps between the pump and harmonic modes as will be shown section 3.3.2.

3.2 Background

The earliest reported observation of THG in tapered fibres by Akimov et al. [15] used 1.25 μm Cr:forsterite laser pulses to produce a third harmonic signal. After deriving the conditions for phase matching, a 9 cm taper was fabricated with the critical phase matching diameter of 2.6 μm. When pumped using 30 fs pulses with a peak power of 10 kW, the conversion efficiency was estimated to be $\eta = 0.05$ %. Meanwhile, Koletova et al. theoretically studied THG in microfibres by accounting for group-delay effects and nonlinear phase shifts, as well as calculating the required phase matching diameters [56].

[1]Strictly, a small non-zero second order susceptibility exists in silica due to magnetic dipole and higher order electric quadrupole effects, as well as surface structural anisotropy near an interface. These are discussed further in Chapter 5.

Later, Grubsky and Savchenko refined the theory by deriving the differential equations and evaluating the overlap integrals between the pump and various TH modes, using a more accurate vectorised field model rather than scalar fields [17]. Experimental work by Grubsky et al. also confirmed the sudden onset of THG when the taper is pulled to the critical diameter [16]. However, the conversion efficiency of 10^{-6} was low due to the short 100 μm taper length. In the same series of experiments, the second harmonic was also observed for a taper diameter which corresponded to its phase matching, although this was not studied any further.

During the course of this work, other teams have also investigated harmonic generation in microfibres. THG using a 1.55 μm source was observed by Coillet et al. [11], who also highlighted the potential and practicalities of using microfibres based on highly nonlinear glasses such as tellurite and chalcogenide [18]. Karapetyan et al. reported on a possible application for characterising microfibre diameters by tuning a Ti:Sapphire source across the 850-1000 nm range and recording the wavelengths at which the third and second harmonic peaks appear [14]. At these wavelengths, the diameter must correspond to a phase match point and can therefore be deduced. Whilst the work did not attempt to maximise the strength of the harmonic signals, it nonetheless confirmed that the SH/TH at multiple predicted phase match points are observable.

Furthermore, Delgado-Pinar et al. observed THG in 500 nm diameter silica microfibres produced using the flame brushing technique [57]. The waist length of 3 cm in this case was significantly longer than those previously reported so as to increase the conversion, and the fibres were found to be capable of sustaining high peak powers up to 3 kW with ps pulses at MHz repetition rates. When pumped with a pulsed 1064 nm source, the $HE_{12}(3\omega)$ TH mode was indeed excited as confirmed by modal imaging at the output but the efficiency was only 4×10^{-6}. This may have been limited by a combination of UV absorption, low fabrication tolerance and walkoff associated with short pulses.

3.3 Theory and simulations

3.3.1 Phase match points

To find the phase match points, we first calculate the mode dispersion curves of n_{eff} against diameter. The rigourous form of the modal eigenvalue equations (EVE) in Eqn. 2.4 must be used [31], since the large index contrast between the silica core and air cladding invalidates the weakly-guiding approximation normally used for standard fibre analysis.

The motivation for simulating a step-index profile, rather than a three layer system based on the SMF-core/cladding/air, lies in that fact that the high processing temperatures of $1300°C$ needed to pull the microfibres will facilitate dopant diffusion between the core

and cladding of the original parent fibre, so the final taper is likely to have uniform material properties. Note that a three-layer model [58, 59] might however be applicable were one to solve for modes in the mid-transition region where the larger diameter might retain a distinct core.

Since the harmonic and pump signals experience different material dispersion, a wavelength-dependant Sellmeier formula [60] was used to calculate the silica's refractive index n_1:

$$n_1^2 = 1 + \frac{0.6961663\lambda^2}{\lambda^2 - (0.0684043)^2} + \frac{0.4079426\lambda^2}{\lambda^2 - (0.1162414)^2} + \frac{0.8974794\lambda^2}{\lambda^2 - (9.896161)^2} \tag{3.3}$$

This formula has been verified to be accurate to within 10^{-5} between $0.3\ \mu\text{m} < \lambda < 2\ \mu\text{m}$, which covers both the pump λ_1 and harmonic λ_3 wavelengths for λ_1 down to 1 μm. To solve the eigenvalue equation, it is convenient to reformulate it as a function of the normalised propagation parameter $b = (n_{\text{eff}}^2 - n_2^2)/(n_1^2 - n_2^2)$ as any guided mode solution

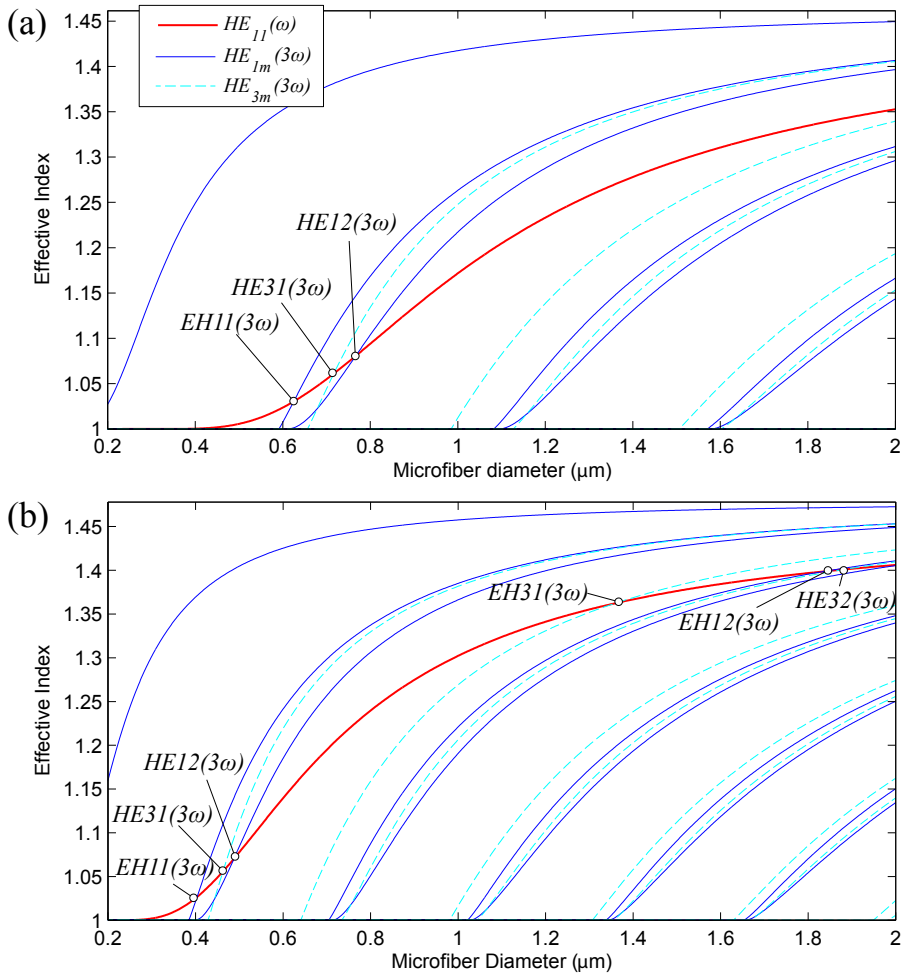

FIGURE 3.1: Effective index curves for the fundamental $\text{HE}_{11}(\omega)$ pump mode (red) and third harmonic hybrid modes with azimuthal order $\nu = 1$ (solid blue) and $\nu = 3$ (dashed cyan) in a silica microfibre for (a) $\lambda_1 = 1.550\ \mu$m and (b) $\lambda_1 = 1.03\ \mu$m. Phase match points are highlighted.

Harmonic Mode	Diameter (nm)	n_{eff}	Overlaps (μm^{-2})				L_{NL} (mm)	L_{THG} (m)
			J_1	J_2	J_3	J_5		
EH11	625	1.03	0.33	0.76	4.60E-03	4.27	28	2.14
HE12	766	1.08	0.97	1.46	0.34	3.97	9	0.027
EH12	3475	1.41	0.35	0.20	2.73E-04	0.37	26	33
HE13	3811	1.42	0.29	0.26	7.80E-04	0.47	31	11
HE31	717	1.06	0.74	0.99	0.061	4.03	12	0.15
EH31	2510	1.38	0.61	0.19	2.75E-04	0.58	15	33
HE32	3538	1.41	0.34	0.18	7.80E-04	0.32	27	12

TABLE 3.1: A summary of the possible phase match points for a 1.55 μm wavelength pump and corresponding overlap integrals J_i for the pump and harmonic modes, which are defined in Eqn. 3.8. The nonlinear length L_{NL} and third harmonic length L_{THG} are also provided for each diameter, and represent the distances over which the nonlinearity and third harmonic signal become significant for 1 kW pump power, respectively.

is guaranteed to reside in the range $0 < b < 1$. The EVE is transcendental in b and so a numerical approach (the Newton method) was adopted to be find the roots. When multiple solutions exist, the search range was divided into segments between values of b which correspond to the cut off for different modes to ensure all solutions can be found.

Mode index curves for the fundamental pump and hybrid $\mathrm{HE}_{\nu m}(3\omega)/\mathrm{EH}_{\nu m}(3\omega)$ third harmonic modes are shown in Fig. 3.1 for a $\lambda_1 = 1.55$ and $\lambda_1 = 1.03$ μm pump. These two pump wavelengths are of particular interest since high power sources for both wavelengths are readily available, namely through Erbium and Ytterbium doped laser systems.

For microfibre diameters up to 2 microns, both pump sources can phase match with the $\mathrm{EH}_{11}(3\omega)$ and $\mathrm{HE}_{12}(3\omega)$ modes, but the 1.03 μm pump can also match with additional modes including the $\mathrm{EH}_{12}(3\omega)$ and $\mathrm{HE}_{13}(3\omega)$ (in general, a fibre of a given diameter will support more modes if a shorter wavelength is used, as this corresponds to a larger V number). The phase matching points for both graphs are summarised in Table 3.1, and show that the critical diameters are roughly half a micron or larger - dimensions which are realisable using existing tapering rigs at the ORC with a microheater element.

Higher azimuthal order harmonic modes with $\nu = 3$ also can be phase matched, such as the $\mathrm{HE}_{31}(3\omega)$ mode. However, certain modes such as those with an even ν or $\nu > 3$ do not have any overlap with the pump due to their field symmetry, so these cannot be observed and hence are not considered (see Appendix B for a detailed explanation).

To summarise, the critical THG diameters were calculated for a range of different pump wavelengths and are plotted in Fig. 3.2, which includes all matching hybrid TH modes for $\nu = 1, 3$. Compared to shorter pump wavelengths, the 1.55 μm pump's phase matching diameters are further apart - experimentally, this has the advantage of being able to resolve the modes easier if the TH is being measured in-situ whilst tapering the fibre, or preferentially couple to only one particular harmonic mode.

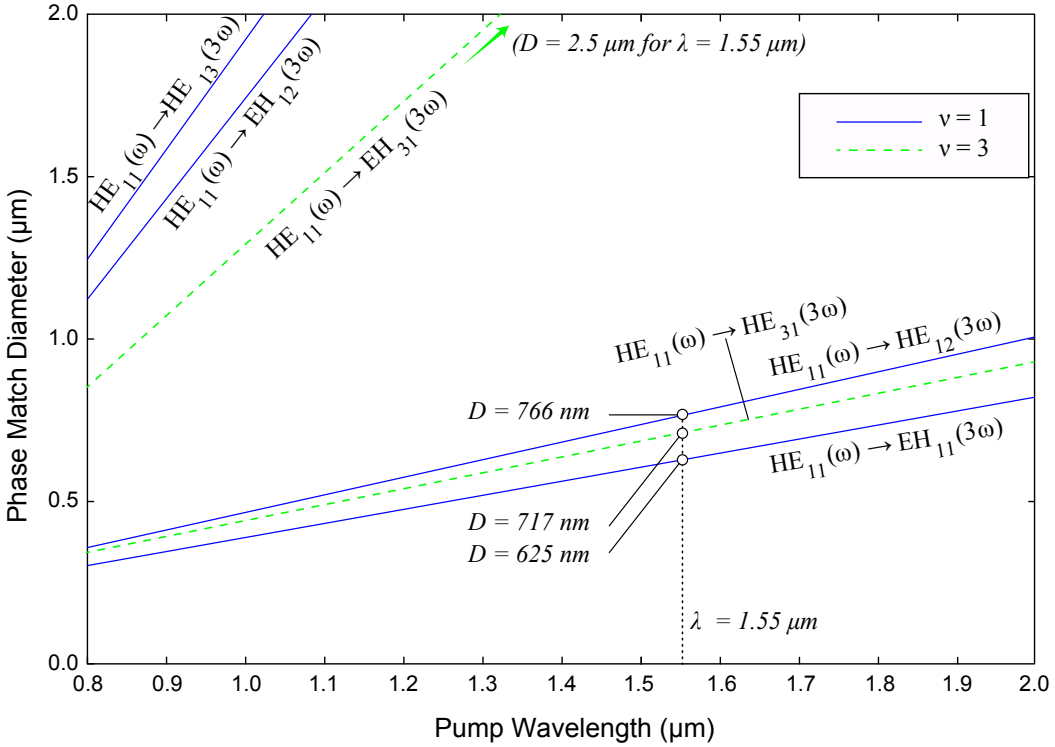

FIGURE 3.2: Third harmonic phase match diameters at different pump wavelengths, when matched to $\mathrm{HE}_{\nu m}(3\omega)$ and $\mathrm{EH}_{\nu m}(3\omega)$ modes for ν=1 (blue) and ν=3 (green).

Finally, it is worth mentioning that each and every harmonic mode (except the fundamental) can in fact be phase matched with the pump. At its cut-off diameter, a higher order harmonic mode's index will always be near 1, so $n_{\text{eff}}\ (\omega) > n_{\text{eff}}\ (3\omega)$. However, as the diameter tends to infinity, $n_{\text{eff}}\ (\omega)$ approaches $n_1(\omega)$ whereas $n_{\text{eff}}\ (3\omega)$ approaches $n_1(3\omega)$, which is higher owing to material dispersion. Therefore, at a certain point between the cut-off diameter and $D = \infty$, the two modes' n_{eff} must be equal to each other. To determine which harmonic mode offers the greatest conversion efficiency, the next section will consider their overlap with the pump.

3.3.2 Efficiency calculation

To simulate the THG conversion, the overlap between the interacting pump and harmonic modes must be evaluated. The electric and magnetic fields in the fibre are defined as:

$$\widetilde{\mathbf{E}}(\mathbf{r},t) = \sum_{i=1,3} A_i(z)\sqrt{Z_0}\mathbf{E}_i(\mathbf{r}_\perp)\exp i(\beta_i z - \omega_i t) + \text{c.c.} \tag{3.4a}$$

$$\widetilde{\mathbf{H}}(\mathbf{r},t) = \sum_{i=1,3} A_i(z)\frac{1}{\sqrt{Z_0}}\mathbf{H}_i(\mathbf{r}_\perp)\exp i(\beta_i z - \omega_i t) + \text{c.c.} \tag{3.4b}$$

where the subscripts $i = 1$ and $i = 3$ refer to pump and third harmonic with angular frequencies ω_1 and $\omega_3 = 3\omega_1$ respectively, and the mode distributions $\mathbf{E}_i$ and $\mathbf{H}_i$ are power normalised:

$$\frac{1}{4}\int_{A_\infty} (\mathbf{E}_i \times \mathbf{H}_i^* + \mathbf{E}_i^* \times \mathbf{H}_i).\hat{\mathbf{z}}\, dA = 1 \tag{3.5}$$

The vacuum impedance term $Z_0 = \sqrt{\mu_0/\epsilon_0}$ is included so as to conform with the field definitions used by Grubsky [17] and conveniently provide the amplitudes $A_i(z)$ with units of $W^{1/2}$ so the power in each mode given simply by the square of its amplitude:

$$\iint_\infty S_z dA = \iint_\infty \langle \widetilde{\mathbf{E}}_i \times \widetilde{\mathbf{H}}_i \rangle_t .\hat{\mathbf{z}}\, dA = |A_i(z)|^2 \tag{3.6}$$

By substituting Eqn. 3.4 into the expression for the nonlinear polarisation Eqn. 3.2 and applying the reciprocity theorem as shown in Appendix. B, the coupled mode differential equations describing the evolution of the TH along the fibre can be expressed as follows [17]:

$$\frac{dA_1}{dz} = -\alpha_1 A_1 + in^{(2)}k_1 \left\{ (J_1|A_1|^2 + 2J_2|A_3|^2)A_1 + J_3 A_1^{*2} A_3 e^{i\delta\beta z} \right\} \tag{3.7a}$$

$$\frac{dA_3}{dz} = -\alpha_3 A_3 + in^{(2)}k_1 \left\{ (6J_2|A_1|^2 + 3J_5|A_3|^2)A_3 + J_3^* A_1^3 e^{-i\delta\beta z} \right\} \tag{3.7b}$$

where $k_1 = 2\pi/\lambda_1$ is the pump's free space propagation constant, $\delta\beta = \beta_3 - 3\beta_1$ is the detuning, $n^{(2)} \approx 2.5 \times 10^{-20}$ $\mathrm{m^2W^{-1}}$ is the nonlinear refractive index coefficient, $\alpha_{1,3}$ are the losses, and the overlap integrals J_i are integrated over the nonlinear glass core area:

$$J_1 = \frac{1}{3}\iint_{A_{NL}} \left(2|\mathbf{E}_1|^4 + |\mathbf{E}_1^2|^2 \right) dA \tag{3.8a}$$

$$J_2 = \frac{1}{3}\iint_{A_{NL}} \left(|\mathbf{E}_1|^2|\mathbf{E}_3|^2 + |\mathbf{E}_1.\mathbf{E}_3|^2 + |\mathbf{E}_1.\mathbf{E}_3^*|^2 \right) dA \tag{3.8b}$$

$$J_3 = \iint_{A_{NL}} \left((\mathbf{E}_1.\mathbf{E}_3)|\mathbf{E}_1^*|^2 \right) dA \tag{3.8c}$$

$$J_5 = \frac{1}{3}\iint_{A_{NL}} \left(2|\mathbf{E}_3|^4 + |\mathbf{E}_3^2|^2 \right) dA \tag{3.8d}$$

Of these, J_3 is the most important as it gives the overlap between the pump and TH modes and therefore dictates how rapidly the power can be exchanged between them along the waveguide. J_1 and J_5 govern the self phase modulation (SPM) of the pump and harmonic wave respectively, whilst J_2 relates to the cross phase modulation (XPM). All overlaps are listed in Table 3.1 on p. 23.

Fig. 3.3 shows the values of the overlap integrals for some of the phase match points

listed earlier. For 1.03 μm and 1.55 μm pumps, the $HE_{12}(3\omega)$ mode overlap is largest at 0.76 μm^{-2} and 0.38 μm^{-2} respectively; and therefore represents the best candidate for achieving efficient THG. This is due the HE_{12} mode containing a large peak in the centre which coincides with the peak of the fundamental pump field, as illustrated in Fig. 3.4. On the other hand, it is clear that increasing the hybrid mode number m introduces more radial oscillations and zeroes in the field profile, which generally reduces the overlap with the pump. The same is true of modes with higher azimuthal number ν, and hence the overlap with most other modes is over an order of magnitude smaller (only the $HE_{31}(3\omega)$ overlap is comparable).

Note that the overlaps for a 1.03 μm pump are slightly greater than for a 1.55 μm, since the phase matching occurs at a narrower diameter with greater modal confinement. Unfortunately, the TH from a 1.03 μm pump would be in the UV range where standard SMF shows strong absorption by the traditional germanium and phosphorous dopants.

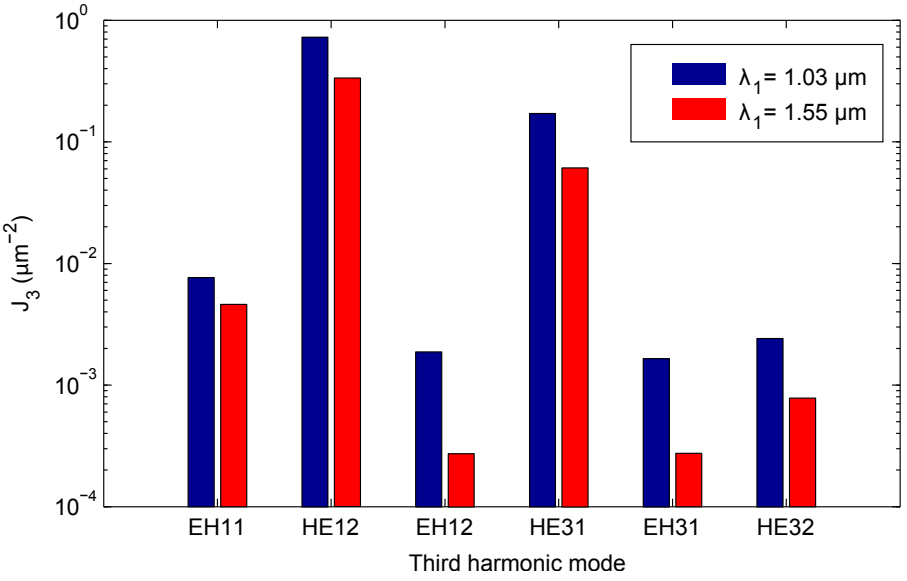

FIGURE 3.3: The pump-harmonic overlap integral J_3 evaluated for different harmonic modes using a 1.55 μm and 1.03 μm pump.

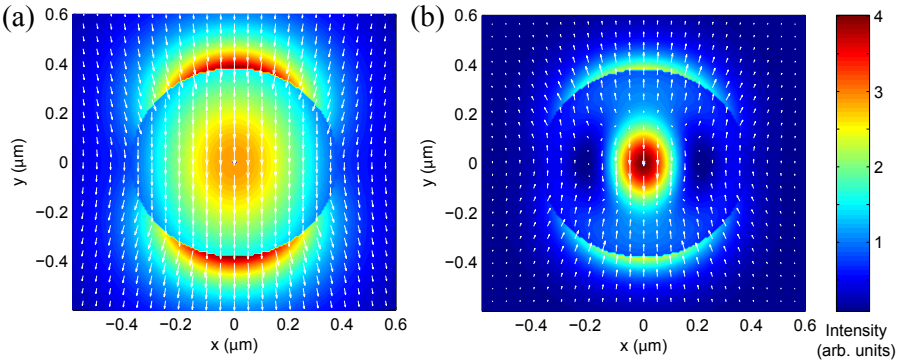

FIGURE 3.4: The electric field intensity $|\mathbf{E}|^2$ and transverse vector plot for (a) the $HE_{11}(\omega)$ pump mode at 1.55 μm and (b) the $HE_{12}(3\omega)$ harmonic mode at 0.517 μm.

As a result, the experiments in this work were carried out using a 1.55 μm pump so the resulting 517 nm harmonic signal could be easily coupled out.

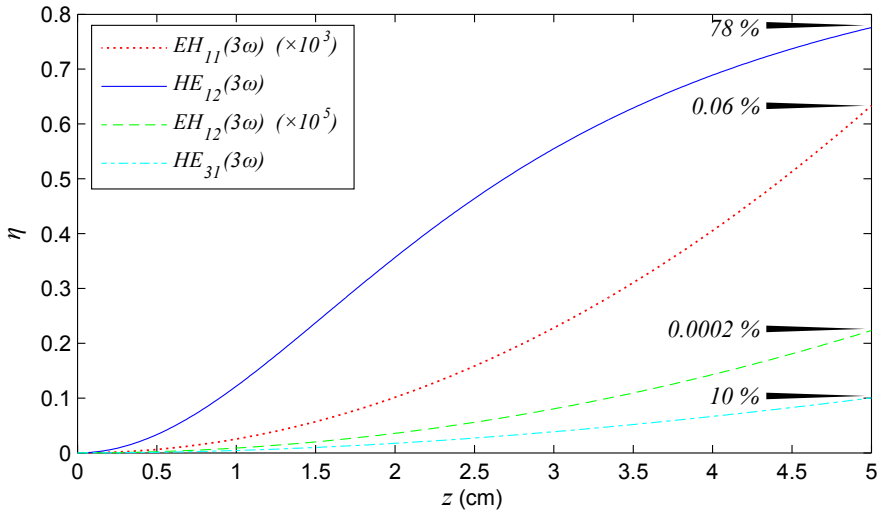

FIGURE 3.5: A comparison of the simulated conversion to different higher order harmonic modes using a 1 kW 1.550 μm fundamental mode pump. In each case, the microfibre diameter is chosen to ensure phase matching.

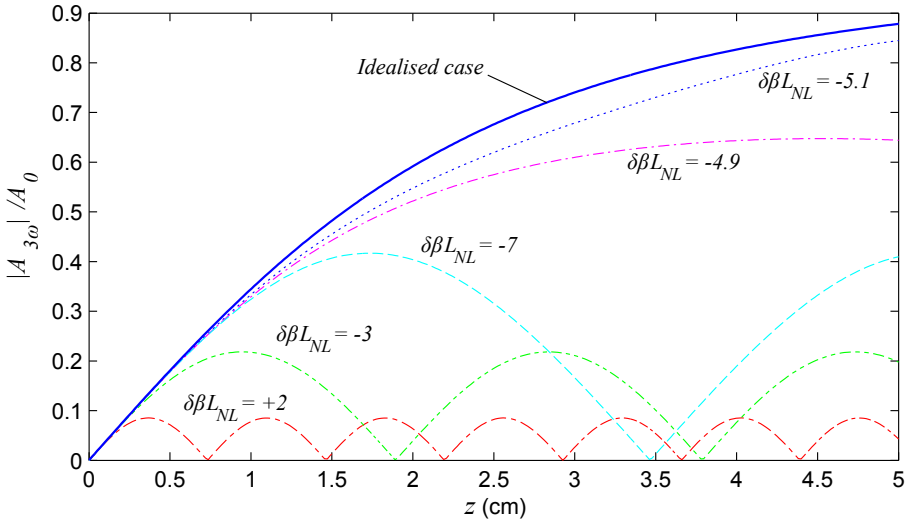

FIGURE 3.6: The normalised amplitude for the $HE_{12}(3\omega)$ mode for the ideal case ignoring nonlinear phase modulation effects (solid line) and various cases for different detunings $\delta\beta$ which account for SPM/XPM (dotted and dashed lines). Nonlinear length is L_{NL}. Pump parameters same as Fig. 3.5.

By applying the Runge-Kutta method to solve the coupled ODEs in Eqns. 3.7, the expected conversion efficiency for each harmonic mode was simulated as shown in Fig. 3.5 assuming a 1 kW pump at 1.55 μm wavelength. For the $HE_{12}(3\omega)$ mode, close to $\eta \approx 80\%$ is possible over a 5 cm uniform microfibre. For short distances up to a centimetre, the harmonic signal grows quadratically, beyond which the conversion begins to plateau due to pump depletion and also to some extent the exchange in power between the pump and harmonic disrupting the delicate balance between the nonlinear phase and detuning

$\delta\beta$. This plateauing is not observed for the other modes' conversion graphs, since their efficiencies are much lower. To faciliate comparison, the THG length L_{THG}, defined as the distance required to attain an efficiency of $\eta = 50\%$, is given for each mode in Table 3.1; for example, L_{TH} for the $\mathrm{HE}_{12}(3\omega)$ and $\mathrm{HE}_{31}(3\omega)$ modes are of the order of cm. The potential for such efficient conversion over a short distances ensures that competing nonlinear effects can be minimised, in particular those which grow exponentially with distance such as stimulated Raman or Brillouin scattering [24].

In Fig. 3.5, the detuning was optimised to ensure maximum conversion after propagating along 5 cm. From Eqn. 3.7, the optimum detuning $\delta\beta_0$ for harmonic growth can be calculated by incorporating the phase contributions from XPM and SPM:

$$\delta\beta_0(z) = -3n^{(2)}k_1\big[(2J_2 - J1)P_1(z) + (J_5 - 2J_2)P_3(z)\big] \tag{3.9}$$

At the start of the microfibre, the condition reduces to:

$$\delta\beta_0(0) = -3n^{(2)}k_1(2J_2 - J1)P_0 \tag{3.10}$$

where P_0 is the input pump power. To investigate other values of detunings, Fig. 3.6 plots the normalised amplitude $|A_3|/A_0$ against normalised detuning $\delta\beta L_{\mathrm{NL}}$ (where $L_{\mathrm{NL}} = 1/(n^{(2)}k_1J_1P_0)$ is the nonlinear length and roughly 1 cm). Firstly, it can be seen that the optimal detuning is around $\delta\beta L_{\mathrm{NL}} = -5$. This value is non-zero owing to combined effects of the SPM and XPM terms in the ODEs, but nonetheless is close enough to zero for the phase matching condition of $n_{\mathrm{eff}}\ (\omega) \approx n_{\mathrm{eff}}\ (3\omega)$ to hold. When detuned either above or below this optimum value, the harmonic amplitude falls and begins to show a sinusoidal dependance on distance, indicating a periodic exchange of energy between the pump and TH mode as expected for a phase mismatched scenario. Furthermore, the power conversion falls significantly: for $\delta\beta L_{\mathrm{NL}} = 2$, the conversion is limited to about 1%.

The effect of detuning on the output harmonic amplitude from a 5 cm OM is further explored in Fig. 3.7(a) and (b), whilst Fig. 3.7(c) shows the corresponding diameter for the given detuning range. The TH amplitude resembles a *sinc* function of $\delta\beta$ (similar to what might be expected for SHG with an undepleted pump), but is asymmetric about the peak and offset from zero by $-500\ \mathrm{m}^{-1}$ due to nonlinear phase modulation. It is clear that the conversion efficiency only peaks over a very narrow range which would demand an impossibly high tolerance of < 0.1 nm; this unfortunately cannot be achieved using silica glass given that it is comparable to molecular dimensions. The range over which the conversion envelope exceeds 1% is however more lenient ($-1400\ \mathrm{m}^{-1} < \delta\beta < 200\ \mathrm{m}^{-1}$) but nonetheless requires nm accuracy. It is unlikely that microfibres can be consistently and repeatably tapered within this range, but if the waist is deliberately fabricated slightly smaller than the critical diameter, there will be two segments (in the uptaper and downtaper) over which this diameter criteria is satisfied. With this approach, the

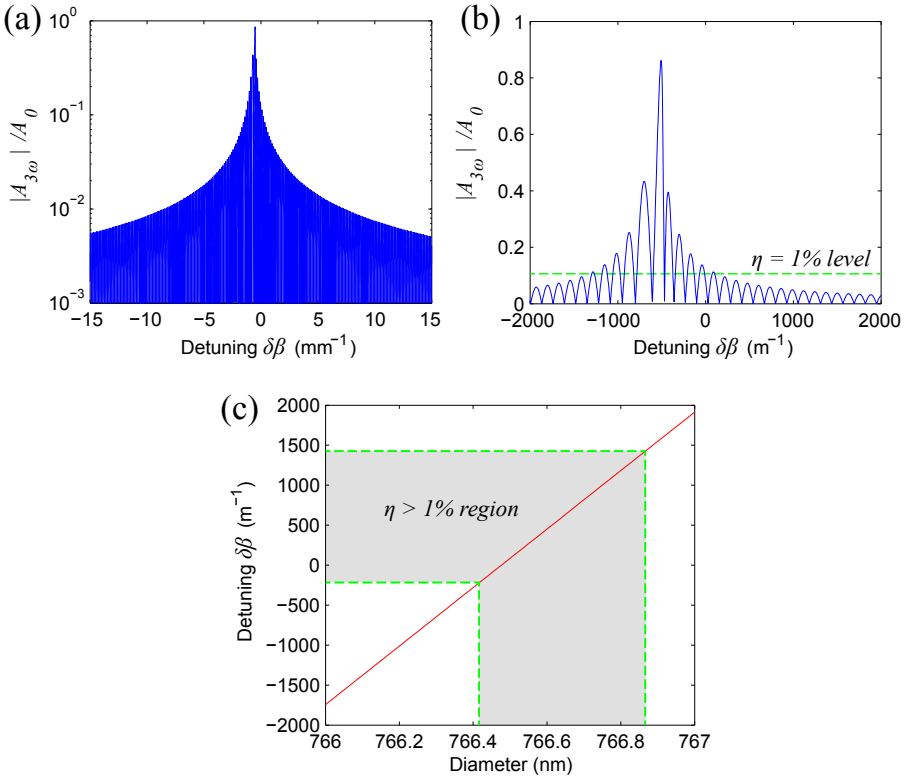

FIGURE 3.7: (a) The effect of detuning $\delta\beta$ on the amplitude conversion and (b) a close up of the highest conversion regime for THG with the $HE_{12}(3\omega)$ mode. (c) The detuning corresponding to different microfibre diameters. $P_0 = 1$ kW and $\lambda_1 = 1.55$ μm.

transition regions would have to be several centimetres long to maximise THG, whilst the length of the waist itself is insignificant. Alternatively, if the pump is tunable, the wavelength can be adjusted until it phase matches in the waist.

The sensitivity of the conversion to diameter variations also depends upon the choice of phase match point, in particular, the slope of the n_{eff} vs D graph at the point of intersection between the pump and harmonic n_{eff} curves. For example, in Fig. 3.1(b) at the $HE_{12}(3\omega)$ phase match point, the slope is steeper than that of the $HE_{32}(3\omega)$ point, which implies a greater detuning $\delta\beta$ for a given diameter offset. Nonetheless, the higher conversion offered by the $HE_{12}(3\omega)$ mode outweighs any benefit in terms of diameter sensitivity from using the $HE_{32}(3\omega)$ mode or other high order modes.

3.4 Experiments

Having presented the theoretical considerations for third harmonic generation in the previous section, the following discussions will outline the procedure for manufacturing the tapers, before analysing the resulting harmonic spectra which were recorded. Broadly, these experiments can be divided into two main categories:

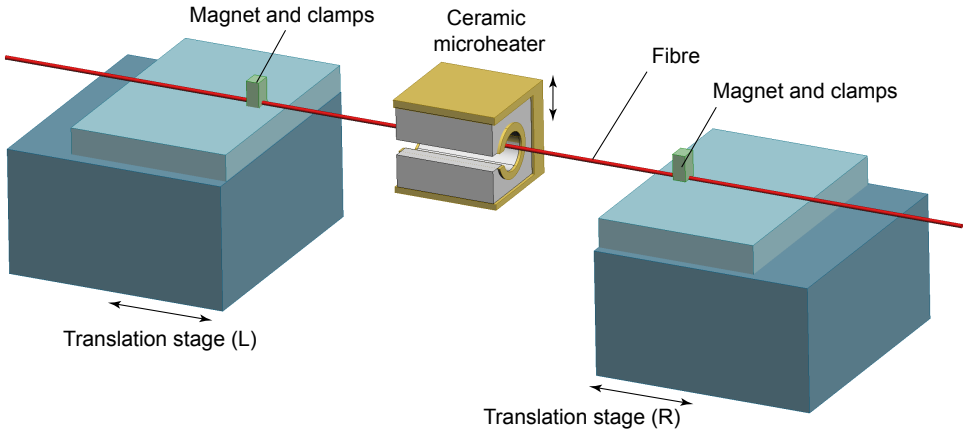

FIGURE 3.8: Schematic of the tapering rig. Both translation stages are computer controlled, and the height of the microheater can be manually adjusted.

1. Short tapers with waist lengths of a few mm, with phase matching in the uniform waist region to give high conversion at a specific wavelength.

2. Longer tapers, with THG occuring instead in the transition regions which are purposely extended over several cm to increase the conversion bandwidth (albeit at reduced efficiency).

Parts of the experimental work were carried out in collaboration with Yongmin Jung (ORC, University of Southampton) and Kotya Karapetyan (University of Bonn), and pump source components were loaned from Christophe Codemard (SPI Lasers, UK). Scanning electron microscopy of microfibre samples was conducted by Ming Ding (ORC, University of Southampton).

3.4.1 Taper fabrication

The tapers were fabricated from standard SMF (SMF-1300/1500-9-125-0.25-L, OZ Optics, Canada) in-house at the ORC using the modified flame brushing method [61] as shown in Fig. 3.8. The fibre is tensioned in the rig by two computer controlled stages and translated back and forth through a stationary ceramic heater at roughly 1320 ^{o}C until the desired microfibre diameter is reached. Compared to the more commonly used flame burner, the heater's wide hot zone of 4 mm offers more uniform heating. The taper diameter profile is adjusted by setting the gradient parameter α_t [62] in the stage control algorithm, where $\alpha_t = 0$ corresponds to a parabolic profile with a short waist and shallow transition regions, whilst $\alpha_t = 1$ represents the opposite extreme with much steeper transition regions. For the short tapers with total lengths of a few cm, α_t is chosen as zero to ensure an adiabatic transition for the pump mode in the downtaper (and of the harmonic mode in the uptaper), whereas for the longer tapers whose the total length range between 3 to 4.5 cm, a higher value of $\alpha_t \approx 0.3$ can be used without any adiabacity issues.

Taper Ref.	**Diameter (μm)**	**Waist Length (mm)**	η **(Experimental)**	η **(Theory)**
A	0.75±0.05	1±0.1	5×10^{-5}	1×10^{-3}
B	0.75±0.05	2±0.1	3×10^{-4}	5×10^{-3}
C	0.78±0.05	4±0.1	3×10^{-3}	2×10^{-2}

TABLE 3.2: Details for three of the characterised short tapers. Diameter profile parameter is $\alpha_t = 0$ for all tapers, and the experimental efficiencies are evaluated at 1.3 kW peak power.

3.4.2 Harmonic generation in short tapers

Results from the three short tapers listed in Table 3.2 are analysed in this section; tapers A and B were fabricated using the aforementioned rig, whilst taper C was produced by the University of Bonn and investigated at the ORC as a collaborative effort in 2009. All tapers have a diameter in the range 0.75-0.78 μm, so as to phase match with the $HE_{12}(3\omega)$ mode which is predicted to have the greatest overlap with the pump.

During the fabrication of tapers A and B, the pump was launched into the fibre and the output passed through a shortpass filter with a 1300 nm cut off wavelength to attenuate the pump before being monitored on a spectrum analyser (Yokogawa AQ-6315A), as illustrated in Fig. 3.9. The shortpass filter is a straightforward bend-loss filter formed by coiling the output fibre (the harmonic signal is not significantly affected as the loss is only 5 dB at $\lambda = 0.5$ μm). In this way, it is possible to simultaneously observe the TH spectrum in-situ whilst the taper diameter narrows. The pump source at $\lambda_1 = 1.55$ μm is fully fiberised and provides 4 ns pulses at a repetition rate of 100 kHz and peak power of up to 1.3 kW (further details about the source properties and construction are given in Appendix A). Using nanosecond pulses minimises walkoff issues, whilst maintaining high average and peak powers of $P_{\text{av}} = 0.5$ W and $P_0 = 1.25$ kW respectively which were well tolerated by the microfibre. The relatively long pulses can also be considered as quasi-continuous waves, a regime in which the aforementioned THG differential equations which exclude dispersive terms (Eqns. 3.7) are a good approximation. Prior to entering the taper, the pump pulses' full-width at half-maximum (FWHM) linewidth is typically less than 0.5 nm since the preceding SMF is limited to 2 m at most.

During tapering, as the core diameter approached the phase matching diameter, the TH signal increased slightly at first, before suddenly peaking at a much larger value (and then decaying away if the diameter continued to fall). These observations differ with those described by Grubsky et al., who reported a much sharper TH onset [17]. The discrepancies maybe due to the slightly higher pulse power used in this set up, so the diameters close to the critical value may in fact be matching to the nonlinearly broadened wavelength components of the pulse rather than the central wavelength at 1.55 μm). Once the TH signal appears, the tapering process can be immediately halted at the critical diameter. However, due to the thermal-optic and thermal expansion/contraction

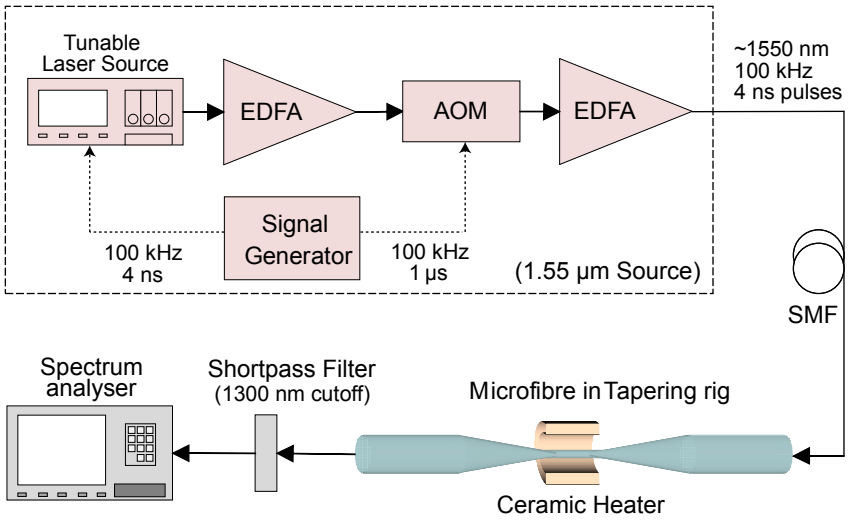

FIGURE 3.9: The $\lambda_1 = 1.55$ μm fiberised pump source schematic and the experimental set up for the observing the third harmonic whilst tapering fibre.

effects dn/dT and dD/dT, the final taper is often imperfectly phase matched, in which case the tunable laser source (TLS) wavelength from the pump can be adjusted.

The third harmonic spectra for taper A are presented in Fig. 3.10. As the estimated uniform waist length is 1 mm, the conversion (evaluated for $P_1 = 1.2$ kW) was consequently relatively low at $\eta = 10^{-5}$. The conversion is roughly two orders of magnitude lower than expected, due to imperfect phase matching. The asymmetry of third harmonic spectrum (also reported by Akimov et al. [15]) is largely due to the longer pump/TH wavelengths being phase matched within the transition regions (which possess a range

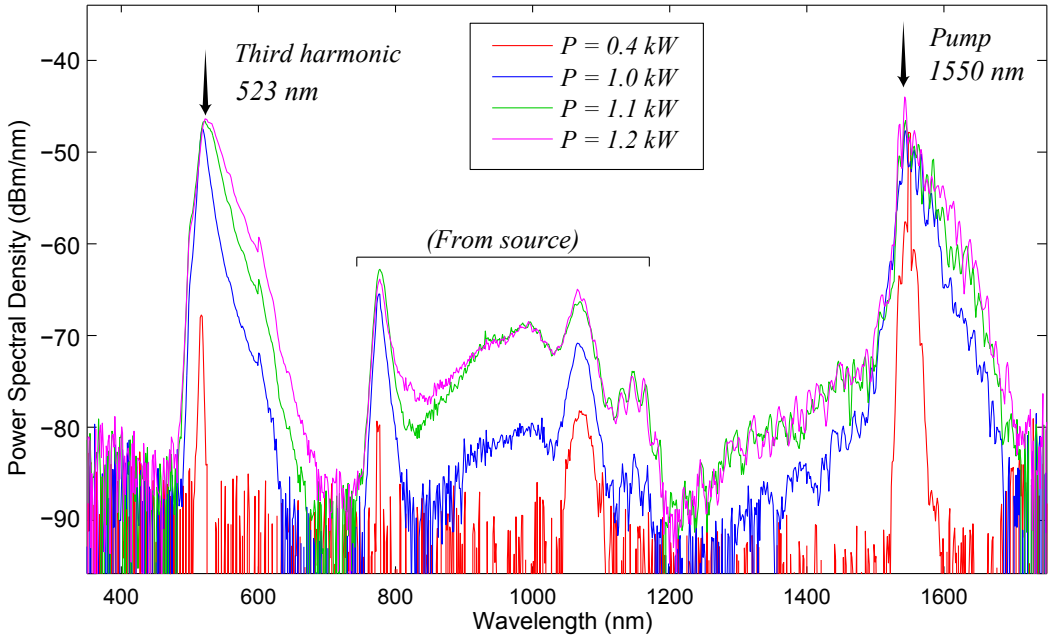

FIGURE 3.10: Output spectrum from taper A, showing the third harmonic at different pump powers. $D = 0.75 \pm 0.05$ μm, waist length 1 ± 0.1 mm.

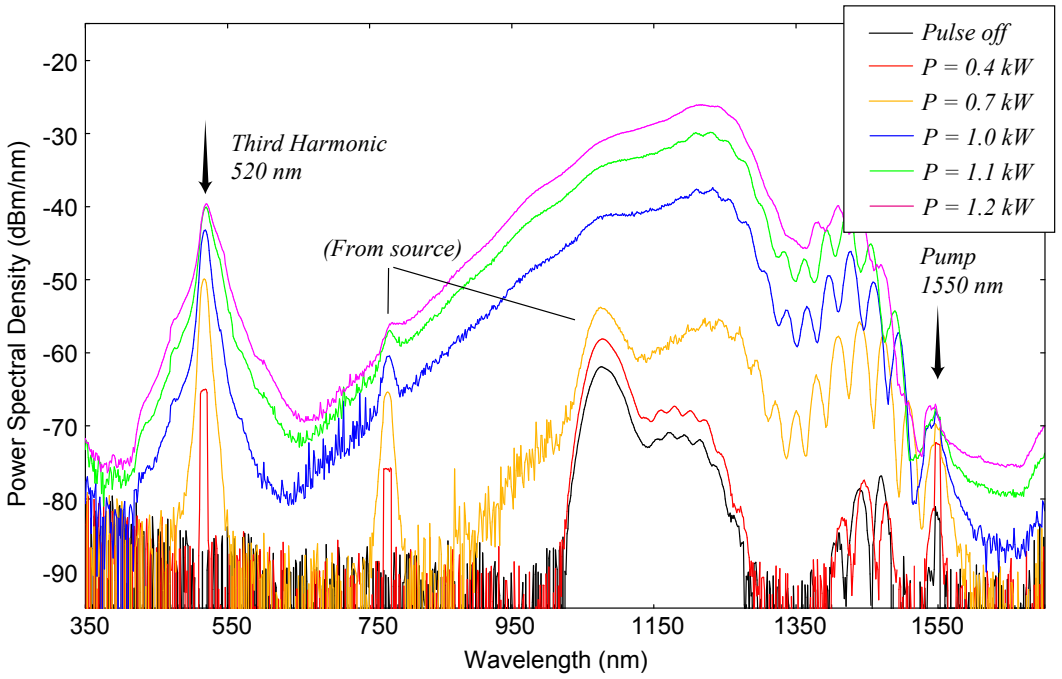

FIGURE 3.11: Output spectrum from taper B, showing the third harmonic at different pump powers. Taper diameter $D = 0.75 \pm 0.05$ μm, waist length 2 ± 0.1 mm.

of diameters larger than that of the waist) so the TH peak appears skewed to longer wavelengths. This spectral asymmetry is further exacerbated if the diameter exceeds the critical value for phase matching, as is likely the case here, because the TH will only be generated by the long-wavelength side of the pump peak.

At low pump powers (400 W), the third harmonic signal range is narrow (10 nm) but for powers approaching 1 kW, the range broadens due to the pump broadening from SPM, which is strongly enhanced by the tight modal confinement [63].

Taper B was fabricated with the same diameter as taper A, but with a longer waist length of approximately 2 mm. The third harmonic spectrum given in Fig. 3.11 indicates that the harmonic peak is indeed greater by 5 dB, and visually a slight green glow could be observed with the naked eye. The position of the peak at 520 nm, which is closer to the expected $\lambda_1/3 = 517$ nm than the peak of taper A, indicates that the diameter is slightly closer to the target phase matching diameter of 0.77 μm. A conversion efficiency 10 times lower than the simulated value of 10^{-3} was obtained, most likely due to the waist being slightly parabolic rather than uniform.

Finally, some interesting comparisons can be made with the spectrum for the 4 mm taper C, shown in Fig. 3.12. In 2009, the taper was brought to the ORC by Konstantino (Kotya) Karapetyan from the Uni. Bonn, Germany and the TH spectrum was characterised along with the help of G. Brambilla, Yongmin Jung and Christophe Codemard (SPI Lasers). The more severe spectral asymmetry and third harmonic wavelength of

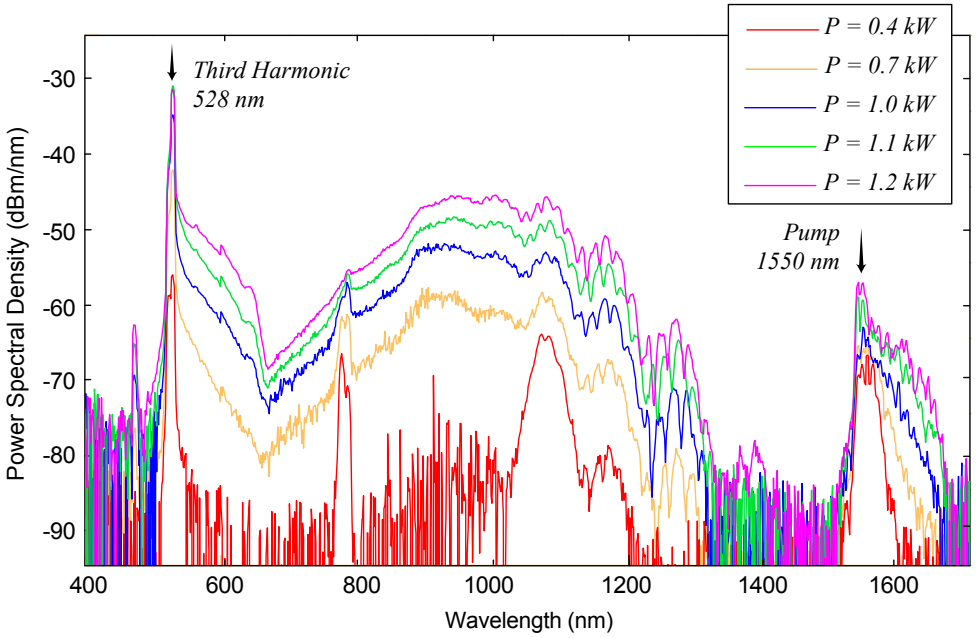

FIGURE 3.12: Output spectrum from taper C. Taper diameter $D = 0.78 \pm 0.05$ μm, waist length 4 ± 0.1 mm.

528 nm (rather than 517 nm) imply that the diameter is in fact more strongly detuned from the phase match point than the other 2 tapers. Despite this, the TH peak is over an order of magnitude higher than the other two tapers since the waist length is roughly 4 times longer, and the harmonic power would be expected to grow quadratically with distance. The efficiency was estimated at 10^{-3} - for comparison, the maximum value reported in literature so far is 0.05% at 10 kW pumping by Akimov et al. [15].

Another feature of taper C's TH spectrum, absent in A and B, is the sharper and more pronounced peak at 528 nm which is 15 dB higher than the neighbouring TH wavelengths. This is again due to the longer waist length over which the 528 nm signal can grow, whereas the neighbouring TH wavelengths, generated in the microfibre's transition regions, cannot develop to the same amplitude.

From the spectra, it can be seen that a potential limit to the maximum achievable efficiency is the broadening of the pump, which is significant even for taper waists of a few mm. For longer tapers this is clearly an issue, but could be mitigated by limiting the pump peak power or perhaps using a different phase match point with a larger diameter, such as $\mathrm{HE}_{11}(\omega) \rightarrow \mathrm{EH}_{31}(3\omega)$, at the expense of reduced efficiency.

To study the power dependance further, Fig. 3.13 plots the cube root of the third harmonic power against the pump power. Taper C shows a fairly linear fit, indicating that the third harmonic power $P_{3\omega}$ increases cubically with pump power as one would expect from Eqn. 3.7a when $\mathrm{A}_3 << A_1$. However, for taper B the pattern is inconclusive. This is perhaps because the taper is shorter, so the fraction of the TH generated in the

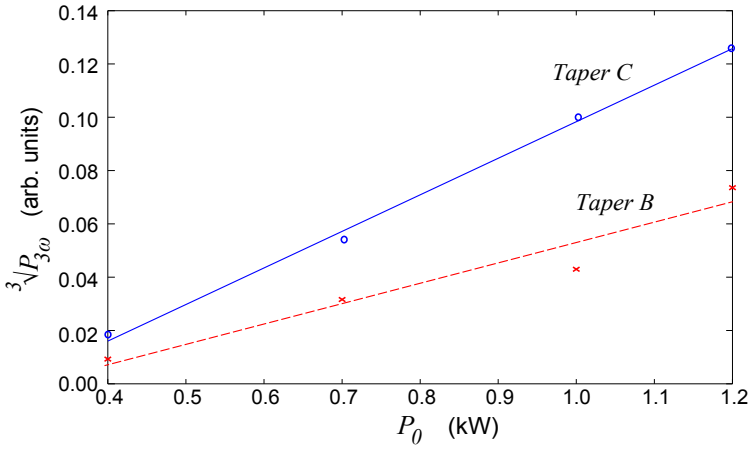

FIGURE 3.13: A plot of the cube of the third harmonic power ($\sqrt[3]{10^{0.1P_{3\omega}^{\mathrm{dB}}}}$) against pump peak power for tapers B and C.

Taper Ref.	**Diameter (μm)**	$\boldsymbol{\alpha_t}$	**Total Length L (mm)**	η **(Experimental)**	max η **(Theory)**
D	2.1±0.05	0.3	45±0.5	1×10^{-4}	4×10^{-3}
E	1.8±0.05	0.1	45±0.5	5×10^{-5}	4×10^{-3}
F	2.4±0.05	0.3	30±0.5	1×10^{-4}	2×10^{-3}

TABLE 3.3: Details for three of the characterised long tapers. Theoretical η is estimated for phase matching to the several TH modes along the transition region. Total length L includes both transition regions. Experimental η values are calculated at a pump power of 1.2 kW.

transition regions (corresponding to wavelengths other than $\lambda_1/3$) is relatively larger; hence increasing the pump peak power does not necessarily lead to a cubic increase in total TH power.

3.4.3 Long tapers for broadband third harmonic generation

3.4.3.1 Experiment overview

Here, we discuss experiments using longer tapers with total lengths $L > 3$ cm (including both transition regions and the waist) wherein the intermodal phase matching occurs within the range of diameters available in the transition regions, to collectively permit harmonic generation over a wider range of pump wavelengths. This bandwidth-extension technique is somewhat analogous to chirping the poling period of quasi phase matched devices [64], and can potentially allow broad third harmonic continua with broader spectral ranges to be generated in the green down to the UV wavelengths for applications such as biological spectroscopy or detection.

We focus in particular on the properties of the three long tapers listed in Table 3.3. The length and value of α_t were chosen to maximise the length of the transition region in the

range where the diameter is about 2 μm where several phase match points exist. Rather than scrutinising the full output spectrum of each taper, this section will expound upon the differences between short and long tapers and also examine specific attributes from each taper, such as its response to the pump power level or wavelength detuning.

From scanning electron microscope (SEM) images recorded with the help of M. Ding (ORC, University of Southampton), Fig. 3.14(a) summarises the reconstructed profile of taper A's downtaper. The uptaper is identical and tapers B and C contain similar transition regions. The diameter falls exponentially ($\sim \exp(-0.31\ \mathrm{mm}^{-1} z)$) which gives a shallow gradient close to the phase matching diameter of 2 μm, thus ensuring a sufficient interaction length for the harmonic to grow. The diameter near the waist is roughly uniform over 3 mm. A low surface roughness with diameter variations < 10 nm is also confirmed by the SEM images taken along the taper, shown in Fig 3.14(b-d).

The experimental set up and fabrication technique are the same as described for the shorter tapers in the previous section and Fig. 3.9. For taper F, the tapering process was stopped just after the third harmonic signal peaked, but both tapers D and E were deliberatly pulled for a slightly longer time to give a narrower waist which shifts the phase matching further within the transition region.

3.4.3.2 Simulations

Fig. 3.15 plots the predicted phase matching wavelength at different diameters for $\nu = 1, 3$ hybrid TH modes. When compared with the profile of taper D, it is clear that a 1.55 μm pump can potentially phase match to several modes, including the $EH_{31}(3\omega)$,

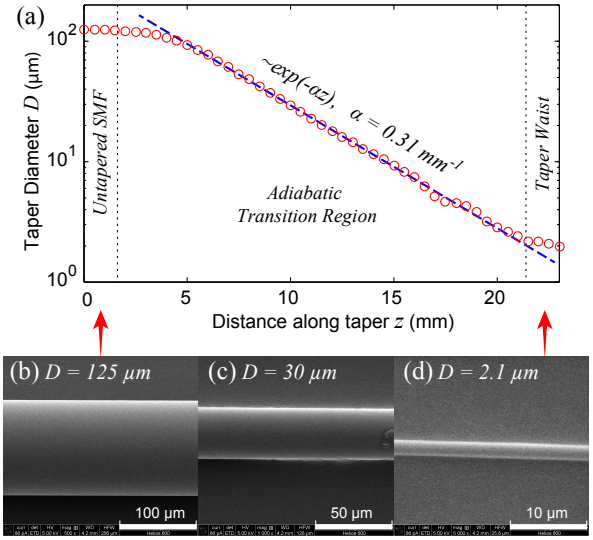

FIGURE 3.14: (a) The diameter profile for the transition region of taper D ($D = 2.1$ μm and $L = 45$ mm) characterised from SEM images, showing an exponential decreasing diameter along the taper. (b-d) SEM images of the taper at the start, transition region and waist.

$EH_{12}(3\omega)$, $HE_{32}(3\omega)$, and $HE_{13}(3\omega)$ modes, albeit at different points along the transition region. Indeed, since any taper with a waist narrower than D=2.5 μm will permit phase matching with these four modes at various positions, we shall refer to this as the critical diameter. To assess the relative contribution of the modes, the modal overlaps J_3 between the pump and each mode were calculated and found to be similar in the range of $10^{-4} < J_3 < 10^{-3}$ μm^{-2}. We therefore expect each of the modes to contribute a significant fraction to the third harmonic signal power at the taper output. Although the overlap with the $\text{HE}_{12}(3\omega)$ mode at $D = 0.77$ μm is greater, the key aim of the current experiment is to increase bandwidth and so we focus on the phase match points at larger diameters, which can be more consistently fabricated with longer lengths and tolerate higher peak pump powers (exceeding kW levels for ns pulses).

3.4.3.3 Results and discussion

When the long tapers' waist neared the phase matching diameter during the tapering process, the THG signal took several minutes attain its peak conversion, unlike previous experiments with short tapers where the onset of THG appeared over seconds. This observation occurs mainly because the longer microfibres are drawn slower (i.e. smaller dD/dt) when the diameter approaches a few microns because the stages move at a fixed speed and hence take a longer time to physically translate the length of the microfibre through the heater. Secondly, a narrower waist diameter decreases the minimum pump

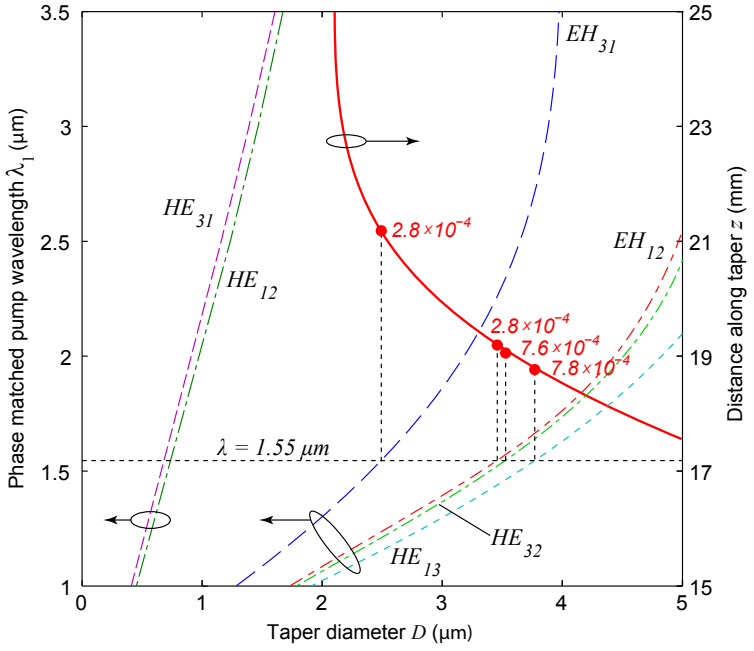

FIGURE 3.15: The phase matched pump wavelength (left) against microfibre diameter, when matching to different third harmonic modes. The corresponding diameter-distance profile for taper D (right) is also shown, and the red dots indicate positions where a $\lambda_1 = 1.55$ μm pump would phase match. At each point, the overlap integral J_3 is given in units of [μm^{-2}].

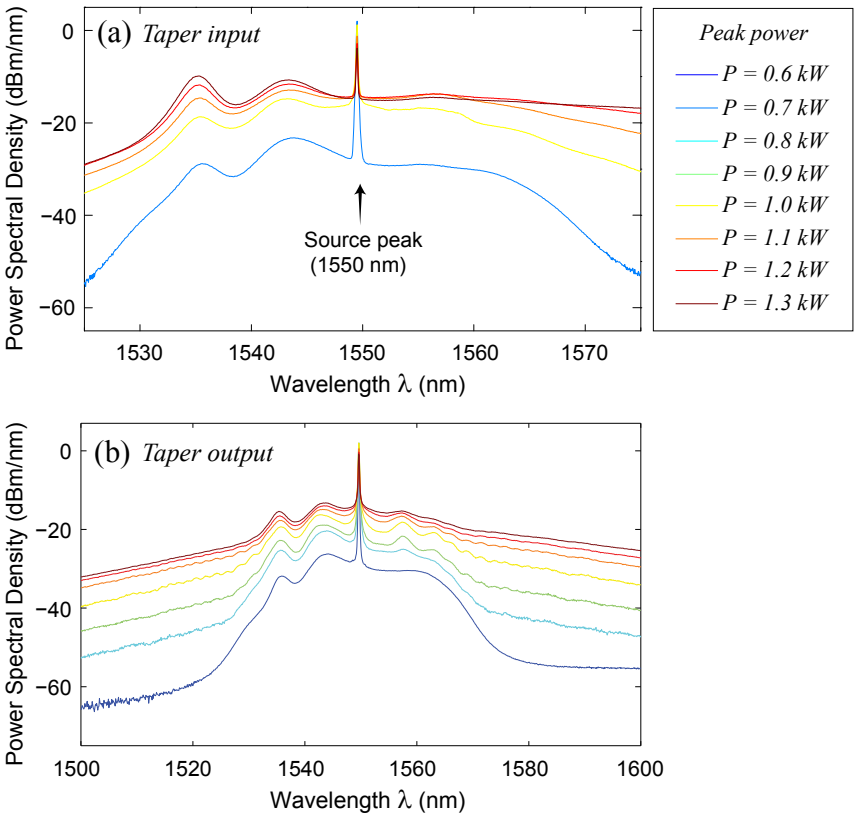

FIGURE 3.16: (a) The pump spectrum measured via a -25 dB coupler from the source output and also (b) at the taper output with an input pump wavelength of $\lambda_1 = 1.55$ μm.

wavelength (from the broadened pump spectrum) which can be phase matched. Hence, as this limit approaches the 1550 nm pump peak, the THG peak is expected to gradually rise. Indeed, as the waist narrowed from 3.3 μm to 2.4 μm, the TH peak grew by 25 dB whilst simultaneously falling from 600 nm to 520 nm as expected from Fig. 3.15. Furthermore, the TH signal remains even after the waist diameter falls several hundred nanometres below the critical value (although the peak is reduced by over 10 dB) which implies that the locale of THG has shifted away from the waist into the transition regions.

For taper D, the pump spectrum before and after the taper is shown in Fig. 3.16(a-b), characterised via a -25 dB coupler, whilst the harmonic spectrum is given in Fig. 3.17. The input pump pulse is initially narrowband with a FWHM linewidth < 0.5 nm, but undergoes nonlinear broadening to over several hundred nanometres as it enters the taper. These broadened components are subsequently phase matched along the uptaper, resulting in the measured broadband THG spectrum. Comparison of the pump spectrum before and after the taper in Figs. 3.16 (a) and (b) verifies that the pump broadening is more significant at higher powers – for example, at 1.3 kW peak power, the power at 1525 nm was measured from the source as -29 dBm/nm (being comprised largely of CW ASE rather than the pulse) but increases to -24 dBm/nm after the taper. Additionally,

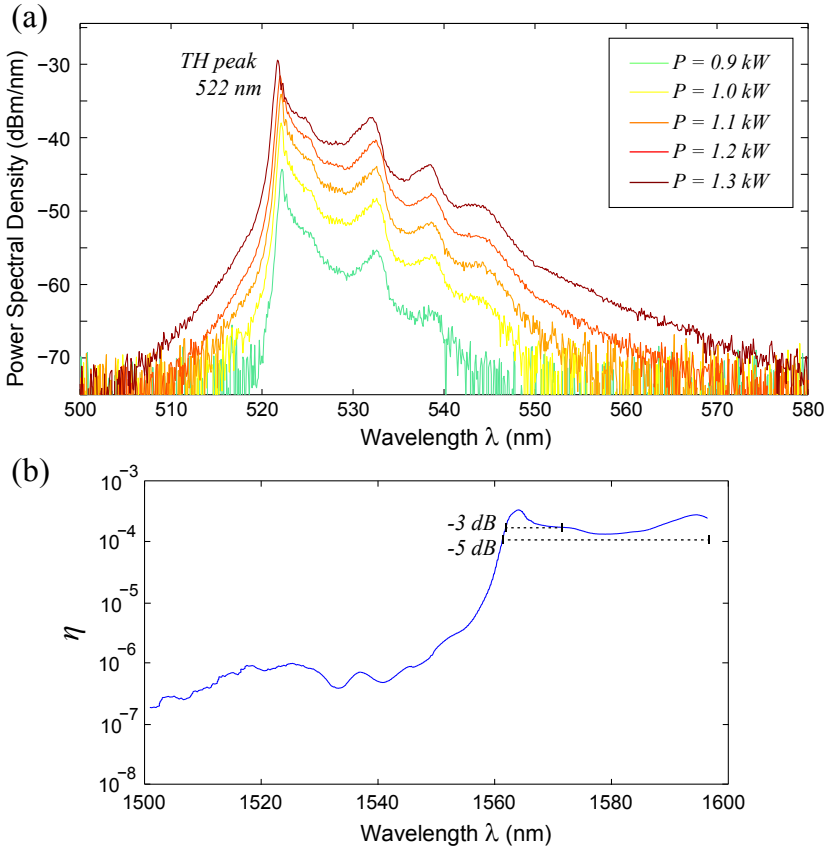

FIGURE 3.17: (a) The third harmonic spectrum for taper D, measured after a short-pass filter with approximately 5 dB loss. (b) The estimated experimental conversion efficiency at each of the pump wavelengths. Taper D parameters: $D = 2.1$ μm and $L = 45$ mm.

the side peaks in Fig. 3.16(b) were observed, which did not exist in the original source spectrum, possibly due to nonlinear effects such as self phase modulation and modulation instability. Note that these are partially masked by the source's background amplified spontaneous emission peaks, which are CW and low power (with a cumulative total power of 0.1 W) and hence do not contribute to the THG.

Aside from the distinct peak at 522 nm, there exist also the third harmonic of the secondary peaks and broadened components at longer wavelengths in the harmonic spectrum of Fig. 3.17. The shape of the TH signal is to some extent dictated by the generation of multiple third harmonic modes, which contribute their individual conversion spectra. As the pump power increases from 0.9 kW up to 1.3 kW, these extend from 540 nm up to 570 nm. Whereas the components of the pump which broadened to longer wavelengths are able to phase match within the transition regions, the shorter wavelengths require a phase matching diameter narrower than the taper waist and hence cannot generate a detectable TH signal. The harmonic spectrum is therefore asymmetrically skewed towards longer wavelengths.

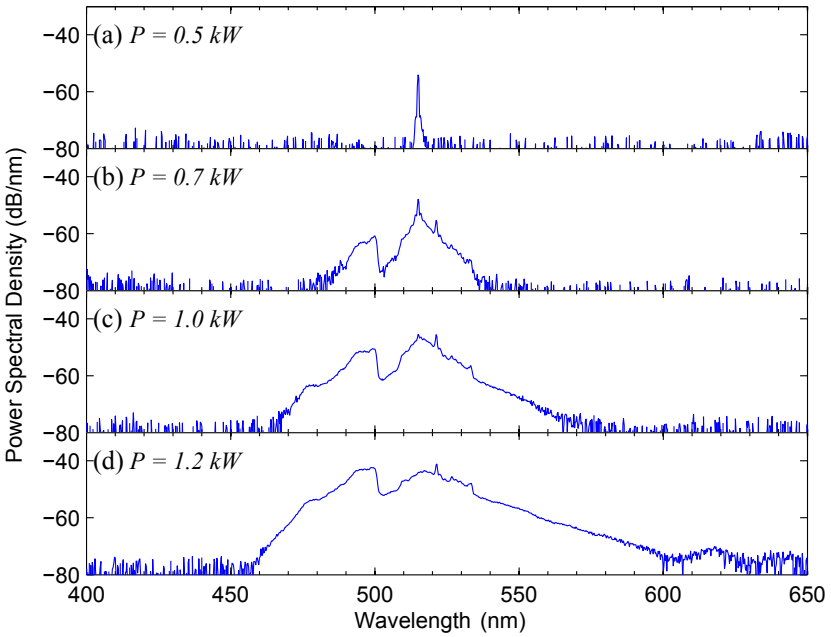

FIGURE 3.18: Third harmonic spectrum for different pump powers for taper E, showing broad TH signal detectable over 150 nm. Pump wavelength is $\lambda_1 = 1.55$ μm. Taper E parameters: $D = 1.8$ μm and $L = 45$ mm.

Calculating the efficiency over moving 5 nm steps at maximum pump power (10 μJ pulse energy) results in the conversion rates shown in Fig. 3.17(b). At $\lambda = 1550$ nm, the value of $\eta = 10^{-6}$ is low, but nonetheless comparable to that reported in published experiments with uniform diameter waveguides [16]. For shorter pump wavelengths, the conversion falls below 10^{-7} due to poor phase matching. On the other hand, for $\lambda > 1560$ nm, η rises by over a hundred-fold to more than 0.3×10^{-3} with a 5 dB bandwidth of at least 36 nm. From Fig. 3.17(b) it is also apparent that the true bandwidth may extend further to longer wavelengths, but confirmation would require a source for $> 1.6\mu$m L-band wavelengths and a longer wavelength OSA.

To study the dependency upon the taper profile further, taper E was purposely fabricated with a narrower waist of 1.8 μm. The resulting third harmonic output spectrum in Fig. 3.18 is over twice as broad as that of taper D and covers a wider range of 150 nm at $P = 1.2$ kW, because the shorter wavelength components of the pump are also able to contribute to the third harmonic signal. The TH spectrum therefore appears much more symmetrical and extends down to 450 nm (60 nm lower than for taper D). Compared to the THG in uniform waveguides in [15], this spectral width is an order of magnitude broader, despite pumping at a tenfold lower peak power. However, an important consequence of the narrower waist is that the efficiency of $\eta = 5 \times 10^{-5}$ is notably lower than that of taper D, since the THG occurs in a steeper part of the transition region.

Using powers below 0.7 kW provides a distinct THG peak as shown in Fig. 3.18(a) and (b) - in the latter, the secondary peaks are also visible. On the other hand, at

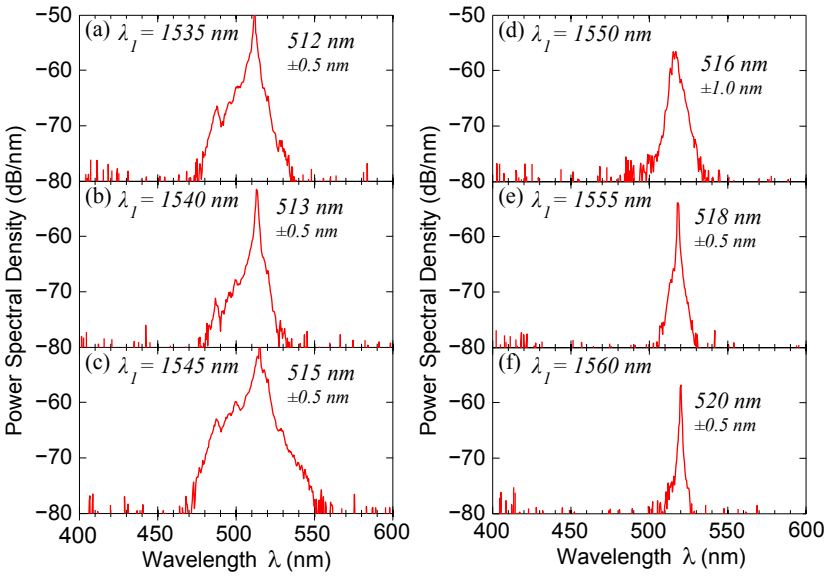

FIGURE 3.19: Third harmonic spectrum when the pump wavelength is tuned from 1535 nm to 1560 nm using taper F (D = 2.4 μm and L = 30 mm). Pump power is approximately P = 0.6 kW to minimise broadening.

higher powers the peak becomes masked by the nonlinear broadening as in (d) when $P = 1.2$ kW. This was not observed in the spectra of 3.16 (c) and can be attributed to a combination of the higher field intensity in the narrower taper E, as well as differences in their dispersion properties which vary strongly with fibre diameter.

Finally, to investigate the effect of tuning the pump wavelength λ_1 in more detail, taper F was fabricated with a shorter length of 30 mm with a diameter of 2.4 μm and characterised at the lower power of $P_0 = 0.6$ kW. These two changes intend to minimise nonlinear broadening so that a distinct TH peak can be identified and tracked during pump tuning, as shown in Fig. 3.19.

As λ_1 is tuned from 1535 nm up to 1560 nm, the TH peak wavelength is confirmed to vary as $\lambda_1/3$. For this taper, the THG from phase matching to the $EH_{31}(3\omega)$ third harmonic mode is likely to be dominant near the waist since the 2.4 μm diameter is very close to the critical diameter of 2.5 μm. However, due to the slight difference, the largest conversion occurs at the shorter wavelength of $\lambda_1 = 1545$ nm rather than 1550 nm.

Even when the pump wavelength is tuned over the wide 25 nm range, the TH peak level only varies by only 6 dB which implies the distribution of the corresponding phase matching diameters is fairly even in the transition region, in agreement with SEM characterisation. The slight narrowing of the TH peak when pumped at the longer wavelength of 1560 nm may be due to a fall in the gain spectrum of the source amplifier as well as the steeper taper gradient at phase matching position.

3.5 Conclusion

We have simulated the required phase matching conditions for third harmonic generation in silica microfibres and studied the different possible harmonic modes which can be obtained. Of these, the $HE_{12}(3\omega)$ exhibits the largest modal overlap with the fundamental pump mode and hence can offer the highest conversion, up to 80% over uniform 5 cm microfibre using a 1 kW 1.55 μm pump.

Experimentally, both short and long tapers for were fabricated and investigated for THG. For short tapers where THG occurs in the uniform waist, efficiencies up to 0.1% were obtained over 4 mm, but the bandwidth was limited to the order of nm. On the other hand, when using longer tapers where the phase matching occurs within the transition regions of several cm, broadband conversion is possible with 5 dB bandwidths in excess of 36 nm.

Chapter 4

Resonantly Enhanced Third Harmonic Generation

4.1 Overview

For THG in a microfibre, diameter fluctuations present a fundamental limitation to the efficiency. Whilst increasing the pump power would increase conversion quadratically, this also facilitates nonlinear pump broadening in the preceding fibre, which may be undesirable and furthermore reduce the power at the central pump wavelength. Also, extending the taper length will not improve the conversion unless a high uniformity can be maintained.

One solution is to configure the microfibre into a loop resonator architecture, in which the taper is self-coupled via its own evanescent field [20, 21]. The recirculation of the pump light on resonance will only locally enhance the electric field near the taper (including the region where harmonic generation occurs) and importantly, since the loop is usually only a few mm in length, this does not require diameter uniformity over long microfibre distances. Such a technique therefore offers an inexpensive method, with straightforward fabrication steps, to increase the efficiency without resorting to higher powers. We focus on the loop resonator since it is simplest of all microfibre resonators to fabricate, but alternative resonators such as the microcoil [23] or knot [22] would likewise offer resonant enhancement. A similar concept has also been previously applied to harmonic generation in ring resonators [65, 66, 67] and microtoroids [68],

In the following sections, resonantly enhanced THG in loop resonators will be first studied theoretically, before discussing the experimental observations.

4.2 Theoretical study

Here, we study the effect of the pump light resonance on the THG conversion, including the influence of the coupling and loss parameters (which both dictate the resonance characteristics) for a silica loop resonator. At higher powers, the transmission is modified by hysteresis, and the effect of bistability on the THG will be analysed, as well as the co-resonant case in which the harmonic signal is partially recirculated.

4.2.1 Theoretical modelling details

The ideal loop resonator geometry is illustrated in Fig. 4.1, formed from a microfibre arranged into loop and coupling regions with lengths L_0 and L_c respectively. Nonlinear phase modulation effects and third harmonic generation are assumed throughout the resonator. Typically, the diameter of a loop varies between several hundred microns to a centimetre, whilst the coupling length can vary considerably according to the tightness of the loop. The coupling coefficient between the adjacent OMs $\kappa_{\omega,3\omega}$ falls exponentially with their separation and so it can be assumed that the coupling is only significant over a small range $L_c \ll L_0$.

Here, we focus on simulations using the loop parameters listed in Table 4.1 which can be readily realized using manual stages without the need for specialist equipment after the microfibre is fabricated, with $L_0 = 3$ mm and $L_c = 50$ μm.

In order to phase match with the $\mathrm{HE}_{11}(\omega)$ mode with the $\mathrm{HE}_{12}(3\omega)$ harmonic mode, the OM diameter is chosen to be 767 nm, at which both the pump and harmonic modes have an effective index of $n_{\mathrm{eff}} = 1.08$ for a pump wavelength of $\lambda_1 = 1.55$ μm. Only

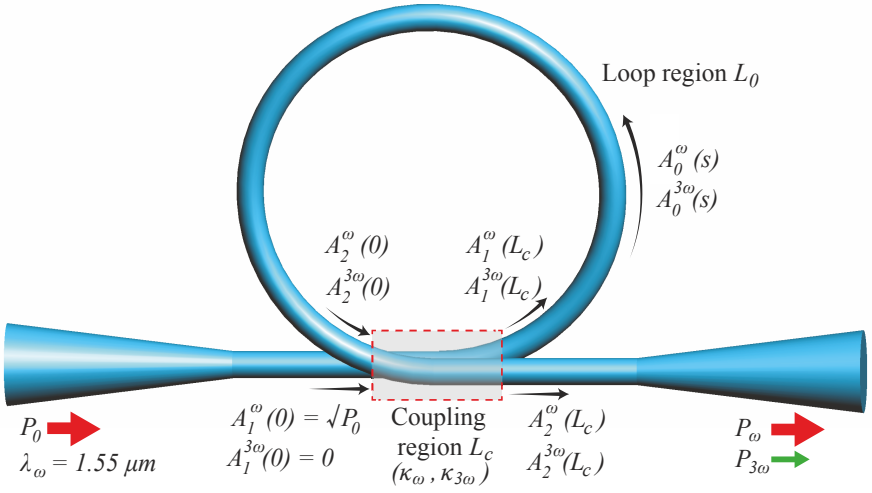

FIGURE 4.1: Microfibre loop resonator schematic. $A_1(z)$ and $A_2(z)$ represent the amplitudes in the each arm of the coupling region, and $A_0(s)$ is the amplitudes inside the loop.

Parameter	Symbol	Value
Pump SPM overlap	J_1	0.97 μm^{-2}
Pump XPM overlap	J_2	1.46 μm^{-2}
Harmonic-pump overlap	J_3	0.39 μm^{-2}
Harmonic SPM overlap	J_5	3.96 μm^{-2}
Loop length	L_0	3 mm
Coupling length	L_c	50 μm
Effective index	n_{eff}	1.081

TABLE 4.1: Summary of parameters used in the simulation of the loop resonator, when phase matching the $\text{HE}_{11}(\omega)$ mode with the $\text{HE}_{12}(3\omega)$ mode for $\lambda_1 = 1.55$ μm.

these two modes will experience any significant power exchange, since the microfibre is single-moded at $\lambda = \lambda_1$ with a V number of 1.6, and all other harmonic modes are far from phase matched.

In the loop region, the coupled mode differential equations describing the evolution of the co-propagating pump and third harmonic mode amplitudes A_0^{ω} and $A_0^{3\omega}$ are adapted from [17] to include loss:

$$\begin{aligned}\frac{dA_0^{\omega}}{ds} =& -\alpha_{\omega}A_0^{\omega} + in^{(2)}k_1\Big[(J_1|A_0^{\omega}|^2 \\ &+ 2J_2|A_0^{3\omega}|^2)A_0^{\omega} + J_3(A_0^{\omega *})^2A_0^{3\omega}e^{i\delta\beta s}\Big] \qquad (4.1a)\\ \frac{dA_0^{3\omega}}{ds} =& -\alpha_{3\omega}A_0^{3\omega} + in^{(2)}k_1\Big[(6J_2|A_0^{\omega}|^2 \\ &+ 3J_5|A_0^{3\omega}|^2)A_0^{3\omega} + J_3^*(A_0^{3\omega})^3e^{-i\delta\beta s}\Big] \qquad (4.1b)\end{aligned}$$

where the overlap integrals J_1, J_2, J_3 and J_5 correspond to the terms for pump self-phase modulation (SPM), cross-phase modulation (XPM), pump-harmonic overlap, and harmonic SPM respectively. Since the analysis will concentrate on the narrow range of wavelengths (< 1 nm) around a resonance, it is reasonable to approximate these overlaps as constants, with the values given in Table 4.1. The detuning is given by $\delta\beta = \beta_{3\omega} - 3\beta_{\omega}$, whilst $k_1 = 2\pi/\lambda_1$ is the pump free space propagation constant and $n^{(2)} = 2.7 \times 10^{-20}$ m^2/W is the silica nonlinear refractive index coefficient. In the coupling region, the equations for the amplitudes $A_i^{\omega}(s)$ and $A_i^{3\omega}(s)$ are similar albeit with the addition of the linear coupling terms:

$$\begin{aligned}\frac{dA_i^{\omega}}{ds} =& -\alpha_{\omega}A_i^{\omega} + i\kappa_{\omega}A_j^{\omega} + in^{(2)}k_1\Big[(J_1|A_i^{\omega}|^2 \\ &+ 2J_2|A_i^{3\omega}|^2)A_i^{\omega} + J_3(A_i^{\omega *})^2A_i^{3\omega}e^{i\delta\beta s}\Big] \qquad (4.2a)\\ \frac{dA_i^{3\omega}}{ds} =& -\alpha_{3\omega}A_i^{3\omega} + i\kappa_{3\omega}A_j^{3\omega} + in^{(2)}k_1\Big[(6J_2|A_i^{\omega}|^2 \\ &+ 3J_5|A_i^{3\omega}|^2)A_i^{3\omega} + J_3^*(A_i^{3\omega})^3e^{-i\delta\beta s}\Big] \qquad (4.2b)\end{aligned}$$

Eqns. 4.2 (a) and (b) give the differential equations for the modes $A_1^{\omega}, A_1^{3\omega}$, propagating in the first arm of the coupling region when $i = 1$ and $j = 2$; and likewise for the second arm $A_2^{\omega}, A_2^{3\omega}$, when $i = 2$ and $j = 1$. These equations are then solved iteratively with the boundary conditions for field continuity:

$$A_0^{\omega,3\omega}(0) = A_1^{\omega,3\omega}(L_c)\exp\left(i\beta_{\omega,3\omega}L_c\right) \tag{4.3a}$$

$$A_2^{\omega,3\omega}(0) = A_0^{\omega,3\omega}(L_0)\exp\left(i\beta_{\omega,3\omega}L_0\right) \tag{4.3b}$$

as well as the input initial conditions:

$$A_1^{\omega}(0) = \sqrt{P_0} \tag{4.4a}$$

$$A_1^{3\omega}(0) = 0 \tag{4.4b}$$

for an input pump power P_0. The output transmissions can then be evaluated as:

$$\frac{P_{\omega,3\omega}}{P_0} = \left|\frac{A_2^{\omega,3\omega}(L_c)}{A_1^{\omega}(0)}\exp\left(i\beta_{\omega,3\omega}L_c\right)\right|^2 \tag{4.5}$$

The free spectral range (FSR) of the 3 mm loop is FSR $\approx \lambda^2/(\mathrm{n_{eff}L_0}) = 740$ pm near the 1.55 μm pump wavelength. A larger resonant enhancement would be expected if the loop resonator were nearer to critical coupling, which occurs when $K_c = \kappa_c L_c = \pi(2m+1)/2$ for integer $m \geq 1$ [21] with the lowest value ($m = 1$) of $\kappa_c = 9.4 \times 10^4$ m^{-1}. The power within a critically coupled loop resonator may be several orders of magnitude larger than the original input power, and hence the avoidance of dust and other surface contaminants becomes especially important in order to prevent hotspots. Experimentally, the loop will often be slightly undercoupled or overcoupled due to fabrication limitations in controlling the spacing between the microfibres and for these reasons we will study the dependency of ζ on proximity to critical coupling for cases where $\Delta K = (\kappa_c - \kappa_\omega)L_c \approx 1$, rather than zero.

Powers in excess of 100 W will be studied, which can be straightforwardly achieved in experiments using pulsed sources. It is worth noting from previous reports that such high powers can induce thermal phase shifts arising from the temperature dependent refractive index and thermal expansion, which introduce their own nonlinearities and hysteresis into the power transfer function of a microfibre resonator [69]. However, provided that the repetition rate of the source is greater than the inverse of the thermal response time (typically of the order of 0.1–1 ms, depending on the OM diameter and surrounding environment) we may assume here that the resonator exists in a dynamic thermal equilibrium in which the loop geometry and linear/nonlinear index are steady state.

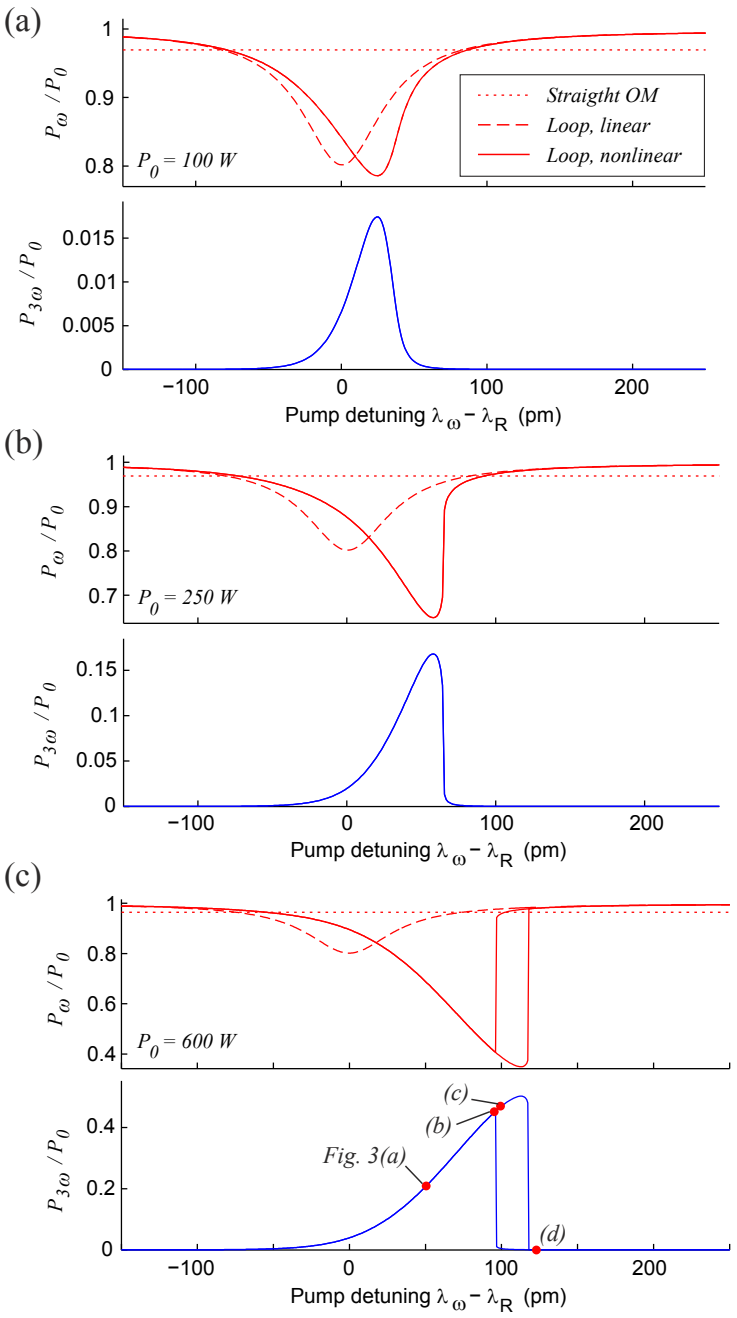

FIGURE 4.2: The pump P_ω and third harmonic $P_{3\omega}$ output power from a loop resonator when input pump power P_0 is (a) 100 W, (b) 250 W and (c) 600 W. The labelled dots indicate the position of the detunings for the transfer characteristics shown in Fig. 4.3. Parameters: $L_0 = 3$ mm $L_c = 50$ μm, $\alpha_{\omega,3\omega} = 5$ m^{-1}, $\kappa = 8\times10^4$ m^{-1}, $\delta\beta \approx 1440$ m^{-1}.

4.2.2 Discussion

Firstly, the transmitted pump P_ω and harmonic $P_{3\omega}$ output powers will be studied for different input powers as shown in Fig. 4.2, where the pump is detuned from a resonance at $\lambda_R \approx 1550$ nm (to avoid confusion with the phase matching detuning $\delta\beta$, this detuning will be denoted as $\delta\lambda$). The coupling between pump modes is chosen to be $\kappa_\omega = 8 \times 10^4$ m^{-1}, which is achievable with close contact between the two microfibres, and corresponds to $\Delta K = 0.71$ (for reference, values of $\Delta K = 0$ and $\Delta K = 3\pi/2$ would correspond to the critically-coupled and totally-uncoupled extremes respectively). Since the higher order harmonic mode's transverse profile contains more oscillations/zeroes, $\kappa_{3\omega}$ is roughly an order of magnitude smaller than κ_ω. Furthermore, in the most general case the resulting third harmonic signal will not necessarily coincide with a resonance and so $\kappa_{3\omega}$ will be set to zero here (situations in which $\kappa_{3\omega} > 0$ will be considered later).

We choose $\delta\beta \approx -1440$ m^{-1}, which is close to the optimum detuning for THG in the loop resonator. The value is negatively offset from zero to compensate for the nonlinear phase shifts, although a smaller but nonetheless significant third harmonic signal would still be detectable if $\delta\beta = 0$ m^{-1}. It should be noted that the magnitude of the optimum detuning for THG in a loop resonator, which experiences stronger SPM/XPM on resonance, is generally larger than that of the straight microfibre (for the OM, the ideal detuning and input parameters can be deduced by finding soliton solutions to the third harmonic interaction which offer the greatest conversion [70]).

For an input power of $P_0 = 100$ W, Fig. 4.2(a) confirms that the pump's nonlinear resonance spectrum appears asymmetrically skewed towards longer wavelengths by $\delta\lambda = 25$ pm due to the accumulated phase shift from SPM. The extinction ratio also exceeds that of the linear resonance due to exchange of power into the harmonic mode – indeed, a peak conversion of $\eta = P_{3\omega}/P_\omega = 0.0174$ is attained. For comparison, the theoretical conversion for an equivalent 3 mm long microfibre (calculated by setting $\kappa_{\omega,3\omega}$ to zero) would be $\eta_0 = 2.7 \times 10^{-5}$. The loop therefore provides a resonant enhancement of $\zeta = \eta/\eta_0 = 640$ times greater than the straight microfibre. This enhancement arises primarily due to a large field enhancement inside the loop of $P_{\text{circ}} = |A_0^\omega(0)|^2 = 8.6P_0$, corresponding to an internal power level of 860 W which should be well tolerated by the OM (if pumping with nanosecond pulses and ≈1 W average powers) and hence possible to demonstrate experimentally using current fabrication techniques. However, far from resonance (e.g. at $\delta\lambda = 200$ pm) η will fall below η_0 since a fraction of the light will bypass the loop in the coupling region, and thus experience an effective path length shorter than L_0.

Increasing P_0 to 250 W will further red-shift the resonance wavelength as shown in Fig. 4.2(b). In addition, the greater pump power increases both η and η_0 to 0.17 and 2.24×10^{-4} respectively, yielding a resonant enhancement of $\zeta = 750$, *i.e.* 17 % times larger than for $P_0 = 100$ W. Although ζ is to a large extent dictated by the intrinsic

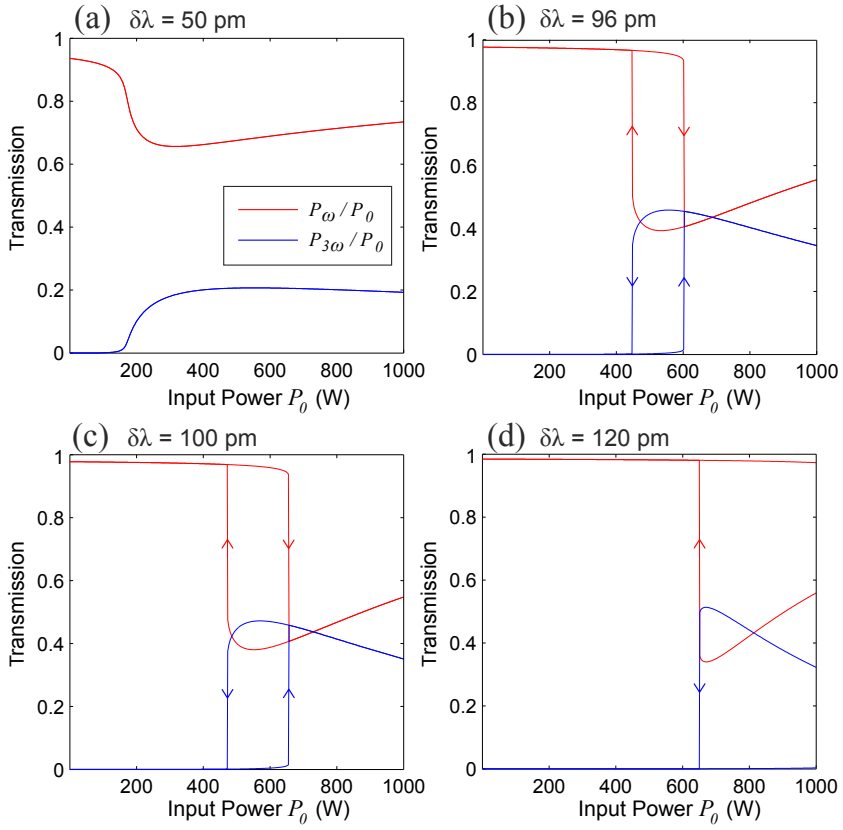

FIGURE 4.3: Transfer characteristics when the pump is detuned from resonance by (a) 50 pm (b) 96 pm (c) 100 pm (d) 120 pm. Other parameters are same as Fig. 4.2.

resonance characteristics (namely the proximity to critical coupling, as will be discussed later), the growth of the third harmonic signal remains nonetheless highly sensitive to any changes to the phase matching conditions. In this case, the detuning of -1440 m^{-1} is slightly lower than the optimum detuning, so at the higher power levels experienced inside the loop, the greater nonlinear phase modulation serves to compensate for this offset and thus increase the conversion and ζ. However, the same mechanism would also reduce the efficiency if $\delta\beta$ was positively offset; physically this depends on whether the OM diameter is slightly larger or smaller than the critical phase matching diameter.

When $P_0 = 600$ W in Fig. 4.2(c), the peak efficiency of $\eta = 0.50$ is sufficiently high such that the maximum enhancement becomes limited by pump depletion, with the pump extinction ratio being 2.3 times greater than the linear case. For this reason, the enhancement of $\zeta = 240$ is smaller than that predicted for the lower input powers. Furthermore, the output spectra from the resonator becomes multi-valued for a band of red-detunings near $\delta\lambda \approx 100$ pm due to bistability. To explain this behaviour, Figs. 4.3(a-d) provide the power transfer characteristics at several positive detunings for a loop resonator of the same parameters. When $\delta\lambda = 50$ pm, the pump wavelength resides within the original linear resonance and so the output is monostable. Increasing $\delta\lambda$ further however introduces hysteresis as expected, and at $\delta\lambda = 96$ pm the upper nonlinear switching power coincides with the input power of $P_0 = 600$ W. For $\delta\lambda = 100$ pm the same input

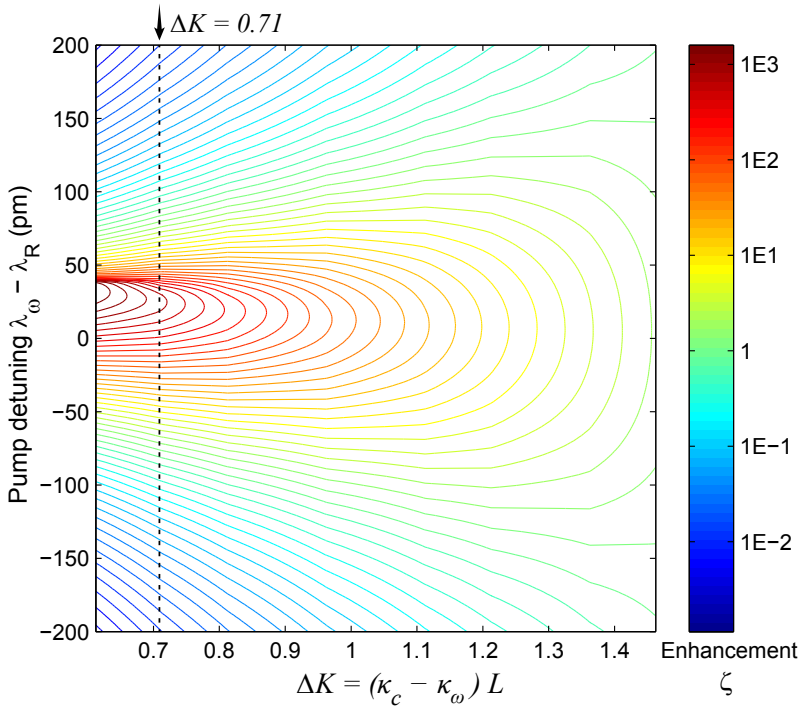

FIGURE 4.4: Enhancement ζ against detuning $\delta\lambda_\omega$, for different proximities to critical coupling ΔK (equivalent to 6.5×10^4 m^{-1} $< \kappa_\omega <$ 8.2×10^4 m^{-1}. Regions where $\zeta > 1$ will generate a greater third harmonic conversion than an equivalent straight microfibre. The dotted line at $\Delta K = 0.71$ corresponds to the situation in Fig. 4.2(a), when $\kappa_\omega = 8 \times 10^4$ m^{-1}. $P_0 = 100$ W and other parameters are same as Fig. 4.2.

power resides on the bistable region, with the upper and lower branches corresponding to the two values in Fig. 4.2(c). Note that only the upper branch for $P_{3\omega}/P_0$ generates any significant harmonic power, since the pump light in the other branch is in an off-resonance high transmission state. Finally, when the detuning is increased to 120 pm, the output for a $P_0 = 600$ W pump becomes single valued again since both the upper and lower switching powers exceed 600 W.

As mentioned earlier, the maximum possible enhancement is greater if the loop resonator is closer to critical coupling, as can be seen in Fig. 4.4 which shows the expected ζ for different ΔK. For comparison purposes, the situation presented earlier in Fig. 4.2(a), when $\kappa_\omega = 8 \times 10^4$ m^{-1}, is highlighted by the dotted line at $\Delta K = 0.71$. In addition, Fig 4.5 shows the corresponding circulating power ratio on resonance P_{circ}/P_0 for the same range of ΔK.

Near to critical coupling, with $\Delta K = 0.6$, P_{circ} exceeds the input power by 9 times which results in large enhancements $> 10^3$, but only over a narrow range of 20 pm near the resonance. Furthermore, ζ only exceeds unity across a 150 pm span - outside of this range, the harmonic signal can become two orders of magnitude weaker than that of the original OM. As ΔK increases, the Q factor of the resonance and hence the enhancement both decrease dramatically, with $\zeta = 2$ at $\Delta K = 1.4$ since the recirculating power is only $1.3P_0$. On the other hand, the conversion bandwidth increases with the resonance

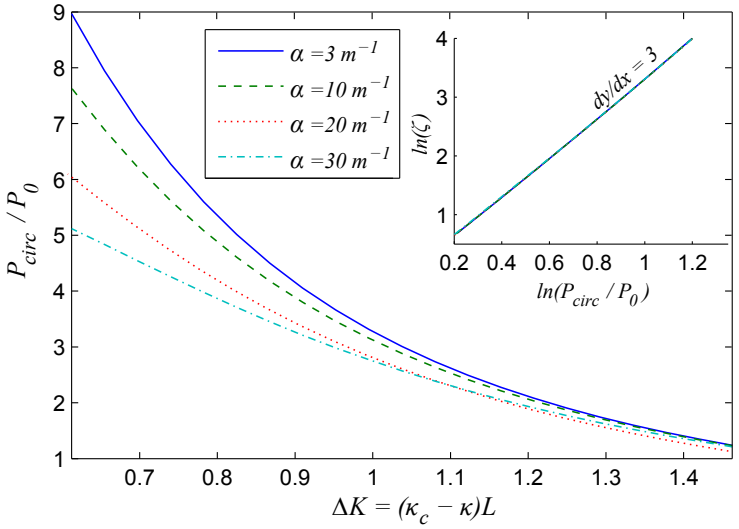

FIGURE 4.5: The maximum internal pump power on resonance inside the loop, P_{circ}/P_0, for different proximities to critical coupling ΔK and loss. $P_0 = 100$ W and other parameters are same as Fig. 4.2. The inset confirms the cubic pump dependency of the enhancement over the range of values simulated.

linewidth. Note that the efficiency also peaks closer to $\delta\lambda = 0$ pm and the $P_{3\omega}$ spectrum is more symmetric, mirroring the loop's linear resonance spectra, since the smaller field in the loop reduces the nonlinear phase shift.

A higher pump loss α_ω will reduce the circulating power ratio and ζ as expected, but the reduction becomes more significant with lower values of ΔK since the light traverses a longer effective path length within the loop on resonance. Although the bend losses of loop resonators with a few millimetres diameter are negligible for sub-micron OM diameters, the microfibre surface may become contaminated by dust or moisture from the atmosphere which increases the surface scattering and absorption losses to reduce P_{circ}. Nonetheless, from Fig. 4.5 it can be seen that even for very large losses of $\alpha_\omega = 30$ the recirculating power ratio still exceeds 5 which provides a corresponding enhancement of $\zeta = 125$.

For the range of ΔK and loss discussed above, the highest efficiency is 5 % (when $\Delta K = 0.6$ and $\alpha = 3$ m^{-1}) and so the pump can be approximated to be undepleted such that the pump distribution inside the loop is similar to what would be observed in the absence of THG. Indeed, the inset in Fig. 4.5 confirms that the enhancement increases cubically with P_{circ}. The enhancement can therefore be estimated from the linear properties accounting for the loss, which are discussed in reference [21]. On resonance, when $m = 1$ (where m is the integer eigenvalue index for the critical coupling condition as mentioned previously), the power transmission simplifies to:

$$|T|^2 = \frac{|A_2^\omega(L_c)|^2}{P_0} = \frac{e^{-\alpha_\omega L_0} + \sin(\kappa_\omega L_c)}{1 + \sin(\kappa_\omega L_c) e^{-\alpha_\omega L_0}} \tag{4.6}$$

and the power recirculation is given by:

$$\frac{P_{\text{circ}}}{P_0} = \frac{1 - |T|^2}{1 - \exp(-2\alpha_\omega L_0)} \tag{4.7}$$

From Eqns. 4.6 and 4.7 the maximum enhancement can be estimated as:

$$\zeta \approx \left[\frac{1 - \sin^2(\kappa_\omega L_c)}{(1 + \sin(\kappa_\omega L_c) e^{-\alpha_\omega L_0})^2} \right]^3 \tag{4.8}$$

Interestingly, Eqn. 4.7 also predicts that P_{circ}/P_0 would counter-intuitively increase with increasing loss if $\pi/2 < \Delta K < 3\pi/2$ (where ΔK was previously defined as the difference from the critical coupling value at $\kappa_c L_c = 3\pi/2$). This can indeed be seen from Fig. 4.5, where the highest loss ($\alpha = 30$ m^{-1}) does not correspond to the lowest circulating power for values of ΔK near 1.5 (the behaviour shown in the numerically calculated graph differs somewhat from the aforementioned analytical prediction based on Eqn. 4.7, due to the phase modulation effects). This phenomenon is however unlikely to be of practical use since it occurs far from critical coupling, where the enhancement is poor, and the larger loss values would detriment the out-coupling of the third harmonic signal.

In general, the bandwidth B of the enhancement is dictated by the resonance linewidth, with a greater resonant enhancement from a higher Q resonance ($|\Delta K|$ closer to 0) achieved at the expense of bandwidth as shown in Fig. 4.6. For weak coupling at $\Delta K = 1.4$, the full width half maximum (FWHM) bandwidth of ζ (measured from a

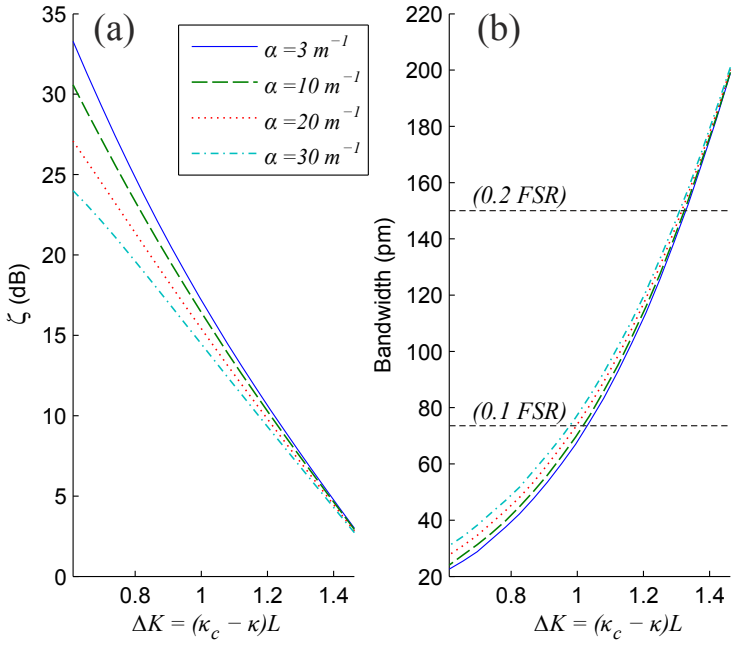

FIGURE 4.6: (a) Resonant enhancement factor ζ of the third harmonic power and (b) bandwidth of the enhancement (taken as the full-width measured halfway between $\zeta = 1$ and maximum ζ) for different proximities to critical coupling ΔK. $P_0 = 100$ W and other parameters are same as Fig. 4.2.

baseline of $\zeta = 1$) is 185 pm, or roughly 25 % of the resonator's FSR. On the other hand, nearer to critical coupling at $\Delta K = 0.8$, the Q factor is approximately 2.8 times greater and limits B to only 40 pm, which may however be useful for applications requiring a narrow linewidth at the harmonic wavelength.

A relatively wide bandwidth is advantageous for converting a wider range of the pump light's nonlinear broadened wavelength components, which may have been generated even before reaching the taper waist region by self phase modulation (additional broadening mechanisms may become significant depending on the pulse duration, power, and the pump wavelength's position on the OM dispersion curve, and indeed their influence has been discussed in the context of continuum generation - see for example references [9, 10]). The broadened pump components will each experience a different enhancement depending on their proximity to the resonance as explained from Fig. 4.2, and it should thus be noted that in the limit when $B \ll FSR \ll$ pump-linewidth, the overall conversion would fall and tend towards the off-resonance level.

Finally, it is interesting to consider cases with $\kappa_{3\omega} > 0$ in which the harmonic is also near resonance, since previous studies on resonantly enhanced harmonic generation in ring resonators [65, 67] suggest that co-resonance of the pump and harmonic can further increase the conversion. However, in order for any efficiency enhancement to be observed at the resonator output, the gain in harmonic power circulating within the loop would need to be large enough to compensate for the reduction in coupling out the harmonic power due its resonance. For values of $\kappa_{3\omega}$ up to 2×10^4 m^{-1}, Fig. 4.7 shows the expected harmonic conversion spectrum for a loop with the same parameters as Fig. 4.2(a) and $P_0 = 100$ W input. Both κ_ω and $\kappa_{3\omega}$ can be altered in practice by adjusting the OM index, surrounding index, OM separation and pump wavelength. Altering one of these

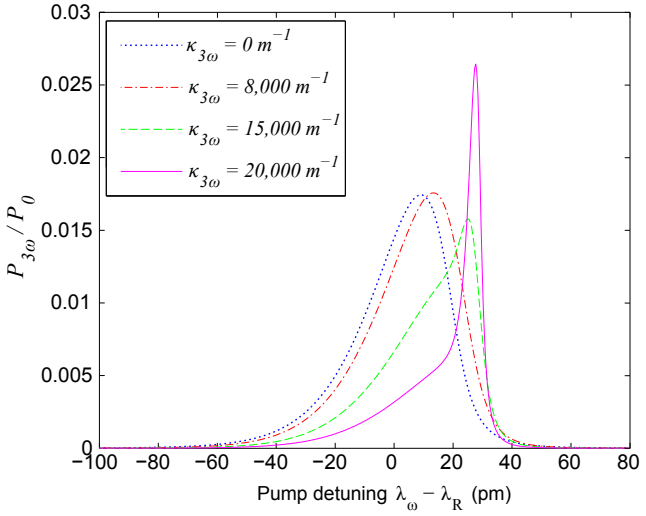

FIGURE 4.7: The third harmonic conversion against detuning, when the harmonic light is partially recirculated (i.e. with $\kappa_{3\omega} > 0$ m^{-1}). $P_0 = 100$ W and other parameters are same as Fig. 4.2.

parameters will inevitably affect both couplings, but by changing two or more parameters simultaneously it is possible to keep constant one of the couplings and change the other (or alternatively, tailor their ratio). As $\kappa_{3\omega}$ increases from zero, the conversion generally falls because the third harmonic signal is being recirculated rather than coupled out. However, for detunings in the range +20 pm to +30 pm, the efficiency can be enhanced significantly (by up to 50 % greater when $\kappa_{3\omega} = 2 \times 10^4$ m^{-1}).

The behaviour can be understood from Eqn. 4.2b, which states that at the start of loop $|A_0^{3\omega}|$ will grow if $0 < \theta_{3\omega}(s=0) - 3\theta_{\omega}(s=0) < \pi$ (neglecting phase modulation) where θ_i represents the phase of A_0^i. For this particular example, the condition is satisfied not at zero detuning, but rather at the detunings around $\delta\lambda \approx +30$ pm where the power of the recirculated harmonic 'seed' will grow with distance as it propagates around the loop. Note that although this phase condition is also met at $\delta\lambda = 40$ pm, the pump is off resonance and hence η is low. For this reason, the co-resonant enhancement is only apparent over a relatively narrow 10 pm range.

4.2.3 Summary

The use of microfibre loop resonators can greatly enhance third harmonic generation efficiency by several orders of magnitude greater than that of the straight microfibre, thus allowing conversion rates of several percent even at pump powers as low as 100 W. Importantly, this requires microfibre loop lengths of only a few mm which is sufficiently short to be fabricated to a high diameter uniformity; the distance being comparable to the microheater hot zone size. A range of interesting characteristics arise from the interplay of the nonlinear properties of the fibre and the resonant behaviour. For example, at higher powers, the resonator hysteresis causes nonlinear switching of both the pump and third harmonic power levels. Furthermore, allowing co-resonance of both the harmonic and pump light can increase the conversion further.

4.3 Experiment

4.3.1 Experimental details

In order to observe resonantly-enhanced third harmonic generation, silica microfibre loop resonators were fabricated by Rand Ismaeel (ORC, University of Southampton). These samples were produced from silica tapers with a 770 nm diameter waist (to ensure phase matching to the $HE_{12}(3\omega)$ harmonic mode) and a 1 mm waist length, and were characterised using the same experimental setup shown in Fig. 3.9 on page 32 with $\lambda_1 = 1.55$ μm 4 ns pump pulses. In order to limit nonlinear pump broadening, a lower pump power of $P_0 = 100$ W was used during the nonlinear measurements on

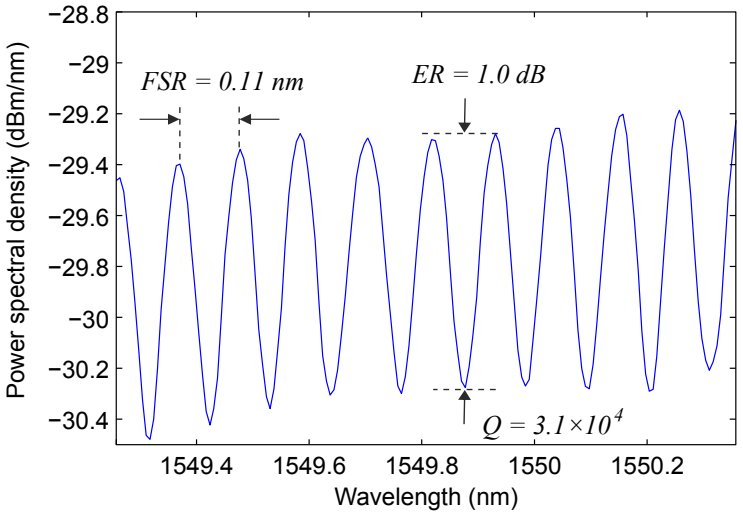

FIGURE 4.8: The output spectrum for the 6 mm diameter loop resonator, recorded with an ASE source at the resonator input. The wavelength resolution of the spectrum analyser is 20 pm. (Loop resonator fabricated and spectra recorded by R. Ismaeel).

both the taper and loop, such that the 100 pm pump linewidth remains comparable to the resonance FWHM, and the repetition rate was increased to 250 kHz to provide a moderately high average power to aid detection.

The loop resonator was produced by fixing the fibre ends of the taper onto linear stages, which were subsequently pushed together so the OM is slightly bent. Next, a rotation stage was used to twist one end of the fibre, providing a torsion which forced the taper into a 1 cm diameter loop, before both fibre pigtails were simultaneously pulled apart until the desired loop diameter and tightness were achieved.

With this procedure, Q factors in the range $10^4 > Q > 10^5$ and extinction ratios of several dB can be achieved consistently. The linear spectrum for a typical loop in Fig. 4.8, recorded using the ASE from an amplifier as a source, shows a FWHM linewidth of 50 pm, i. e. $Q \approx \lambda/\mathrm{FWHM} = 3.1 \times 10^4$ (the true Q may be higher, since the measured linewidth is comparable to the OSA resolution of 20 pm).

4.3.2 Discussion

Before analysing the experimental results, we shall first determine the expected enhancement by applying the parameters of the experimentally fabricated loops to the theory from the previous section. Although the loop diameter is 6 mm, the length of the waist over which phase matching occurs is only 1 mm. The simulations from section 4.2 are therefore modified so that THG only occurs over a 1 mm section within the loop, whereas SPM and XPM are assumed throughout the entire length of the loop.

In addition, losses of $\alpha_{\omega,3\omega} = 5\ \mathrm{m}^{-1}$ are included to account for scattering losses and surface contamination incurred during the manipulation of the taper, and the coupling

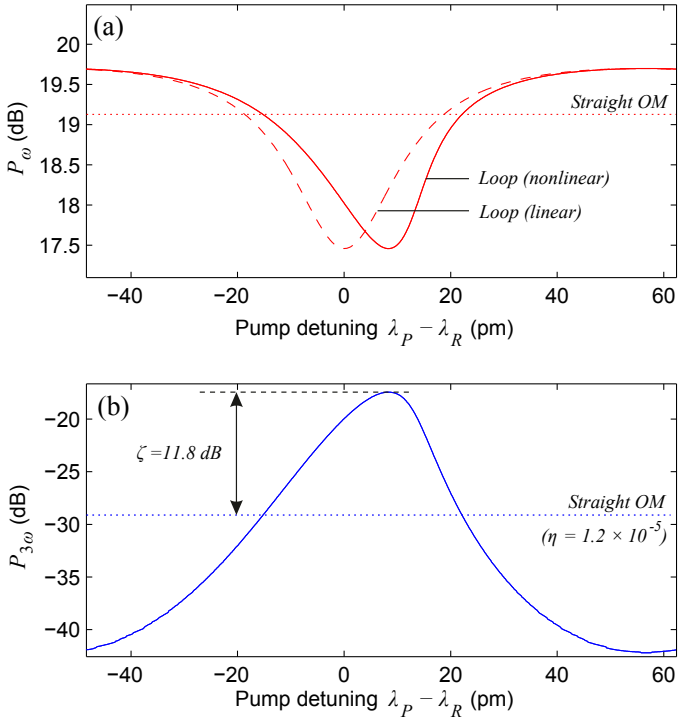

FIGURE 4.9: (a) Simulated output pump power and (b) third harmonic power from a silica loop resonator against pump detuning (solid lines). The dashed line shows the linear spectra of the loop, and dotted lines represent the straight microfibre. Parameters were chosen to match the experimental loop: $P_0 = 100$ W (20 dB), microfibre length $L_0 = 20$ mm, $L_{\text{THG}} = 1$ mm, $L_c = 50$ μm, $\kappa_\omega = 7.3 \times 10^4$ m^{-1}, $\kappa_{3\omega} = 0$ m^{-1}, $\alpha_\omega = \alpha_{3\omega} = 5$ m^{-1}, n_{eff} =1.081, $\delta\beta = \beta_{3\omega} - 3\beta_\omega \approx -1440$ m^{-1}.

length and coefficient are $L_c = 50$ μm and $\kappa_\omega = 7.3 \times 10^4$ m^{-1} respectively. These values were chosen to ensure the linear resonance spectrum matches that which was experimentally recorded.

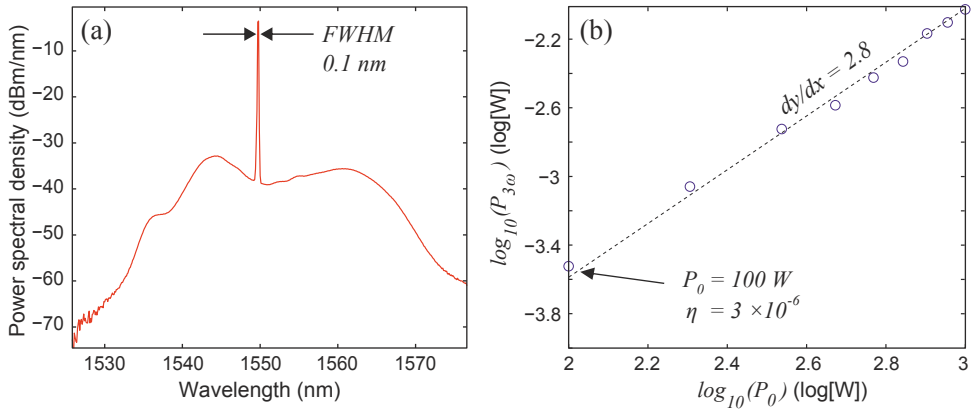

FIGURE 4.10: (a) The pump spectrum with central wavelength of 1550 nm (recorded via a -20 dB coupler). (b) Logarithmic plot of third harmonic against pump peak powers in the range P_0 =0.1-1 kW. The dotted line provides a linear fit with a gradient of 2.8.

Figure 4.9 shows the simulated output pump P_ω and third harmonic power $P_{3\omega}$ at different pump detunings $\delta\lambda_\omega$ from the resonant wavelength over one free spectral range. The third harmonic conversion efficiency is maximal when the pump light is on resonance, with an enhancement of $\zeta \approx 12$ dB greater than that which would be expected from the straight microfibre ($\eta_0 = P_{3\omega}/P_0 = 1.2 \times 10^{-5}$).

Having estimated the expected enhancement, we now discuss the experimental results. At $P_0 = 100$ W, the straight microfibre conversion is $\eta_0 = 3.0 \times 10^{-6}$; similar to the level reported in [16] and roughly 5 times lower than the simulated value (primarily due to an offset between the actual and ideal phase matching diameter). To verify the signal arises from a $\chi^{(3)}$ interaction, the logarithmic harmonic-pump power graph in Fig. 4.10(b) confirms a linear gradient of 2.8; close to the expected gradient of 3 but somewhat lower due to the efficiency reduction when the pump broadens at higher powers near 1 kW.

Figure 4.11 compares the third harmonic spectrum of the straight OM and the loop, whilst the latter is being tightened (the loop diameter is kept at 6 mm throughout). With an initially loose loop, the enhancement is only $\zeta \approx 1$ dB since the coupling is too low. Tightening the loop by further twisting one pigtail forces the microfibre segments in the coupling region closer together which increases κ_ω towards critical coupling, as well as increasing L_c, resulting in stronger resonances. The efficiency subsequently increases to six times greater than that of the taper, with $\eta = 1.8 \times 10^{-5}$ ($\zeta = 7.7$ dB enhancement).

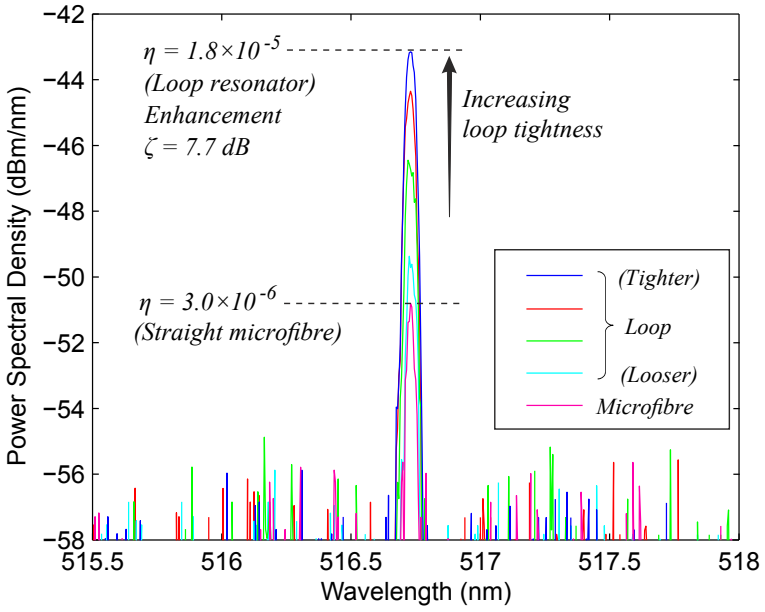

FIGURE 4.11: A comparison of the third harmonic signal spectrum before and after configuring the straight microfibre into the loop resonator. For the loop, several spectra are given, corresponding to different loop tightness during fabrication whilst keeping diameter at 6 mm (measured via a short pass filter with 5 dB loss at $\lambda \approx 0.5$ μm).

This experimentally observed enhancement is similar but slightly lower than the theoretical value, perhaps due to additional scattering loss from the coupling region. The value of $\alpha_{3\omega}$ for the harmonic mode may also be larger than α_{ω} for the pump, although this value could not be experimentally estimated without a calibrated source at the harmonic mode. Also, the 3 dB THG linewidth of 50 pm is slightly larger than the original 45 pm linewidth recorded from the straight OM, due to the higher circulating power in the loop broadening the pump further. Note that a larger ΔK with a weaker resonance would increase the enhancement bandwidth, albeit at the cost of a reduced peak ζ value.

4.3.3 Summary

We fabricated tapers with waist diameters near 0.76 μm and an estimated waist length of 1 mm to ensure intermodal phase matching for THG. When pumped with $\lambda = 1.55$ μm 4 ns pulses at 100 W peak power, the conversion was $\eta = 3 \times 10^{-6}$. The loop resonator was then formed by manually translating and twisting the microfibre ends, to produce loop diameters down to 6 mm and resonant efficiency enhancements up to ζ =7.7 dB for the same pump parameters.

4.4 Conclusions

By simply configuring the taper into a loop resonator, it is possible to enhance the third harmonic efficiency by orders of magnitude. We have experimentally observed efficiencies in loop resonators $\zeta = 7.7$ dB greater than that of the original straight microfibre when pumping at 100 W peak power, and by optimising the coupling geometry, enhancements up to 20 dB can be realistically expected using currently available manufacturing technology. As in many optical systems however, there exists a compromise between the gain and bandwidth – in this case, a stronger resonance nearer to critical coupling offers greater enhancement at the expense of reduced bandwidth.

Although the work described in this chapter relates to loop resonators, one would expect similar behaviour in other microfibre resonators such as the knot [22] or the microcoil [23], which offer improved stability whilst maintaining the advantage of straightforward fabrication.

Chapter 5

Second Harmonic Generation

5.1 Overview

The process of second harmonic generation requires a non-zero second order nonlinear susceptibility $\chi^{(2)}$, in order to induce a corresponding second order polarisation term:

$$\widetilde{\mathbf{P}}^{(2)}(\mathbf{r},t) = \chi^{(2)} \vdots \widetilde{\mathbf{E}}(\mathbf{r},t)\widetilde{\mathbf{E}}(\mathbf{r},t) \tag{5.1}$$

In particular, this term is responsible for mixing the pump beam, with an $\widetilde{\mathbf{E}} \sim \exp(i\omega_1 t)$ time dependency, to produce the frequency doubled signal at $2\omega_1$. It is often assumed that silica waveguides alone cannot be used for second harmonic generation (SHG), since the isotropic structure of the glass would appear to deny any $\chi^{(2)}$. However, whilst it is true that there is no bulk dipole contribution to the second order susceptibility $\chi^{(2)}$, there exist however two other small but significant $\chi^{(2)}$ sources – (i) the bulk quadrupole and magnetic dipole effects [24, 25], and (ii) the surface dipole at the glass-air interface [71, 72, 73, 74]. The surface $\chi^{(2)}$ effect is especially interesting in microfibres and becomes influential since the surface field strength is relatively large, in addition to the relatively high surface-area to volume ratio.

In this chapter, we shall provide a short background of SHG in microfibres, before discussing the theory in detail and simulations to predict the potential second harmonic efficiencies which might be achieved. In addition, we present our experimental work towards achieving SHG in microfibres, as well as loop resonators to improve efficiency. The experiments were carried out in collaboration with R. Ismaeel (ORC, University of Southampton) and M. A. Gouveia (UNICAMP, Brazil).

5.2 Background

Surface SHG from the interface between isotropic media was first studied by Bloembergen and Pershan in 1962 [75], and by the late 1960s, had been experimentally observed at the boundary of liquids and glasses [71, 76]. Furthermore, the phenomena has since been employed as tool for surface characterisation since the harmonic signal depends upon the interface material and quality [77]. In such instances, the absence of phase matching over any appreciable distance limits the conversion.

Using microfibres, however, allows intermodal phase matching between the second harmonic and the pump so that a larger conversion can be attained. SHG was indeed observed and noted in microfibres [14, 16, 57], although there were no attempts to further investigate or optimise the SH signal since these experiments focused on THG, and to date there remains little experimental literature on SHG in microfibres. Recently however, Lægsgaard modelled SHG in circular microfibres and 'wagonwheel' holey silica fibres by solving the SHG differential equations in the undepleted pump approximation [13]. In both cases, the second order polarisation consists mainly of surface dipole contributions, and was modelled using the surface $\chi^{(2)}$ components characterised by Rodriguez et al. [26].

Simulations on SHG in microfibres were also undertaken by Richard [12]. As before, the second harmonic is generated through intermodal phase matching, but unlike Lægsgaard's work, the core is assumed to possess a bulk $\chi^{(2)}$ (for example, an effective $\chi^{(2)}$ can be induced from homogenous electric poling of a silica microfibre [78]). Furthermore, the phase mismatch is taken to vary along the fibre with gradient κ' in order to model a realistic taper profile. For $\kappa' \approx 0$ the conversion can reach close to 100% as expected intuitively, but interestingly the efficiency remains high even for larger values of κ' which suggests that a slight tapering of the profile in the waist can introduce a detuning gradient to compensate the changes in nonlinear phase (due to pump-harmonic power exchanges), to maintain a near-optimum effective detuning.

5.3 Theory and simulations

5.3.1 Second harmonic generation phase matching

The same intermodal technique used to phase match the third harmonic, explained in section 3.3, can be applied to second harmonic generation, i. e. by choosing an appropriate microfibre diameter at which the fundamental $\mathrm{HE}_{11}(\omega)$ pump mode and a higher order second harmonic mode propagate with the same effective index.

Figure 5.1 shows that for a $\lambda_1 = 1.55$ μm pump, there are two key phase match points, with the $\mathrm{TM}_{01}(2\omega)$ and $\mathrm{HE}_{21}(2\omega)$ modes at critical diameters of 690 nm and 780 nm

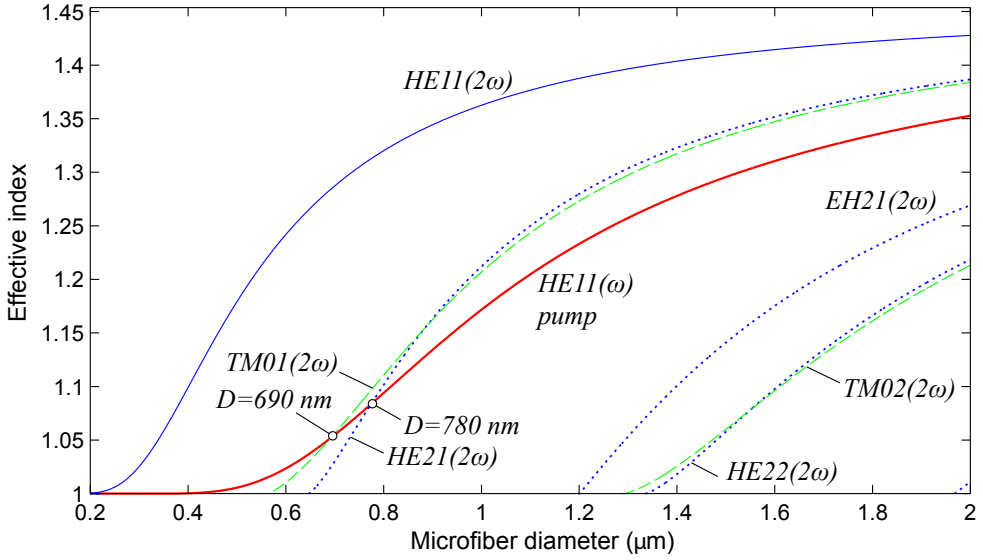

FIGURE 5.1: Effective index n_{eff} curves for the $\lambda_1 = 1.55$ μm fundamental pump mode and various second harmonic modes in a silica microfibre. Two phase match points are highlighted.

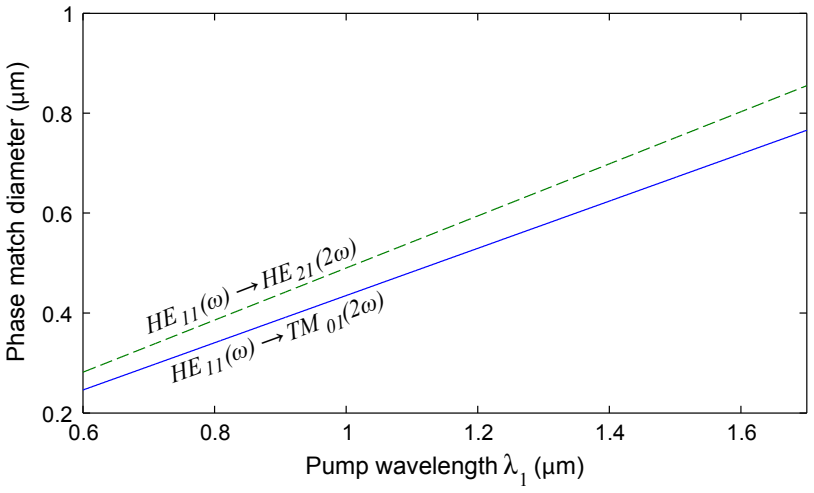

FIGURE 5.2: The critical microfibre diameter needed to phase match the $\text{TM}_{01}(2\omega)$ (solid) and $\text{HE}_{21}(2\omega)$ (dashed) second harmonic modes to the fundamental pump mode.

respectively. Over the range of pump wavelengths between 0.6 μm to 1.7 μm, these phase matching diameters scale roughly linearly with λ_1 as shown in Fig. 5.2 and would be around $D = 0.5$ μm for a 1 μm pump, which remains well within the range that can be fabricated with most tapering rigs (for shorter pump wavelengths however, the required diameter would be challenging to realise).

Note that the set of higher order modes considered for SHG differs from that of THG, since the form of their overlap integral between the pump and harmonic mode differs considerably. Namely, neither the TM_{01} and HE_{21} modes can be generated for THG due to their field symmetry (see Appendix B), but both are possible for SHG.

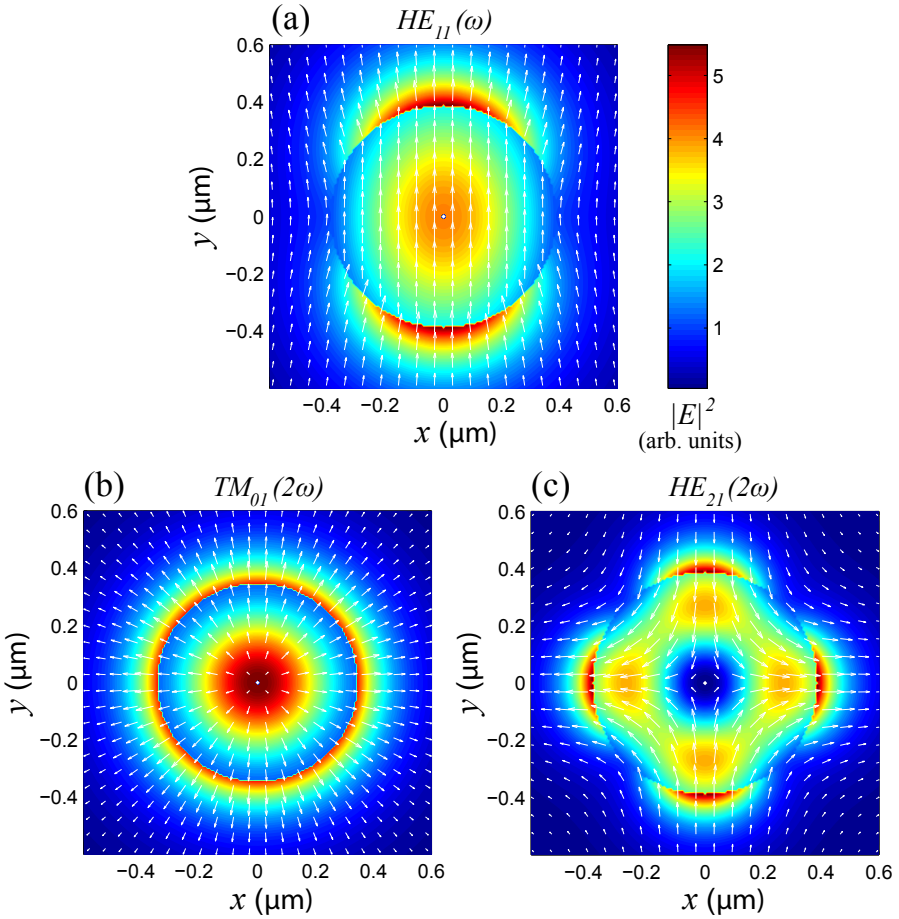

FIGURE 5.3: Contour plots of the electric field intensity and the transverse field vector for the $HE_{11}(\omega)$ $\lambda_1 = 1.55$ μm fundamental pump mode, and (b) the $TM_{01}(2\omega)$ and (c) $HE_{21}(2\omega)$ second harmonic modes at their respective phase matching diameters.

The electric field intensity $|\mathbf{E}|^2$ profile for these modes are shown in Fig. 5.3, along with the transverse field vector plot. The surface field strength is high for each of the modes and even exceeds the bulk field by a factor of 2 in the fundamental pump. Moreover, the field is strongly radial at the surface, which is beneficial for surface SHG since it is aligned with the direction of material anisotropy.

5.3.2 Calculation of second harmonic conversion efficiency

We begin our analysis of the second harmonic conversion by first defining the propagating electric and magnetic fields:

$$\widetilde{\mathbf{E}}_i = A_i \mathbf{E}_i \exp(i(\beta_i \ - \omega_i t)) + \text{c.c.} \tag{5.2a}$$

$$\widetilde{\mathbf{H}}_i = A_i \mathbf{H}_i \exp(i(\beta_i \ - \omega_i t)) + \text{c.c.} \tag{5.2b}$$

where $i = 1$ and 2 for the pump and harmonic fields respectively, and the amplitudes are normalised so that the power is given by the square of the amplitude $|A_i|^2$, i. e. such that:

$$S = \frac{1}{2}\iint_{\infty} (\mathbf{E_i} \times \mathbf{H_i}^*) \cdot \hat{\mathbf{z}}\, dA = 1 \tag{5.3}$$

Assuming the slowly varying envelope approximation, we can derive the nonlinear propagation equations for SHG by adopting the same approach using the Lorentz reciprocity theorem as for THG (Appendix B), but using $\widetilde{\mathbf{P}}_{\mathrm{NL}} = \widetilde{\mathbf{P}}^{(2)}$. The coupled mode differential equations are then expressed as follows:

$$\frac{dA_1}{dz} = -\alpha_1 A_1 + in^{(2)}k_1\Big[(J_1|A_1|^2 + 2J_2|A_2|^2)A_1\Big] + i\rho_2 A_1^* A_2 e^{i\delta\beta z} \tag{5.4a}$$

$$\frac{dA_2}{dz} = -\alpha_2 A_2 + in^{(2)}k_1\Big[(4J_2|A_1|^2 + 2J_5|A_2|^2)A_2\Big] + i\rho_2 A_1^2 e^{-i\delta\beta z} \tag{5.4b}$$

where the overlap integrals J_i are defined previously in Eqn. 3.8 and the detuning is $\delta\beta = \beta_2 - 2\beta_1$. The nonlinear coupling (overlap) coefficient ρ_2 is evaluated between the harmonic mode and the second order nonlinear polarisation $\mathbf{P}^{(2)}$, and can be decomposed into the anisotropic surface dipole (ρ_s) and bulk multipolar (ρ_b) contributions [13]:

$$\rho_2 = \rho_s + \rho_b \tag{5.5a}$$

$$\rho_s = \frac{\omega_2}{2}\int_0^{2\pi} \mathbf{E}_2^* \cdot \mathbf{P}_s^{(2)} a\, d\theta \tag{5.5b}$$

$$\rho_b = \frac{\omega_2}{2}\int_0^{a}\int_0^{2\pi} \mathbf{E}_2^* \cdot \mathbf{P}_b^{(2)} r\, d\theta\, dr \tag{5.5c}$$

where a is the microfibre radius. Physically, the surface nonlinearity arises from the presence of termination bonds at the interface (e.g. between Si and –OH or –H), whereas below the surface, the bonds are predominantly between Si and O only. This structural anisotropy is consequently reflected in the response of the electrons to an external field and hence can be modelled with an effective $\chi^{(2)}$ tensor. The surface second order polarisation $\mathbf{P}_s^{(2)}$ itself therefore contains several terms, corresponding to the various tensor elements of $\chi^{(2)}$ [13]:

$$\mathbf{P}_s^{(2)} = \mathbf{P}_{s1}^{(2)} + \mathbf{P}_{s2}^{(2)} + \mathbf{P}_{s3}^{(2)} \tag{5.6a}$$

$$\mathbf{P}_{s1}^{(2)} = \epsilon_0 \chi_{\perp} E_{1\perp}^2 \hat{\mathbf{r}} \tag{5.6b}$$

$$\mathbf{P}_{s2}^{(2)} = \epsilon_0 \chi_{\perp\parallel} |\mathbf{E}_{1\parallel}|^2 \hat{\mathbf{r}} \tag{5.6c}$$

$$\mathbf{P}_{s3}^{(2)} = 2\epsilon_0 \chi_{\parallel} E_{1\perp} \mathbf{E}_{1\parallel} \tag{5.6d}$$

where $\hat{\mathbf{r}}$ is the unit radial vector perpendicular to the OM surface, and the surface $\chi^{(2)}$ tensor elements $\chi_{\perp}$, $\chi_{\perp\parallel}$ and $\chi_{\parallel}$ are 6300, 770 and 790 pm^2/V respectively [26]. $E_{1\perp}$ and $E_{1\parallel}$ represent the pump electric field components perpendicular and parallel to the surface, respectively. Eqns. 5.6b to 5.6d are substituted into Eqn. 5.5b and then

integrated over the microfibre circumference to determine their relative contribution to the total ρ_2. This can be performed analytically using the mode electric field expressions from Eqns. 2.12 and 2.8, and for the $\mathrm{TM}_{01}(2\omega)$ mode, these surface components take the form:

$$\rho_{s1} = \frac{\pi}{2} c_1^2 c_2 \epsilon_0 \omega_2 \chi_\perp a^4 \frac{\beta_1^2 \beta_2}{U_1^2 U_2} R_{1r}^2(a) J_1(U_2) \tag{5.7a}$$

$$\rho_{s2} = \frac{\pi}{2} c_1^2 c_2 \epsilon_0 \omega_2 \chi_{\perp\parallel} a^2 \frac{\beta_2}{U_2} J_1(U_2) \left[\left(\frac{\beta_1 a}{U_1} \right)^2 R_{1\theta}^2(a) + J_1^2(U_1) \right] \tag{5.7b}$$

$$\rho_{s3} = \pi c_1^2 c_2 \epsilon_0 \omega_2 \chi_\parallel a^2 \frac{\beta_1}{U_1} R_{1r}(a) J_1(U_1) J_0(U_2) \tag{5.7c}$$

and for the $\mathrm{HE}_{21}(2\omega)$ mode, the surface contributions are:

$$\rho_{s1} = \frac{\pi}{4} c_1^2 c_2 \epsilon_0 \omega_2 \chi_\perp a^4 \frac{\beta_1^2 \beta_2}{U_1^2 U_2} R_{1r}^2(a) R_{2r}(a) \tag{5.8a}$$

$$\rho_{s2} = -\frac{\pi}{4} c_1^2 c_2 \epsilon_0 \omega_2 \chi_{\perp\parallel} a^2 \frac{\beta_2}{U_2} R_{2r}(a) \left[\left(\frac{\beta_1}{U_1} a R_{1\theta}(a) \right)^2 - J_1^2(U_1) \right] \tag{5.8b}$$

$$\rho_{s3} = \frac{\pi}{2} c_1^2 c_2 \epsilon_0 \omega_2 \chi_\parallel a^2 \frac{\beta_1}{U_1} R_{1r}(a) \left[\frac{\beta_1 \beta_2}{U_1 U_2} a^2 R_{1\theta}(a) R_{2\theta}(a) + J_1(U_1) J_2(U_2) \right] \tag{5.8c}$$

where the field distribution coefficients are given by:

$$U_i = \frac{2\pi}{\lambda_i} a \sqrt{n_1^2 - n_{\mathrm{eff,i}}^2} \tag{5.9a}$$

$$W_i = \frac{2\pi}{\lambda_i} a \sqrt{n_{\mathrm{eff,i}}^2 - n_2^2} \tag{5.9b}$$

$$R_{\nu r,i} = \frac{1 - s_\nu}{2} J_{\nu-1}\left(\frac{U_i r}{a} \right) - \frac{1 + s_\nu}{2} J_{\nu+1}\left(\frac{U_i r}{a} \right) \tag{5.9c}$$

$$R_{\nu\theta,i} = \frac{1 - s_\nu}{2} J_{\nu-1}\left(\frac{U_i r}{a} \right) + \frac{1 + s_\nu}{2} J_{\nu+1}\left(\frac{U_i r}{a} \right) \tag{5.9d}$$

$$s_{\nu,i} = \frac{\nu\left(U_i^{-2} + W_i^{-2}\right)}{\frac{J'_\nu(U_i)}{U_i J'_\nu(U_i)} + \frac{K'_\nu(W_i)}{W_i K'_\nu(W_i)}} \tag{5.9e}$$

and the power normalisation factor is:

$$c_0 = \frac{2\sqrt{2}}{\iint_{-\infty}^{\infty} (\mathbf{E_1} \times \mathbf{H_1}^*) \cdot \hat{\mathbf{z}}\, dA \sqrt{\iint_{-\infty}^{\infty} (\mathbf{E_2} \times \mathbf{H_2}^*) \cdot \hat{\mathbf{z}}\, dA}} \tag{5.10}$$

On the other hand, the bulk multipolar term $\mathbf{P}_b^{(2)}$ contain two components:

$$\mathbf{P}_b^{(2)} = \mathbf{P}_{b1}^{(2)} + \mathbf{P}_{b2}^{(2)} \tag{5.11a}$$

$$\mathbf{P}_{b1}^{(2)} = \epsilon_0 \gamma \nabla (\mathbf{E}_1 \cdot \mathbf{E}_1) \tag{5.11b}$$

$$\mathbf{P}_{b2}^{(2)} = \epsilon_0 \delta (\mathbf{E}_1 \cdot \nabla) \mathbf{E}_1 \tag{5.11c}$$

where δ and γ are bulk multipolar coefficients with values of -390 and 780 pm^2/V

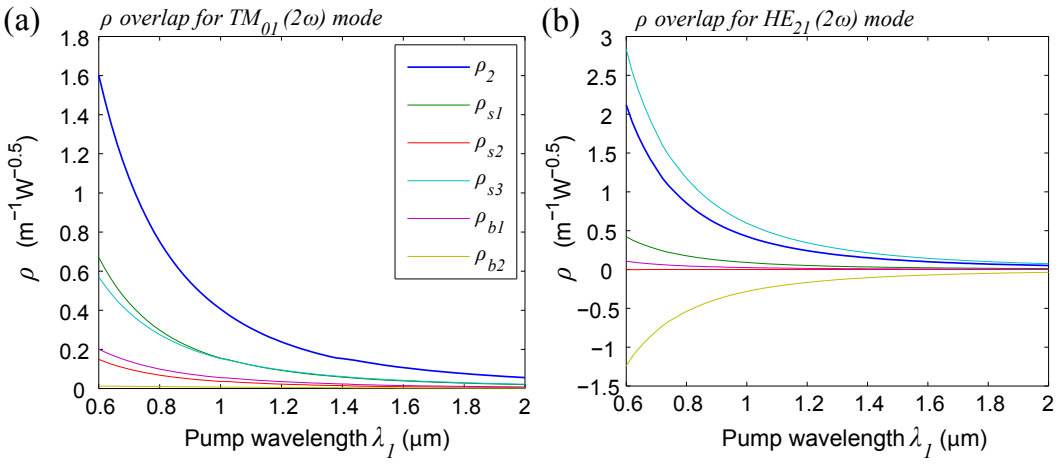

FIGURE 5.4: Second-harmonic/pump overlap integral ρ_2 for (a) $TM_{01}(2\omega)$ and (b) $HE_{21}(2\omega)$ modes. The surface ρ_s and bulk ρ_b contributions are also given.

respectively [26]. The term 'multipolar' is used here to imply that the coefficients' values collectively incorporate both the electric quadrupole and magnetic dipole effects. The second term $\mathbf{P}_{b2}^{(2)}$ can be written more explicitly as:

$$\mathbf{P}_{b2}^{(2)} = \epsilon_0 \delta \begin{pmatrix} E_r \frac{\partial E_r}{\partial r} + \frac{E_\theta}{r} \frac{\partial E_r}{\partial \theta} \\ E_r \frac{\partial E_\theta}{\partial r} + \frac{E_\theta}{r} \frac{\partial E_\theta}{\partial \theta} \\ E_r \frac{\partial E_z}{\partial r} + \frac{E_\theta}{r} \frac{\partial E_z}{\partial \theta} \end{pmatrix} \tag{5.12a}$$

The calculated total overlap ρ_2 and its components are shown in Fig. 5.4 for the $TM_{01}(2\omega)$ and $HE_{21}(2\omega)$ modes, assuming a $HE_{11}(\omega)$ pump. Although the surface contributions ρ_s are the greatest as expected, it is also clear that the bulk components cannot be neglected, especially for the $HE_{21}(2\omega)$ mode where ρ_{b2} is large and negative, which reduces the net overlap. For a $\lambda_1 = 1.55$ μm pump, the overlap for both modes is roughly equal at $\rho_2 = 0.12$ $\mathrm{m^{-1}W^{-1/2}}$ and 0.11 $\mathrm{m^{-1}W^{-1/2}}$ for the $TM_{01}(2\omega)$ and $HE_{21}(2\omega)$ modes respectively, which implies they would offer similar SHG conversion efficiencies.

Next, we integrate Eqns. 5.4a and 5.4b, using the parameters summarised in Table 5.1, to give the theoretical conversion efficiency of both modes as shown in Fig. 5.5. For the $TM_{01}(2\omega)$ and $HE_{21}(2\omega)$ modes, the conversion can reach a significant level of $\eta = 3.4\%$ and 3.0% respectively over 5 cm with a 1 kW 1.55 μm wavelength pump. For the ideal conversion curves, the optimum detuning $\delta\beta_0$ was roughly 200 $\mathrm{m^{-1}}$ in order to offset the nonlinear phase modulation, i. e.:

$$\delta\beta_0 = -2n^{(2)}k_1\left[(2J_2 - J1)P_0\right] \tag{5.13}$$

As with THG, the harmonic power varies strongly with detuning and will fall considerably if $\delta\beta$ is offset by even several hundred $\mathrm{m^{-1}}$ away from $\delta\beta_0$, which thus imposes

Parameter	Symbol	$TM_{01}(2\omega)$	$HE_{21}(2\omega)$
Diameter (nm)	D	695	777
Pump SPM overlap (μm^{-2})	J_1	0.64	1.02
Pump XPM overlap (μm^{-2})	J_2	0.55	0.98
Harmonic-pump overlap ($m^{-1}W^{-0.5}$)	ρ_2	0.12	0.11
Harmonic SPM overlap (μm^{-2})	J_5	1.47	2.40

TABLE 5.1: Summary of the SHG phase matching diameters and modal overlaps, when phase matching the $HE_{11}(\omega)$ mode with the $TM_{01}(2\omega)$ and $HE_{21}(2\omega)$ mode for a $\lambda_1 = 1.55$ μm pump.

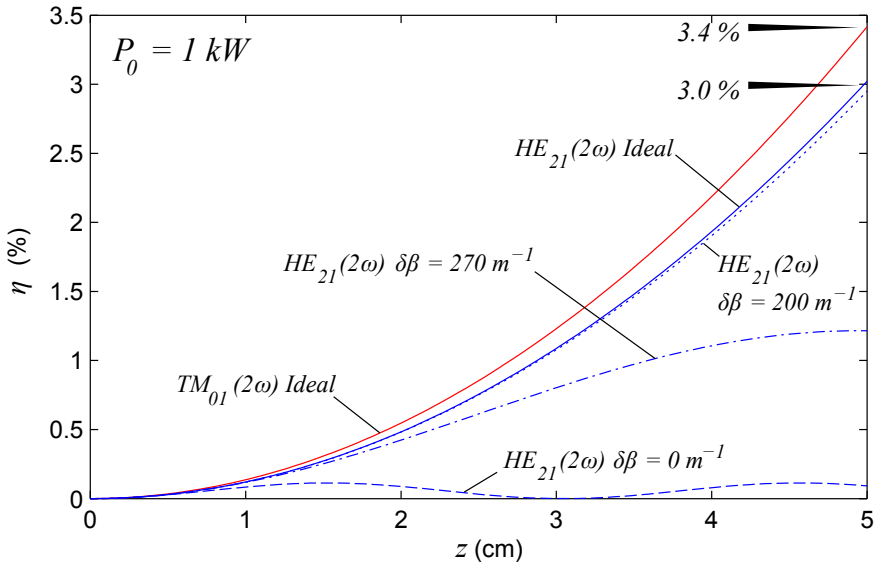

FIGURE 5.5: Simulated conversion efficiency for the $TM_{01}(2\omega)$ and $HE_{21}(2\omega)$ harmonic modes for a 1 kW $\lambda_1 = 1.55$ μm pump. Solid lines indicate ideal conversion (optimised detuning), whilst the dotted and dashed lines represent different variously detuned cases for the $HE_{21}(2\omega)$ mode.

fabrication tolerances of the order of nm. For the distance of several cm, the pump remains undepleted and so η scales quadratically with interaction distance.

5.3.3 Resonantly enhanced second harmonic generation

Compared to THG, theoretical efficiency reached over a few cm is roughly an order of magnitude lower, since the surface and bulk $\chi^{(2)}$ is relatively weak compared to the bulk $\chi^{(3)}$, and the SH power scales only quadratically with pump power rather than cubically. Therefore, to increase the second harmonic power, the use of loop resonators for resonantly enhanced SHG will be discussed theoretically here, as well as experimentally in the following section.

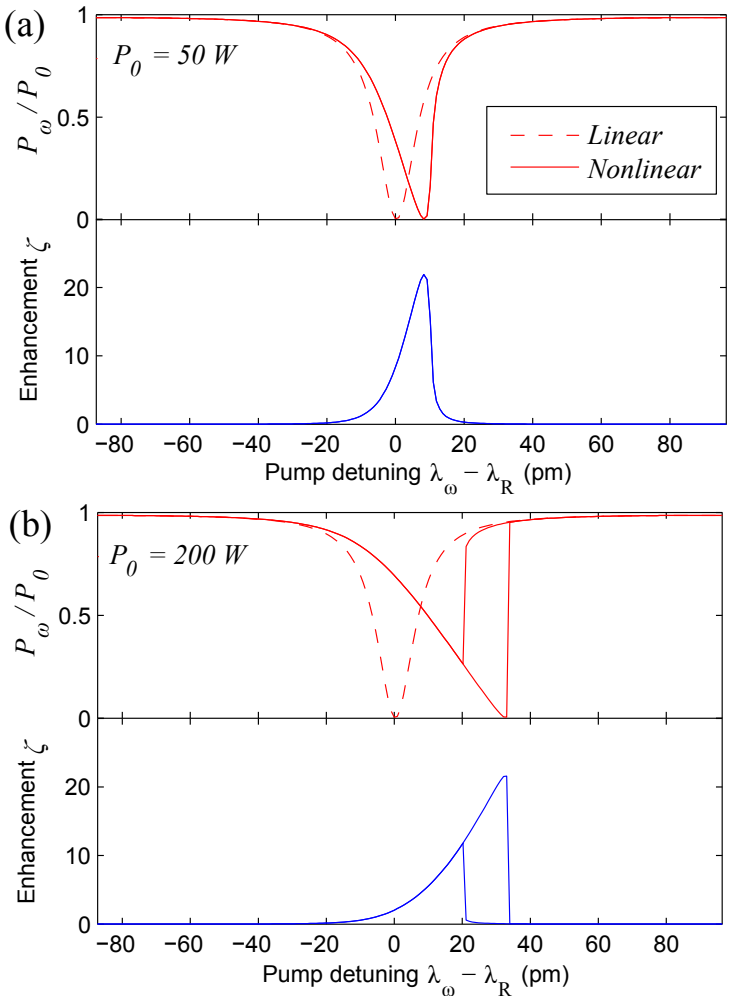

FIGURE 5.6: Pump transmission and resonant second harmonic efficiency enhancement spectrum for a loop resonator with a pump power of (a) 50 W and (b) 200 W. Solid and dashed lines represent linear and nonlinear spectra respectively. Parameters: 4 mm diameter loop, $\alpha_{\omega,2\omega} = 1$ m^{-1}, $\Delta K = 0.6$ ($\kappa = 8.5 \times 10^4$ m^{-1}, $L_c = 50$ μm).

To model SHG in a loop resonator, we apply essentially the same theoretical framework and notation as for resonantly-enhanced THG in section 4.2 and simply adapt Eqns. 4.1–4.5 on page 45 by using Eqn. 5.4 in order to incorporate the ρ_2 SHG term.

For a pump power of 50 W at 1.55 μm wavelength, Fig. 5.6(a) plots the pump and enhancement spectra against detuning from the linear resonance wavelength, where the pump is taken to be phase matched with the TM$_{01}(2\omega)$ mode. The conversion can be enhanced by over $\zeta = \eta/\eta_0 = 20$ dB near resonance in a 4 mm diameter loop, where $\eta_0 = 1 \times 10^{-5}$ is the efficiency for a straight microfibre of the same length. For the low pump powers discussed here, the maximum possible enhancement increases quadratically with increasing recirculating power within the loop and can be estimated as:

$$\zeta \approx \left[\frac{1 - \sin^2(\kappa_\omega L_c)}{(1 + \sin(\kappa_\omega L_c) e^{-\alpha_\omega L_0})^2} \right]^2 \tag{5.14}$$

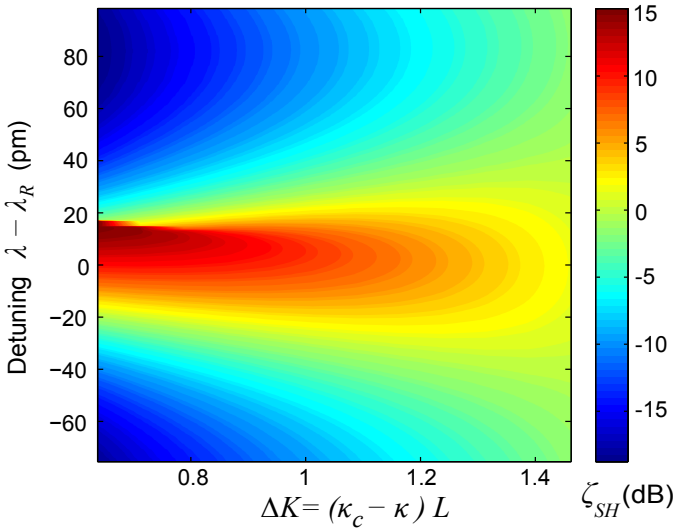

FIGURE 5.7: The second harmonic enhancement ζ against resonance detuning $\delta\lambda$ and proximity to critical coupling ΔK. Regions with $\zeta > 0$ dB experience resonantly enhanced SHG. $P_0 = 200$ W, $\lambda_1 = 1.55$ μm, loop diameter = 4 mm, $\alpha_{\omega,2\omega} = 1$ m^{-1}.

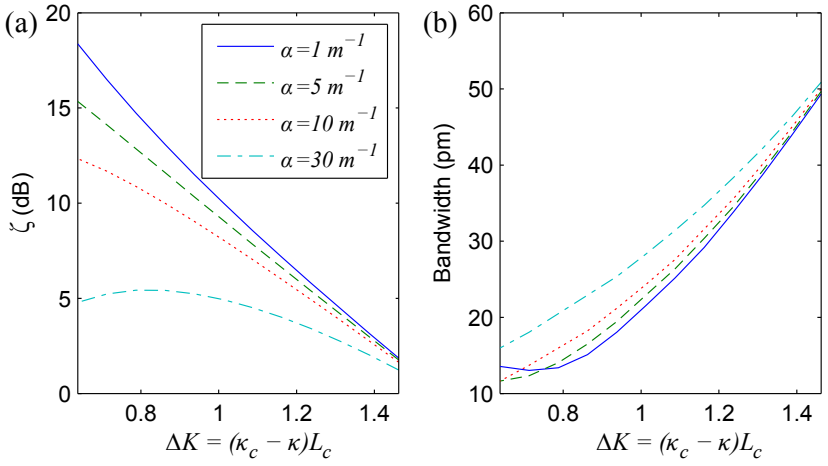

FIGURE 5.8: (a) The peak enhancement ζ against proximity to critical coupling ΔK, for different values of loss α and (b) the corresponding FWHM bandwidth of the enhancement. Other parameters same as Fig. 5.7

Using a higher pump power of 200 W in Fig. 5.6(b), the maximum enhancement is roughly the same since the pump remains undepleted, but due to its higher power the output conversion becomes 16 times greater than for the 50 W case, giving a reasonable conversion of $\eta = 1.6$ % despite the short SHG interaction length.

In Fig. 5.6, the loop is close to critical coupling κ_c with $\Delta K = (\kappa_c - \kappa)L_c = 0.6$, which limits the bandwidth to only a dozen pm. If weaker coupling strengths are chosen, i. e. larger ΔK, we can improve the bandwidth as shown in Figs. 5.7 and 5.8. For example, when $\Delta K = 1$, the FWHM bandwidth is roughly three-fold wider. In addition, the region where $\zeta < 0$ (where the pump light bypasses the loop via the coupling region) becomes narrower by roughly 30 pm which is beneficial if the pump central wavelength

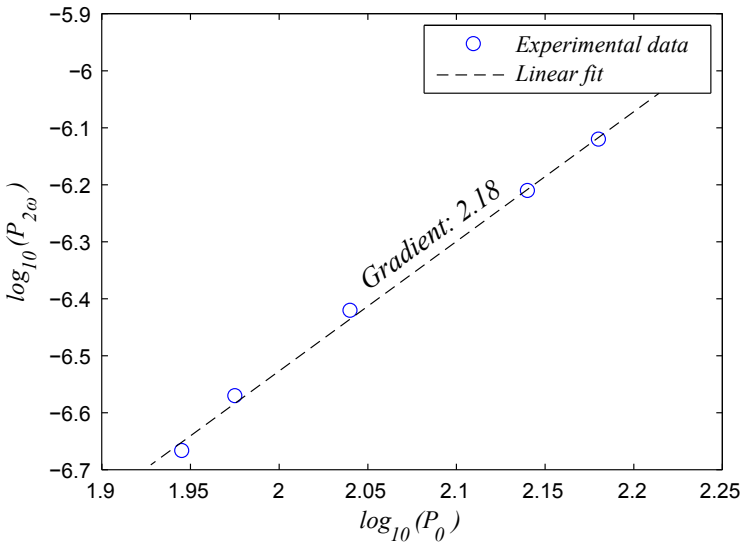

FIGURE 5.9: A logarithmic plot of the experimentally measured peak harmonic power against the peak pump power, when pumping between peak powers of $P_0 = 90$ to 150 W. Dotted line indicates a linear fit. Taper diameter is 0.7 μm and SHG interaction length is 200 μm.

cannot be finely tuned, but the peak enhancement falls to only 10 dB due to the weaker resonance.

5.4 Experiment for resonantly enhanced second harmonic generation

Due to the inherently low second order nonlinearity in silica microfibres, a high conversion of several percent would require diameter uniformity on the order of nm over microfibre lengths of $>$ 5 cm, which unfortunately exceeds the capabilities of the tapering rigs available today. We therefore focus our experiments on resonantly enhanced SHG using microfibre loop resonators, in which the resonant field intensity provides a high efficiency and so diameter uniformity is only required over a much shorter interaction length of a few mm. The following work was conducted with Marcelo A. Gouveia (UNICAMP, Brazil) and Rand Ismaeel (ORC, University of Southampton), in which the SHG is characterised before and after configuring a taper into loop resonator.

Results from two tapers (with similar geometries) are discussed here; the first was investigated to verify that the harmonic power increases quadratically with pump power (to ensure that the detected signal indeed arises from the $\chi^{(2)}$ process), and the second taper was used as loop resonator to demonstrate the resonant SHG enhancement.

Both silica tapers were fabricated from single mode fibre (SMF-28) using the same microheater-based tapering rig and procedure as described in section 3.4.1. The tapers were pulled whilst being pumped with 4 ns 200 kHz $\lambda_1 = 1.55$ μm pump pulses from

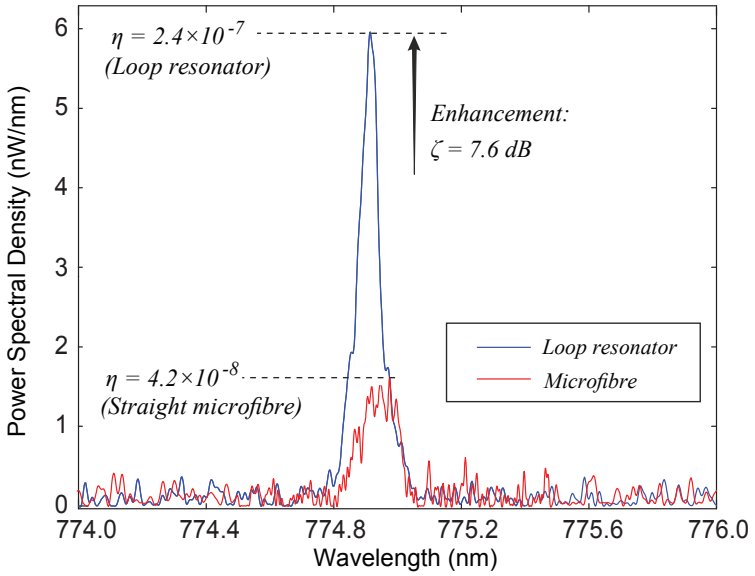

FIGURE 5.10: Experimentally recorded second harmonic spectra from a silica taper before and after arranging into a loop resonator, showing the resonant enhancement. Waist diameter is 0.7 μm and SHG interaction length is 200 μm. Pump parameters: $P_0 = 90$ W, 5 ns 200 kHz 1.55 μm wavelength pulses.

the source as shown in Fig. 3.9, so that the rig could be stopped as soon as the second harmonic signal was detected on an OSA connected to the taper output (via a 1300 nm cutoff shortpass filter).

Firstly, for the first taper, the diameter was measured with SEM images as 0.70 μm, which allows phase matching with the $HE_{21}(2\omega)$ harmonic mode within the transition regions close to the waist. Although the full taper length was 2 cm, the SHG interaction length (the distance over which the diameter is within 1 nm of the critical phase matching diameter, 777 ± 1 nm) is roughly 200 μm.

Since the experiment aims to provide a preliminary demonstration of the resonantly enhanced SHG, we use low pump powers to minimise competing nonlinear effects such as SPM-induced broadening or Raman in the fibre. For peak pump powers P_0 between 90 to 150 W, Fig. 5.9 verifies that the harmonic power increases roughly quadratically with increasing P_0. At $P_0 = 90$ W, the efficiency is low at only $\eta = 2.5 \times 10^{-9}$, and rises to 5×10^{-9} if the pump power is increased to 150 W. Therefore, since η only increases linearly with P_0, using higher pump powers to boost the conversion is not particularly effective, unless P_0 is increased by orders of magnitude.

To demonstrate the resonant efficiency improvement, we fabricated a second taper sample with similar specifications and a diameter of 0.7 μm. An efficiency of $\eta = 4.2 \times 10^{-8}$ was observed at 90 W peak pump power for the straight taper, which is close to the theoretical conversion of 8×10^{-7} over a 200 μm phase matched length. The harmonic spectrum is shown in Fig. 5.10.

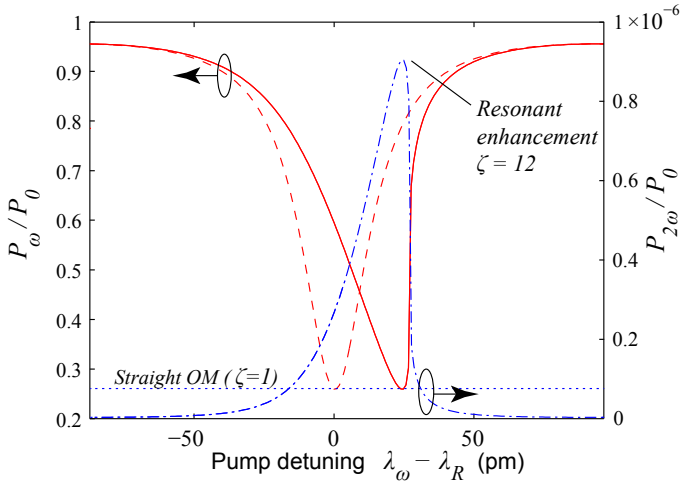

FIGURE 5.11: Simulated resonantly enhanced SHG from a loop resonator with properties matching the experimental loop, for the linear pump (dash), nonlinear pump (solid) and second harmonic (dot-dash) transmission, when the pump wavelength is detuned from a resonance near 1.55 μm. The dotted line shows the SHG conversion from an equivalent straight microfibre. Parameters: Loop length $L_0 = 12$ mm, $L_{\mathrm{SHG}} = 200$ μm, $P_0 = 90$ W, $\Delta K = 0.81$ ($\kappa_\omega = 7.8 \times 10^4$ m^{-1}, $L_c = 50$ μm), $\alpha = 10$ m^{-1}.

Next, the taper was rearranged into a 4 mm diameter loop resonator with a Q-factor of 1.6×10^4. The simulated linear/nonlinear pump and second harmonic spectrum for such a device in Fig. 5.11 predicts enhancements up to $\zeta = 12$, i. e. 10.8 dB (the resonator parameters were chosen by fitting the theoretical and experimental linear spectra).

Experimentally, the conversion for the loop was calculated as $\eta = 2.4 \times 10^{-7}$, which confirms an enhancement of 7.6 dB as shown in Fig. 5.10 and corresponds to a recirculating pump power of 210 W inside the loop. The measured value of ζ is lower than the theoretical value most likely due to the nonlinear broadening of the pump pulse, as any wavelength components which lie outside of the narrow FWHM of resonance (0.05 nm) will not benefit from the resonance.

5.5 Conclusion

The study of second harmonic generation in silica microfibres represents an interesting area of research since it relies upon a second order nonlinearity arising from the often overlooked surface anisotropy and bulk multipolar effects. We have modelled the contributions from both phenomena, which together would give an estimated SHG efficiency of $\eta \approx 3$ % over a 5 cm microfibre for a 1 kW 1.55 μm wavelength pump.

As a potential method for improving the SHG conversion, we have simulated and successfully observed resonantly enhanced SHG by producing a microfibre loop resonator in which the pump light is near resonance, giving an efficiency 7.6 dB higher than the original straight microfibre. The efficiency of $\eta = 4.2 \times 10^{-7}$ when pumped at a peak power

of only 90 W is comparable to that reported in straight tapers where the powers were 10 times greater [16]. It is envisaged that this enhancement can be further increased up to 20 dB, primarily by improving the coupling within the resonator.

Chapter 6

Polarisation Effects in Microcoils

First proposed in 2004 [23], optical microcoil resonators (OMRs) have attracted much research interest for their unique optical properties including strong dispersion, a large external evanescent field, slow light and high Q factor resonances [23, 29, 79]. These characteristics arise from the OMR structure in which a microfibre is tightly wrapped around a central rod to evanescently couple the adjacent turns, allowing specific wavelengths to recirculate within the coil and thus produce a resonance spectrum.

In this chapter, we first introduce the microfibre resonators and motivation in section 6.1. Next, section 6.2 presents the linear polarisation dependent effects in microcoils arising from fibre twist or birefringence, to develop an understanding of the resonance characteristics. We also explore an interesting but often overlooked phenomenon termed 'Berry's phase,' which can couple light between two orthogonal polarisations co-propagating in a helical waveguide structure such as an OMR. Finally, section 6.3 extends the work into the nonlinear regime and also outlines possible applications for nonlinear signal processing using OMRs.

6.1 Overview

Since a considerable fraction of the mode propagates in the surrounding air, microfibres are often used to evanescently couple light into various optical structures such as microspheres [80, 81, 82] or other waveguides [83, 84]. However, by bending the taper onto itself, light can self-couple between different segments of the same microfibre to form optical resonators, including the loop [20, 21, 29], knot [22, 85, 86] and microcoil [23, 29]. In addition, there are also more complex variants based on two or more microfibres such as the racetrack [87], reefknot [88], and multiport microcoil resonator [89], which offer four-port functionality. Together, these form a class of resonators which benefit from low-cost, high Q-factor (up to $Q > 10^5$ demonstrated [90]), relatively straightforward fabrication and negligible input/output coupling losses if the fibre pigtails are retained.

For wavelengths near resonance, light is repeatedly coupled back into resonator and so the internal field strength can grow to orders of magnitude higher than the input level, which (in conjunction with the high microfibre effective nonlinearity of $\gamma \approx 0.1$ $\mathrm{m}^{-1}\mathrm{W}^{-1}$) allows nonlinear effects to be observed at relatively low powers – indeed, we have seen in Chapters 4 and 5 that the loop resonator can be used to resonantly enhance the third and second harmonic generation efficiency. Previous studies have also shown that OMRs can exhibit nonlinear characteristics when detuned near resonance, such as bistability and nonlinear switching of the output, at powers potentially down to only dozens of watts in silica OMRs [30].

The theoretical models exploring OMR transmission in the linear and nonlinear regime [23, 30] have so far negelected polarisation effects since the core is assumed perfectly circular and relaxed, with degenerate and uncoupled x and y polarisations propagating independently and identically. In general however, the microfibre can become slightly twisted during OMR manufacture, leading to coupling between these orthogonally polarised modes. Furthermore, simulations by Wang et al. on polarisation coupling in microfibre knot and loop resonators (the latter akin to an OMR with only 1 turn) indicate that such effects can significantly alter the resonance spectrum, and must be accounted for during microfibre resonator design [86]. It is therefore reasonable to expect that the OMR will also exhibit a polarisation dependency reflected not only in the linear spectrum, but also the nonlinear transfer characteristic and hysteresis properties. The following three sections thus aim to comprise an accurate and polarisation sensitive linear and nonlinear model for OMRs.

6.2 Linear polarisation dependent behaviour

6.2.1 Twisted birefringent microcoils

This section discusses the effect of fibre twisting and birefringence on the transmission of OMRs by formulating and solving the equations describing the simultaneous propagation of both the x and y polarised modes.

Although the birefringence $B = n_{\mathrm{eff}}^{y} - n_{\mathrm{eff}}^{x}$ for the parent SMF is negligibly small ($B \approx 10^{-6}$), the tapering process may inadvertently induce a linear form birefringence by core deformation. The birefringence of elliptical microfibres, calculated in COMSOL software and plotted in Fig. 6.1, shows that even for a small core ellipticity of $e = 1.01$ (where $e = b/a$ is defined as the ratio of the major and minor axes), the birefringence can reach up to $B = 10^{-3}$. On the other hand, much larger birefringences of -10^{-2} can be purposely achieved as reported in 'Hi-Bi' silica microfibres with elliptical and rectangular cross sections [91, 92, 93]. If the taper is gently twisted, the polarisations of

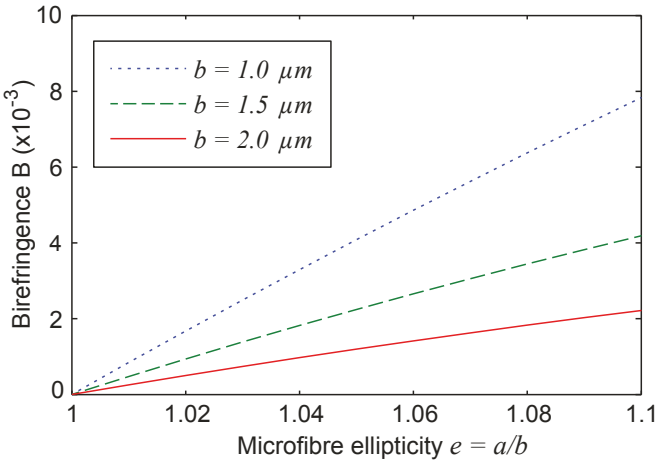

FIGURE 6.1: Simulated birefringence of elliptical fibres for different core widths b and ellipticities $e = a/b$. $\lambda = 1.55\ \mu$m.

the propagating modes would also be rotated, and we therefore analyse the simultaneous influence of fibre birefringence and twist upon the output spectrum.

6.2.1.1 Theory

We begin by defining the coordinate system shown in Fig. 6.2 along with the microcoil schematic. Whereas the laboratory axes (X, Y) are fixed and invariant, the local (x, y) axes are aligned with the birefringent axes of the fibre and hence rotate with the fibre's twist angle $\theta(z)$. It is convenient to adopt the local coordinate system since a linearly polarised mode propagating through small twists would maintain its polarisation angle in the x-y plane, whereas the direction of polarisation in the laboratory frame (X, Y)

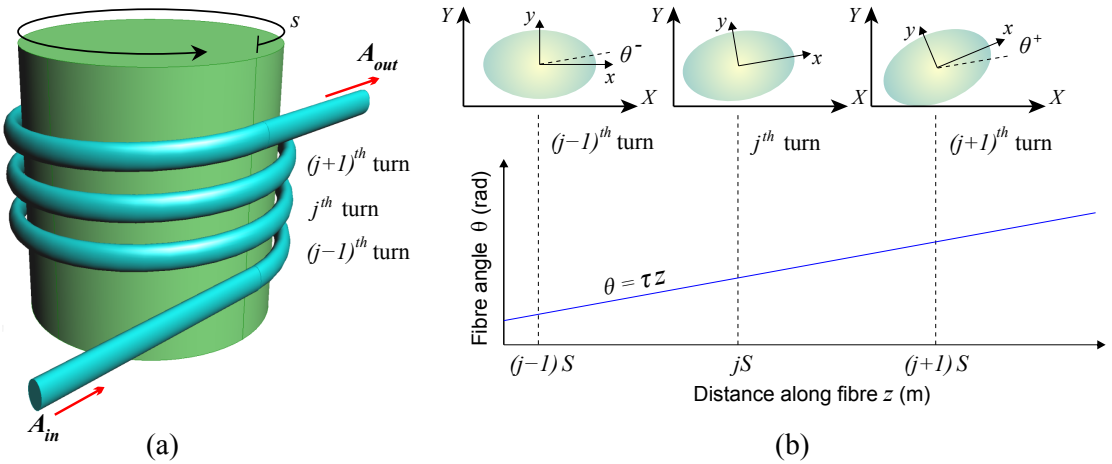

FIGURE 6.2: (a) Schematic of the microcoil and (b) a cross section of three neighbouring turns showing the local fibre axes (x, y) and laboratory axes (X, Y), when the fibre is twisted at an angle $\theta(z)$.

would constantly change. Along these axes, the corresponding x and y-polarised complex slowly-varying electric field amplitudes in the j^{th} turn of the coil are governed by the following couple-mode differential equations, which are adapted from those of the standard microcoil [23]:

$$\begin{aligned}\frac{dA_j^x}{ds} &= i\kappa_0\left[A_{j-1}^x\cos(\theta^-) + A_{j-1}^y\sin(\theta^-) + A_{j+1}^x\cos(\theta^+) - A_{j+1}^y\sin(\theta^+)\right] \\ &\quad + i\kappa_{xy}A_j^y\end{aligned} \tag{6.1a}$$

$$\begin{aligned}\frac{dA_j^y}{ds} &= i\kappa_0\left[A_{j-1}^y\cos(\theta^-) - A_{j-1}^x\sin(\theta^-) + A_{j+1}^y\cos(\theta^+) + A_{j+1}^x\sin(\theta^+)\right] \\ &\quad + i\kappa_{yx}A_j^x + i\Delta\beta A_j^y\end{aligned} \tag{6.1b}$$

where $\Delta\beta = \beta^y - \beta^x = 2\pi B/\lambda$ is the propagation constant mismatch due to birefringence, κ_0 is the coupling coefficient between neighbouring turns of the OMR and the angles θ^+ and θ^- shown in Fig. 6.2(b) represent the difference in twist angle between adjacent turns:

$$\theta^- = \theta_j - \theta_{j-1} = \theta(z) - \theta(z-S) \tag{6.2a}$$

$$\theta^+ = \theta_{j+1} - \theta_j = \theta(z+S) - \theta(z) \tag{6.2b}$$

where S is the length of one loop of the microcoil. The sine and cosine terms arise from the twist dependent coupling between the two polarisations in adjacent turns. For example, regarding the coupling between A_j^x and the modes in the $(j-1)^{\text{th}}$ turn, since the latter are rotated by θ^- relative to the j^{th} turn, A_j^x will couple to the components of these modes which are polarised in the same direction as itself, i. e. $A_{j-1}^x\cos(\theta^-)$ and $A_{j-1}^y\sin(\theta^-)$.

Practically, linear twists are the easiest to fabricate in the OMR fibre by simply rotating one end of the microfibre whilst fixing the other, and hence we shall focus on twist functions taking the form $\theta(z) = \tau z$, where the torsion τ is a left-handed twist coefficient measured in radians per metre along the fibre axial length. Thus, the sine and cosine terms in Eqn. 6.1 will be longitudinally invariant, since $\theta^- = \theta^+ = \tau S$ is constant along the OMR fibre.

For the first turn, Eqn. 6.1 is modified so that it only couples to the second turn, and likewise for the final turn the light will only couple to the penultimate turn.

Note that the fibre ellipticity is assumed to be sufficiently low ($e < 1.1$) such that the linearly polarised fundamental modes are essentially identical and thus can couple from one to the other with similar coupling coefficients κ_0.

Whilst a gently twisted birefringent fibre is expected to be polarisation maintaining, this is untrue for stronger twists since the mechanical strain will induce an additional, circular birefringence which may be comparable to that of the existing linear birefringence, i.e.

the twist is non-adiabatic. In Eqn. 6.1, this is modelled by the κ_{xy} and κ_{yx} terms, where the coupling coefficients are derived from the fibre elastic properties [94]:

$$\kappa_{xy} = -\kappa_{yx} = -\frac{in_0^2 p_{44}\tau}{2} \tag{6.3}$$

From the elastooptic tensor of silica, the value of p_{44} is -0.075 [95], and n_0 is the refractive index. Since κ_{xy} and κ_{yx} are imaginary, they rotate the polarisation, which combined with the fibre's inherent linear birefringence will cause the polarisation to evolve elliptically. For the small twist angles $\tau < 100$ rad/m considered in the discussion however, these terms are relatively unimportant since they are roughly 2 orders of magnitude smaller than the κ_0 terms, but have nonetheless been included for completeness.

Continuity of the field amplitude and phase from the output of each turn to the start of the next requires the amplitudes to satisfy:

$$A_j^{x,y}(0) = \begin{cases} A_{\text{in}}^{x,y} & j = 1 \\ A_{j-1}^{x,y}(S)\exp\left(i\beta^x S\right) & j = 2\ldots n \end{cases} \tag{6.4}$$

Note that β^x is used in both the x and y polarisations' boundary conditions since the phase difference due to birefringence accumulated per turn has been accounted for by the $i\Delta\beta A_j^y$ term in Eqn. 6.1b. The fibre loss α is introduced as the imaginary component of β, and can be assumed to be roughly identical for both polarisations:

$$\beta^{x,y} = \frac{2\pi n_{\text{eff}}^{x,y}}{\lambda} + i\alpha \tag{6.5}$$

At the output the amplitude transmissions are:

$$T^{x,y} = \frac{A_n^{x,y}(S)\exp\left(i\beta^x S\right)}{\sqrt{|A_{\text{in}}^x|^2 + |A_{\text{in}}^y|^2}} \tag{6.6}$$

In practice, the coupling parameter κ_0 would be different between x-x and y-y polarised modes since the fundamental HE_{11} mode is slightly asymmetric [96]. However, the difference is generally small compared to the sine and cosine factors in Eqn. 6.1 unless the microfibre is highly elliptical and so κ_0 is approximated to be the same between both polarisations.

To solve Eqs. 6.1 and 6.4, we use a modified Newton method similar to that described in reference [30], to calculate the amplitudes within an error of $< 10^{-6}$. Further details of the numerical solution algorithm, which was implemented in MATLAB, can be found in Appendix C.

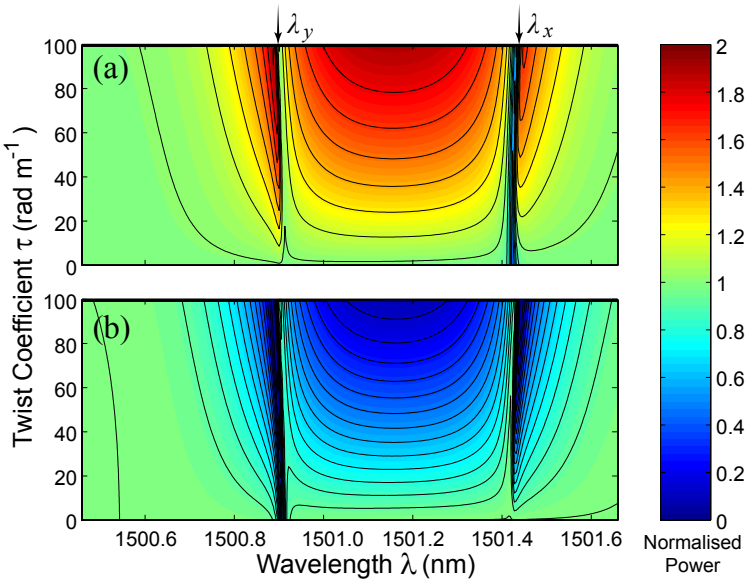

FIGURE 6.3: The effect of twist torsion coefficient τ on the (a) x and (b) y polarised output spectrum. Parameters: 3 turns, $n_{eff}^{x} = 1.45$, $B = 10^{-3}$, $\kappa_0 = 5400$ m^{-1}, $\alpha = 4.6$ m^{-1}, $S = 1$ mm. Input amplitudes $A_1^x = 1$, $A_1^y = 1$. Wavelength range covers one FSR.

6.2.1.2 Discussion

In the following simulation results, we shall study (i) the effect of different values of twist torsion τ in the presence of a fibre birefringence on the resonance characteristics, (ii) OMRs with different numbers of turns, and (iii) the effect of birefringence on the linear spectrum for each polarisation.

For a 3 turn OMR, introducing a fibre twist significantly alters the output spectrum, as shown Fig. 6.3 over one free spectral range (FSR). The input was linearly polarised at $\phi = \pi/4$ rad, with an input amplitude of $A_1^x = A_1^y = 1$, and the output power is taken to be normalised so that $P = |A|^2$. In the absence of twist ($\tau = 0$ rad/m), the two polarisations are uncoupled and propagate independently, with both the x and y spectra only showing their own fundamental resonance dips at $\lambda_x = 1501.4$ nm and $\lambda_y = 1500.9$ nm respectively. The difference in these resonant wavelengths is solely due to the modes' different β and so the separation is given by $\Delta\lambda \approx B\lambda/n_{\text{eff}}$.

As τ increases, a peak in the x transmission forms at λ_y, whilst the extinction of the existing y resonance dip is enhanced, because some of the initially y polarised input light couples into the x polarisation which is off-resonance at λ_y and can be transmitted without being coupled back into the OMR. Therefore, the overall absorption is reduced and indeed the total output power is 10% larger than the $\tau = 0$ rad/m case as illustrated by the close up of the λ_y resonance in Fig. 6.4(a), for a small twist of $\tau = 30$ rad/m.

On the other hand, at λ_x, coupling from the y to x polarisation also occurs but since this wavelength corresponds to an x resonance, more power is consequently recirculated than

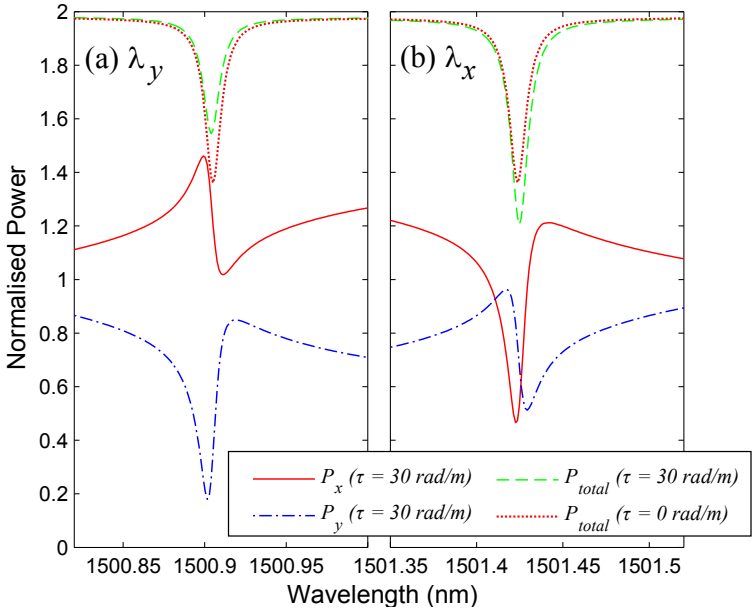

FIGURE 6.4: Close up of resonances at (a) $\lambda_y = 1500.9$ nm and (b) $\lambda_x = 1501.4$ nm, showing the x polarised output (solid), y polarised output (dot-dash) and total power at output (dashed) for a twist of $\tau = 30$ rad/m. The total output power for $\tau = 0$ rad/m is also shown (dotted). Other parameters same as Fig. 6.3.

if there were no twist. Thus the total absorption is greater as confirmed by Fig. 6.4(b), in contrast to the previously described situation at λ_y.

This effect occurs even with weak twists of $\tau = 10$ rad/m, or $\sim 1°$/turn, because at the high Q resonance the recirculation of light within the OMR increases the effective length over which polarisation coupling occurs. To confirm this, when κ_0 was adjusted to give lower Q resonances, a stronger twist was required to achieve the same result.

In the results discussed so far, light couples predominantly from the y to x mode due to the choice of twist direction and input polarisation angle: for a positive τ, the x axis is rotated towards the original polarisation of the light ($\pi/4$ rad for $A_1^x = A_1^y$). Using a negative τ to simulate right handed twisting, or alternatively using $A_1^x = -A_1^y$, would reverse the roles of the two polarisations and favour coupling from the x to y mode instead. Since both scenarios are essentially the same, we focus on positive twists.

To study the effect of twist on resonance behaviour further, Fig. 6.5 shows how the output power and extinction ratio of the y polarised output at λ_y change with twist. Increasing τ from 0 to 80 rad/m raises the extinction ratio (as more light is converted into the x state), until it peaks with an improvement of over 27 dB. Increasing the twist further towards 100 rad/m will however rotate the polarisation enough to couple light back into the high transmission x state and so the extinction ratio falls.

Interestingly, for $\tau > 30$ rad/m, a band appears between $\lambda_y < \lambda < \lambda_x$ where the output is largely x polarised, despite the input light being originally polarised at 45°. For example,

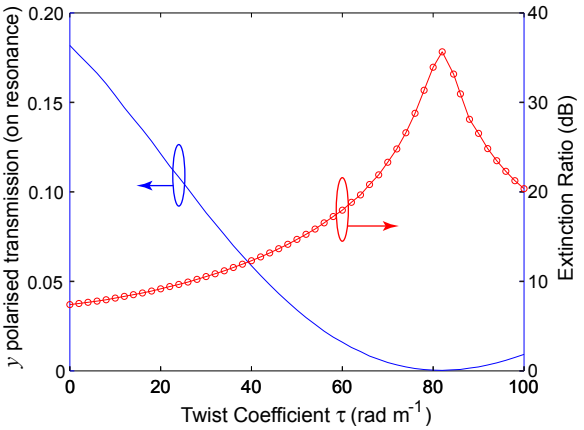

FIGURE 6.5: The y polarised transmission at the resonance near λ_y (solid line) and the corresponding extinction ratio (circles) as a function of twist τ. Same parameters as Fig. 6.3.

with $\tau = 100$ rad/m, over 95% of the output power is x polarised at $\lambda = 1501.2$ nm. For wavelengths outside this range the x and y output powers are roughly equal and close to 1 (i.e. similar to the original input) which indicates the effects of twist can be significant even when off resonance.

In general, for a large birefringence of $B = 10^{-3}$ the fibre is highly polarisation maintaining for $\tau < 100$ rad/m and hence the aforementioned effects arise primarily from the relative rotation of the modes in the neighbouring turns, rather than from the strain induced cross-polarisation coupling (the κ_{xy} and κ_{yx} terms). It should be noted that the output is almost always elliptically polarised regardless of the input polarisation state, due to the accumulated phase difference between the x and y propagating modes as well as their different output amplitude.

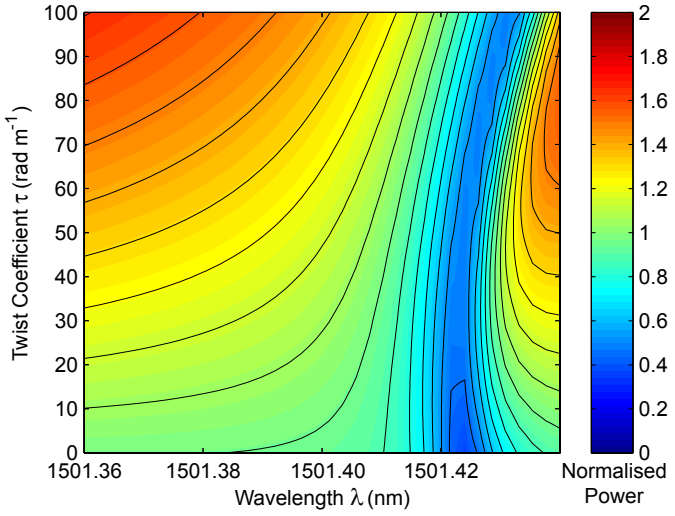

FIGURE 6.6: Close up of the resonance at λ_x in the x polarised output spectrum, showing the resonance wavelength shift with increasing twist. Same parameters as Fig. 6.3.

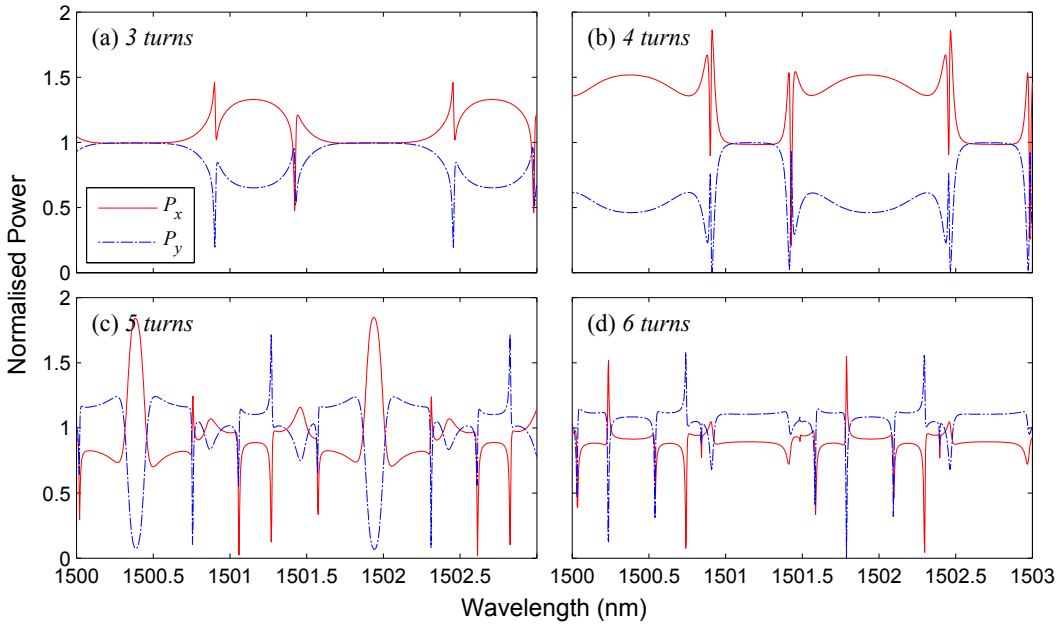

FIGURE 6.7: Output spectra for twisted birefringent fibre OMRs with (a) 3 turns (b) 4 turns (c) 5 turns (d) 6 turns. Coupling is $\kappa_0 = 5400, 5000, 4200, 4200$ m^{-1} in (a)-(d) respectively. $\tau = 30$ rad/m, other parameters same as Fig. 6.3. Wavelength range covers approximately two FSR.

Both the resonant wavelengths λ_x and λ_y vary slightly with twist. Fig. 6.6, which focuses on the wavelength range around the x resonance, shows that increasing τ from 0 to 100 rad/m causes the resonance to shift to a longer wavelength by +0.02 nm, or 1.3% of the FSR. Whilst this shift is not particularly large, it is nonetheless comparable to the resonance's full-width at half maximum (FWHM) value of 10^{-2} nm and therefore sufficient to change an on-resonance wavelength to off-resonance.

Although the discussion so far has been related to OMRs with $n = 3$, similar behaviour can be seen in coils with more turns as shown in Fig. 6.7(a)-(d), which compares typical spectra for OMRs with $n = 3$, 4, 5 and 6 turns. For example, the $n = 4$ OMR also provides a spectrum with wavelength bands over which one polarisation is dominant over the other at the output, and in all four spectra, the effect of polarisation coupling is most obvious at resonance. In the case of the five and six turn microcoil, higher order resonances are supported which give rise to a complex transmission structure.

In the 3 and 4 turn OMR from Fig. 6.7 (a) and (b), the coupling is largely from the y to x mode for reasons explained earlier. For OMRs with more turns however, the coupling can no longer be understood so intuitively since the extra turns introduce more intricate possible routes for the light to take. The five turn OMR's output spectrum alternates between being predominantly x polarised to y polarised and vice versa, while the 6 turn OMR output is mostly y polarised with the exception of certain resonances.

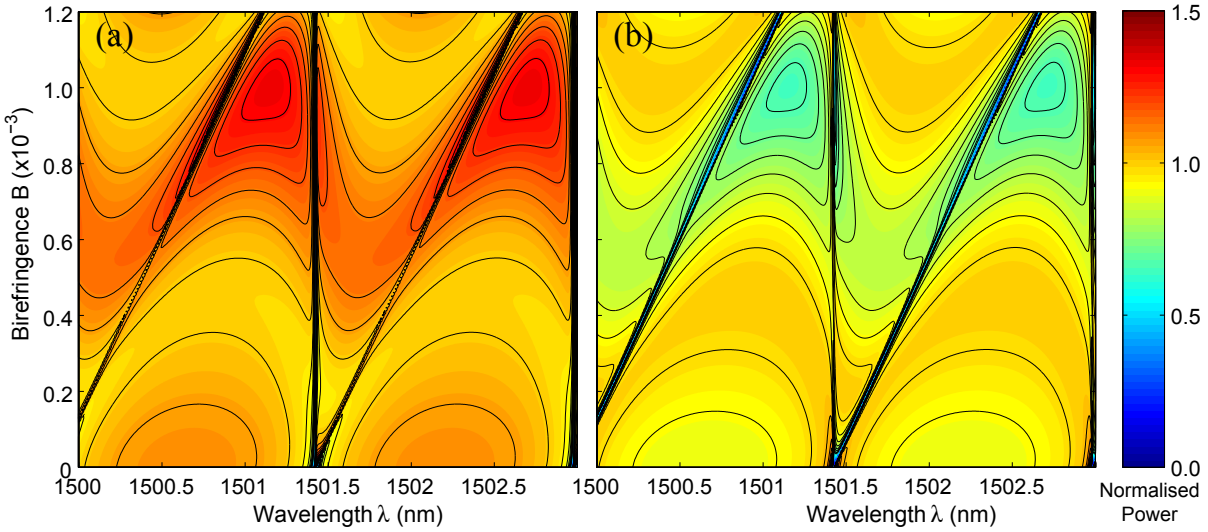

FIGURE 6.8: Effect of birefringence on the (a) x and (b) y polarised output spectrum. $\tau = 30$ rad/m and other parameters are the same as Fig. 6.3.

Finally, the dependance on the birefringence B is summarised in Fig. 6.8. In the plots, n_{eff}^{x} is kept constant at 1.45 and n_{eff}^{y} is increased from 1.45 to 1.4512, which has the effect of shifting the y resonances to longer wavelengths whilst keeping the x resonances stationary. When $B < 2 \times 10^{-4}$, the spectrum is characterised by the original and twist-induced resonances and in between these wavelengths, the x output power is only marginally higher than the y output.

On the other hand, for a moderate birefringence of $B \approx 7 \times 10^{-4}$, the x output power is 1.5-1.7 times greater than the y output across the non-resonant wavelengths. Further increasing B above 10^{-3} causes the spectrum to evolve into alternating wavelength bands where the output power varies between being equally distributed in the two polarisations and being mostly x polarised. Interestingly, the width of these bands appears to be determined by the spectral proximity of the resonances; hence by adjusting the birefringence and twist it may be possible to utilise these for filter applications.

6.2.1.3 Summary

We have shown that the transmission of microcoils based on birefringent or twisted microfibres is strongly polarisation sensitive, especially near resonance where even a mild cross-polarisation coupling mediated by a light twist can become greatly amplified by the recirculation of the resonant polarisation mode. For example, the extinction ratio can be either improved or reduced, depending on the direction of twist.

Away from resonance, twisting may also introduce broad wavelength ranges where the output is primarily polarised in one direction only, even if the input power was originally

evenly distributed between the x and y modes. The width of these spectral bands, and to some extent their output polarisation direction, is governed by the fibre birefringence.

6.2.2 Berry's phase magnification in microcoils

In the previous section, the anisotropy between the x and y polarised output spectra from the microcoil is a direct result of the microfibre twist and birefringence. Under certain conditions however, it is still possible for the two polarisations to interact significantly in the linear domain even if the fibre is neither twisted nor birefringent, due to effects of the Berry's phase ϕ_B as explained in this section.

6.2.2.1 Theory

When linearly polarised light is guided through a non-planar curved path in space, such as the helix of a microcoil, it will acquire a Berry's phase which is detectable as a rotation of the plane of polarisation by an angle equal to ϕ_B. The generation of Berry's phase is well documented both theoretically and experimentally [97, 98, 99], with much research driven by its manifestation in various quantum mechanical and optical phenomena. More recently, the amplification of Berry's phase using ring resonators was observed by Golub [100, 101], and in this section we show that it is also possible to accumulate a large ϕ_B in a microcoil which is on resonance. Note that in the previous two sections, as well as current literature on OMR properties, the Berry's phase is neglected because the coil diameter D_c is assumed to be $10^2 - 10^3$ times greater than the pitch p between turns, so the turns are essentially planar and thus incapable of producing any large ϕ_B. The simulations here will focus on situations when these geometric assumptions are invalid, i. e. when the OMR diameter is of the order of 0.1 mm, under which the optical activity induced by ϕ_B becomes significant.

Before proceeding, it should be mentioned that the acquisition and size of Berry's phase is purely topological and independent of the wavelength, refractive index or initial state of polarisation. If the light traverses a closed curve, the polarisation plane will have been rotated despite being parallel transported perpendicular to it's propagation direction. As an analogy, Fig. 6.9 shows that if a pencil is placed flat at the north pole of a sphere and then translated around the path, whilst keeping the pencil horizontal against the surface at all times, when it is returned to the north pole it will not point in the same direction. This process, like the acquisition of the Berry phase, is therefore nonholonomic since the final state of the system depends on the path taken.

Mathematically, Berry's phase is found to be equal to the solid angle $\Omega(\sigma)$ subtended by the path traced σ out by the momentum vector $\boldsymbol{p}$ (which is coparallel with fibre axis) in

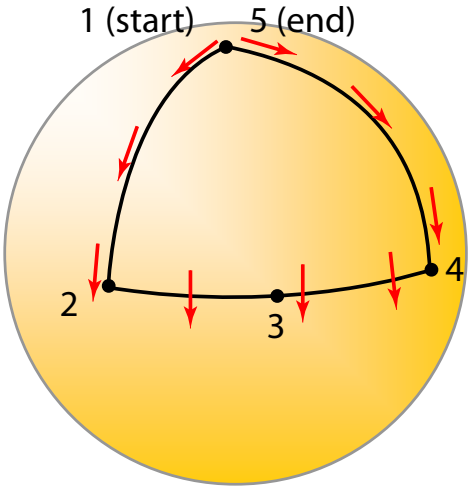

FIGURE 6.9: Analogy of anholonomy on a sphere, where the arrow does not return to its original state after being transported through a closed loop/cyclic change. (Similar result follows if arrow is perpendicular to the path rather than parallel). The system is nonholonomic since the final state of the arrow depends on the traversed path.

momentum space [98, 102]. For an OMR, this path is helical and so $\boldsymbol{p}$ traces out a cone and circular path as represented in Fig. 6.10 (the fibre incline angle is $\theta = \cos^{-1}(p/S)$ for a pitch p and loop length S). For one complete turn of the OMR, the initial and final momentum vector are identical which results in a closed loop path where $\Omega(C)$ can be calculated in circular coordinates (r,θ',ϕ') as:

$$\begin{aligned}\Omega(\sigma) &= \int_0^{2\pi}\int_0^{\theta} \sin\theta' d\theta' d\phi' \\ &= 2\pi(1-\cos\theta) \text{ [per turn]}\end{aligned} \tag{6.7}$$

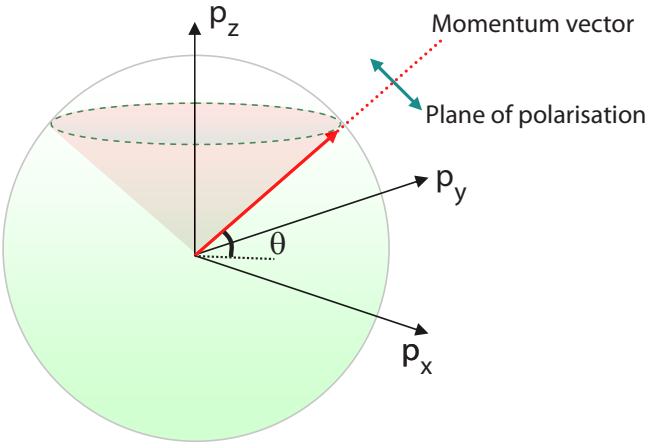

FIGURE 6.10: Momentum vector **p** of the light represented in momentum space, when propagating along a helix. The path traced out by the vector is indicated by the dashed line.

and hence the single turn Berry's phase has a magnitude of $2\pi\cos\theta$ per turn, or equivalently $\tau_h S$ where τ_h is the helical torsion:

$$\tau_h = \frac{2\pi p}{p^2 + 4\pi^2 R^2} \tag{6.8}$$

where R is the radius of the helix. Since ϕ_B increases linearly with distance in a uniform microcoil helix, we may describe the propagation of an initially linearly polarised light with x and y amplitudes of $A_x(z)$ and $A_y(z)$ in an uncoupled helix as follows [97]:

$$\frac{d}{dz}\begin{pmatrix} A_x \\ A_y \end{pmatrix} = \begin{pmatrix} -i\frac{C^2}{2\beta} & \tau_h \\ -\tau_h & 0 \end{pmatrix}\begin{pmatrix} A_x \\ A_y \end{pmatrix} \tag{6.9}$$

The off diagonal terms of the coupling matrix account for the optical activity due to Berry's phase, and bend induced propagation mismatch between the the polarisations is modelled by the C curvature term, where:

$$C = \frac{4\pi^2 R}{p^2 + 4\pi^2 R^2} \tag{6.10}$$

For a helix with a ~ 0.1 mm diameter, this term is generally several orders of magnitude smaller than τ_h and hence for an x polarised input the solutions A_x and A_y would resemble $\cos(\tau_h z)$ and $\sin(\tau_h z)$ functions respectively.

Next, to determine how the Berry's phase affects the transmission of the microcoil, we include the terms of Eqns. 6.9 into the microcoil differential equations of Eqns. 6.1 which incorporate the coupling between turns to obtain :

$$\frac{dA_j^x}{ds} = i\kappa_x\left(A_{j-1}^x + A_{j+1}^x\right) + \tau_h A_j^y + \left(i\Delta\beta_b - i\frac{C^2}{2\beta} - \alpha\right)A_j^x \tag{6.11a}$$

$$\frac{dA_j^y}{ds} = i\kappa_y\left(A_{j-1}^y + A_{j+1}^y\right) - \tau_h A_j^x - \alpha A_j^y \tag{6.11b}$$

with the boundary conditions to stipulate field continuity between each of the n turns of the coil:

$$A_j^{x,y}(0) = \begin{cases} A_{\text{in}}^{x,y} & j = 1 \\ A_{j-1}^{x,y}(S)\exp\left(i\beta S\right) & j = 2\ldots n. \end{cases} \tag{6.12}$$

where $\kappa_{x,y}$ are the coupling coefficients between two x or two y polarised modes in adjacent turns. In section 6.2.1, these were assumed to be equal ($\kappa_x = \kappa_y = \kappa_0$), but a more accurate model must be used here because the torsion term is small ($\tau_h \approx 10^{-1}$, compared to $\kappa \approx 10^3$) and so Berry's phase effects are highly sensitive to parameter variations. In the weakly guiding approximation, κ is usually analytically calculated from the modal overlap of electric fields in adjacent fibres as derived from perturbation theory [31]. However, the strong index contrast of the OMR microfibre ($\Delta n = 0.45$ for air surrounding) necessitates a more accurate numerical evaluation of $\kappa_{x,y}$ using

finite element analysis via COMSOL. A 2D mode analysis of two neighbouring air-clad silica microfibres with $D = 1$ μm diameters was parametrically swept through different separations pitches. At each pitch, the x and y odd/even supermodes were solved and the coupling deduced from the difference in their propagation constants:

$$\kappa_{x,y} = |\beta_{x,y}(\text{even}) - \beta_{\text{x,y}}(\text{odd})| \tag{6.13}$$

Due to the geometry, κ_y is slightly larger than κ_x since the former's field extends further into the turns above and below. Whilst the difference, it can significantly affect the resonance strength, since small polarisation dependent variations of either parameter can alter the Q factor. The OMR will therefore behave differently for different input polarisations.

For the first and last turns, Eqn. 6.11 is rewritten to couple only with the second and penultimate turns respectively. Of the two propagation mismatch terms, the first arises from bend-stress birefringence $\Delta\beta_b = \beta_x - \beta_y$ as calculated by adapting Eqn. 4 in [103] for a microfibre, and the second geometrically from the curvature $C = 4\pi^2 R/S^2$ [97]. Whilst the sum of these two terms is small, totalling ≈ -50 m^{-1}, they remain nonetheless comparable to the helical torsion term and must therefore be included (in particular, one would expect them to induce a slight shift between the x and y resonance frequencies and broaden the overall resonance lineshape).

6.2.2.2 Discussion

We shall study the Berry's phase effects for a 3 turn OMR with an air-clad silica 1 μm diameter microfibre operating at a wavelength of $\lambda = 1.55$ μm since these parameters correspond to OMRs which can be realistically fabricated. The pitch of $p = 2.5$ μm corresponds to a helix torsion of $\tau_h = 40$ m^{-1}. However, as the Berry phase is a purely geometric effect, similar results would be seen in OMRs with a different number of turns or made out of different materials.

Solving Eqns. 6.11 and 6.12 with a pitch of $p = 2.50$ μm produces the transmission spectrum in Fig. 6.11. Note that A^x and A^y would be uncoupled if the Berry phase term were neglected ($\tau = 0$), and hence Berry's phase effects are clearly seen in the coupling of light from one orthogonal state of polarisation to another. This is apparent in Fig. 6.11(a) where an x-polarised input propagating through a lossless coil produces an output with up to $\eta = P_y/P_{\text{Total}} > 97$ % of the power in the y polarisation. For this value of p, κ_x is closer to the critical coupling κ_c than κ_y (physically at the critical coupling κ_c light at a resonant wavelength λ_c is trapped indefinitely in the coil). The y polarised light being further from resonance couples out of the coil quicker than the x polarisation, which contributes to the high value of η.

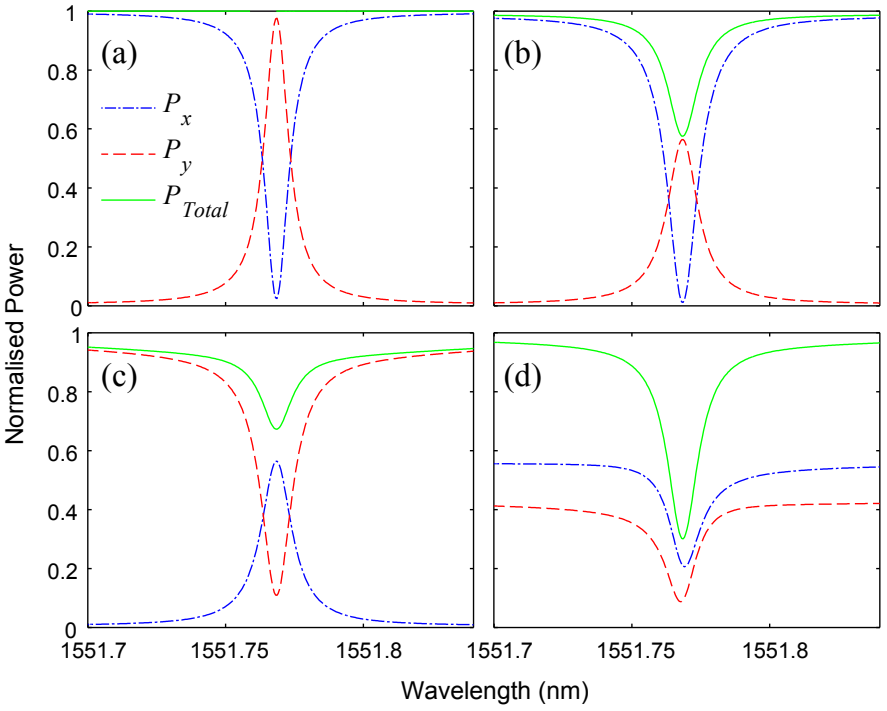

FIGURE 6.11: OMR output spectrum, showing the coupling of light between the x and y polarisation states due to Berry phase effects for an input polarised along (a) the x-axis, with no loss, (b) x-axis, with loss, (c) y-axis, and (d) at $\pi/4$ rad. For (b-d), the loss is $\alpha = 4.6$ m^{-1}. Parameters: 3 turn OMR, $|A_{\text{in}}| = 1$, microfibre diameter 1 μm, OMR diameter 0.2 mm, $p = 2.50$ μm, $\kappa_x = 5770$ m^{-1}, $\kappa_y = 6163$ m^{-1}, $\tau_h = 40$ m^{-1}.

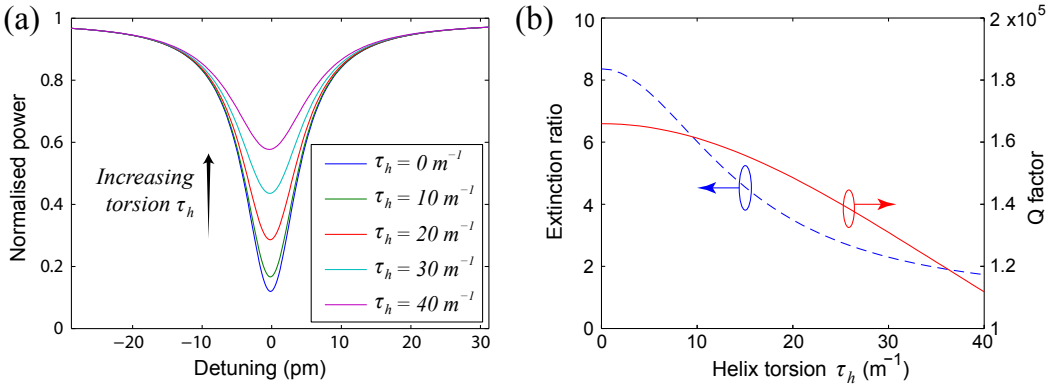

FIGURE 6.12: (a) Output power resonance spectrum against detuning from resonance for helix torsion values τ_h from 0 to 40 m^{-1}. (b) Resonance extinction ratio (dashed) and Q factor (solid) against helix torsion τ_h. Other parameters same as Fig. 6.11.

By comparison, an uncoupled helix ($\kappa_{x,y} = 0$) with the same geometry only has a Berry's phase of $\phi_B = 0.025$ rad and $\eta_0 = 6 \times 10^{-4}$, because the light only makes a single pass through the coil. The high degree of optical activity in an OMR is only observed near resonance; off-resonance however, $\eta < \eta_0$ since the light is simply coupled up the turns and out of the OMR.

In the more realistic lossy case of Fig. 6.11(b), η is marginally lower but remains sufficiently large to be detected experimentally, despite τ_h being over 100 times smaller than

$\kappa_{x,y}$. The Berry phase could also be increased by using a narrower OMR or wider pitch to increase the helical torsion.

Finally, Fig. 6.11(c) and (d) presents the effect input polarisation angle on the output power. Fig. 6.11(c) shows that a y-polarised input gives a significantly smaller polarisation rotation at resonance than before. This is due to two reasons: firstly the y resonance is intrinsically weaker, and secondly any light coupled into the x polarisation will be stored for longer within the coil, during which it will be partially coupled back into the y polarisation. When the input contains both x and y polarisations as in Fig. 6.11(d), the resulting spectrum varies strongly with geometry. The elasto-optic effects, though minor, induce a bend birefringence which shifts the x and y resonances apart by 10 pm, which is comparable to the resonance linewidth and results in an asymmetric total power P_T spectrum. The offset between the x and y resonance frequencies also exists for the cases in Fig. 6.11(a-c), so when the original input polarisation is on resonance, the light converted into the other polarisation is consequently detuned from its own resonance which increases leakage.

Another important and apparent consequence of the cross-polarisation coupling is a reduction in the extinction ratio (ER) as summarised in Fig. 6.12(a), which plots P_T near resonance for τ_h from 0 to 40 m^{-1} whilst keeping the other coil parameters constant. Physically, this is equivalent to changing the coil diameter from $D = \infty$ to 0.2 mm while maintaining a constant dimensionless coupling parameter $K = \kappa S$, such that any change in resonance quality is attributed to a change in τ_h rather than deviation from critical coupling. The $\tau = 0$ case models an OMR in the planar limit, under which $\phi_B = 0$ and the ER is maximum. As τ_h increases, more light couples into A_y, which expends less time in the circulating coil than A_x and hence less light is absorbed. The overall ER of the OMR is limited by that of the y resonance, and Fig. 6.12(b) shows the ER can be reduced by up to 80%.

By the same mechanism, Fig. 6.12(b) shows that the Q-factor (defined as $Q = \Delta\lambda_{\mathrm{FWHM}}/\lambda$ where $\Delta\lambda_{\mathrm{FWHM}}$ is the full width at half maximum linewidth) falls by 32 %. This effect is clearly sensitive to both geometry and polarisation, since the aforementioned trends would be reversed were a y polarised input used, or if the pitch was chosen such that κ_x was closer to critical coupling than κ_y, in which case both the Q-factor and ER would increase with τ_h.

The choice of a 1 μm microfibre diameter in these simulations ensures a large evanescent field for the $\lambda = 1.55$ μm fundamental mode, so that the $\kappa_{x,y}$ remain high even for pitches several times wider than the microfibre. However, the exponential dependence of $\kappa_{x,y}$ on p would suggest that even small pitch variations can noticeably alter η, especially when κ is close to the critical coupling condition given by [23]:

$$\kappa_c = \sqrt{2}\frac{(m\pi \pm \sin^{-1}(1/\sqrt{3})}{S} \tag{6.14}$$

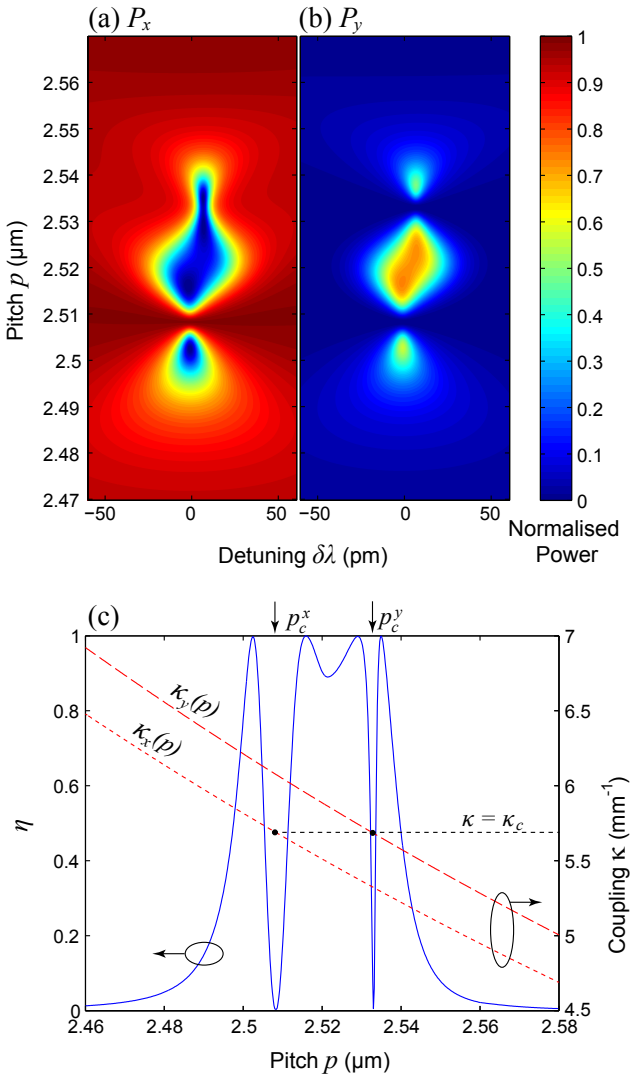

FIGURE 6.13: Output power against pitch in the (a) x polarisation and (b) y polarisation. (c) The fraction of output power in the y polarisation, η, and coupling coefficients as a function of pitch. Input is x polarised and other parameters same as Fig. 6.11.

which for $m = 1$ evaluates to $\kappa_c = 5686$ m^{-1}. Fig. 6.13 illustrates this for a range of pitches near 2.5 μm where $\kappa_{x,y}$ vary exponentially from 4500 to 6900 m^{-1}. When $\kappa \approx \kappa_c$, the value of η is close to 100%, but when far from critical coupling the resonance is too weak to observe the effects of Berry phase because negligible power is coupled into y polarisation. Interestingly, $\eta = 0$ when the coupling is precisely critical at $p = p_c^x$ and p_c^y – at these two points respectively, the x and y resonances are absent when solving the ODEs [29], because the light can be trapped indefinitely even for infinitely small input amplitude, which is a mathematically undefined scenario.

6.2.2.3 Summary

Although the generation of Berry's phase is weak in a microcoil, near resonance it can become greatly magnified by the repeated coupling of light back into the coil, providing

a significant exchange of power between the two states of polarisation which would otherwise propagate uncoupled. Along with the resonance extinction ratio and Q-factor, this behaviour is highly sensitive to the coil geometry, in particular the pitch and torsion, since the Berry's phase is innately topological. Decreasing the rod radius to increase τ_h and using a smaller core diameter in conjunction with a larger pitch would also maximise the generation of Berry's phase. Practically, with an appropriate pitch the effects of Berry's phase on the output of an OMR are sufficiently large to be observed experimentally.

6.3 Nonlinear polarisation dependent behaviour

Having presented a detailed linear model of the polarisation dependent properties of microcoils, we now extend the analysis by incorporating the third order nonlinearity of the silica to study the behaviour near resonances, where the amplified field strength inside the coil plays a crucial role in facilitating nonlinear effects. In previous literature [28, 30], OMRs were shown exhibit hysteresis when detuned from resonance, and given the findings from the previous section, in the birefringent case it is reasonable to expect the hysteresis characteristic and switching powers will be polarisation sensitive.

6.3.1 Theory

As before, the fibre is assumed to be both birefringent and slightly twisted, but the ODEs from Eqs. 6.1 are modified to account for a Kerr nonlinearity. To simplify the model, the coil diameter is assumed to be of the order of 1 mm or larger, so the helix torsion is low enough for Berry's phase effects to be excluded. In the j^{th} turn of the coil, the corresponding field amplitudes A_j^x and A_j^y are governed by the following equations:

$$\begin{aligned}\frac{dA_j^x}{ds} =& i\kappa_0\Big[A_{j-1}^x\cos(\theta^-) + A_{j-1}^y\sin(\theta^-) + A_{j+1}^x\cos(\theta^+) - A_{j+1}^y\sin(\theta^+)\Big] \\ &- i\alpha A_j^x + i\gamma(|A_j^x|^2 + \frac{2}{3}|A_j^y|^2)A_j^x + i\kappa_{xy}A_j^y\end{aligned} \tag{6.15a}$$

$$\begin{aligned}\frac{dA_j^y}{ds} =& i\kappa_0\Big[A_{j-1}^y\cos(\theta^-) - A_{j-1}^x\sin(\theta^-) + A_{j+1}^y\cos(\theta^+) + A_{j+1}^x\sin(\theta^+)\Big] \\ &- i\alpha A_j^y + i\gamma(|A_j^y|^2 + \frac{2}{3}|A_j^x|^2)A_j^y + i\kappa_{yx}A_j^x + i\Delta\beta A_j^y\end{aligned} \tag{6.15b}$$

Here, the loss term α is included in the ODEs because the amplitudes cannot simply be scaled down at the boundary conditions (as was done before) due to the presence of the nonlinear γ terms, which model the self and cross phase modulation [24]. Since the effective nonlinearity γ varies considerably with material and core size for diameters

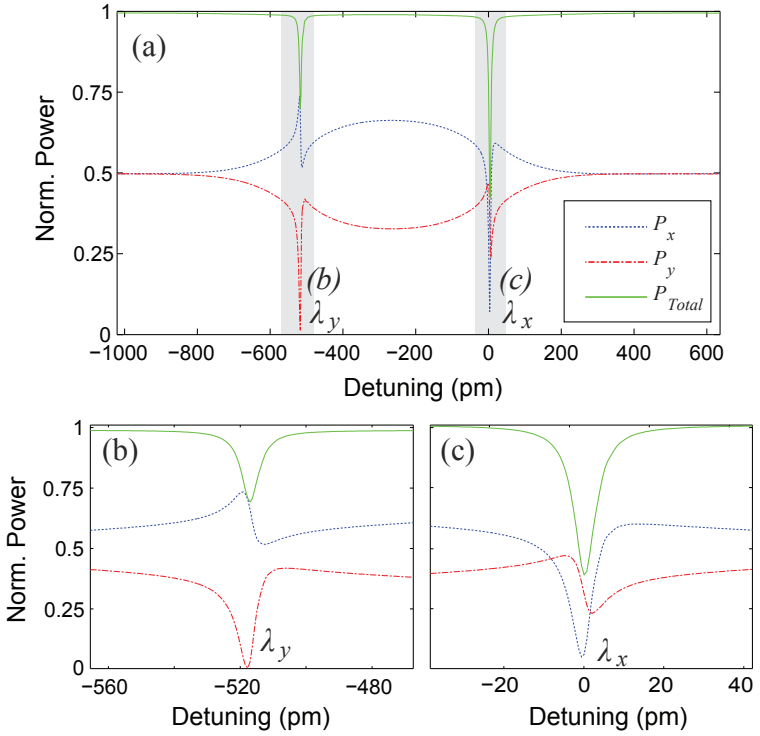

FIGURE 6.14: The linear spectrum of a microcoil based on twisted birefringent fibre (a) shown over one free spectral range. The shaded ranges are shown in close ups near (b) the y-resonance and (c) x-resonance. Coil parameters: $n = 3$ turns, $S = 1$ mm, $\kappa = 5370$ m^{-1}, $\alpha = 4.6$ m^{-1}, $B = 1 \times 10^{-3}$, twist torsion $\tau = 30$ rad m^{-1}, $|\mathbf{A}_{\text{in}}| = 1$ and input polarisation angle is $\pi/4$ rad.

around 1 μm (up to 0.1/W/m for an air clad silica microfibre at $\lambda = 1.55$ μm), in the simulations the amplitudes are normalised such that $\gamma = 1$ W^{-1}m^{-1}, or equivalently, $A \to A\gamma^{-0.5}$, so as to model the general case.

To study the hysteresis properties, these equations could be numerically solved by incrementing the input power and using the modified Newton method to find the output amplitudes A_{out}. However, when multiple solutions exist this will only converge to a single root which is usually closest to the initial start vector, leading to an incomplete set of solutions. For this reason, the technique used here involves incrementing the OMR stored energy E instead, since there is a many-to-one mapping between values of E and A_{out}, so the full hysteresis loop can be obtained as described in Appendix C.

6.3.2 Discussion

We shall first analyse a three turn microcoil with $\tau = 30$ rad m^{-1} and $B = 1 \times 10^{-3}$, whose linear spectrum is given in Fig. 6.14. The coupling of $\kappa_0 = 5370$ m^{-1} was chosen sufficiently close to the critical coupling ($\kappa_c = 5313$ m^{-1}) to offer sharp resonances and provides only one easily identifiable x or y resonance per free spectral range (FSR) to simplify our analysis.

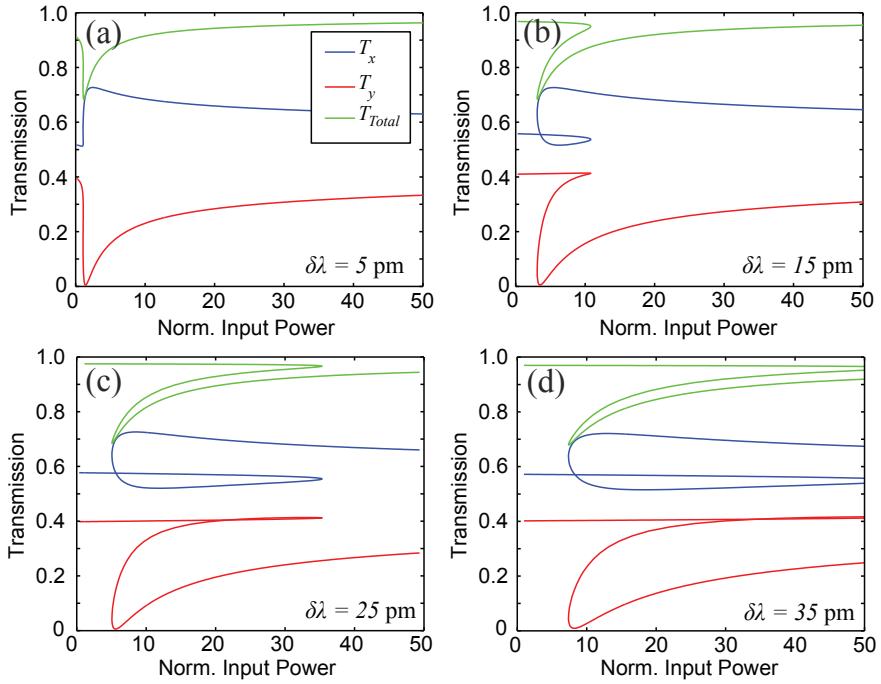

FIGURE 6.15: The nonlinear hysteresis characteristic when the wavelength is detuned from the $y-$resonance λ_y by (a) $\delta\lambda = 5$ pm, (b) 15 pm, (c) 25 pm and (d) 35 pm.Coil parameters same as Fig. 6.14.

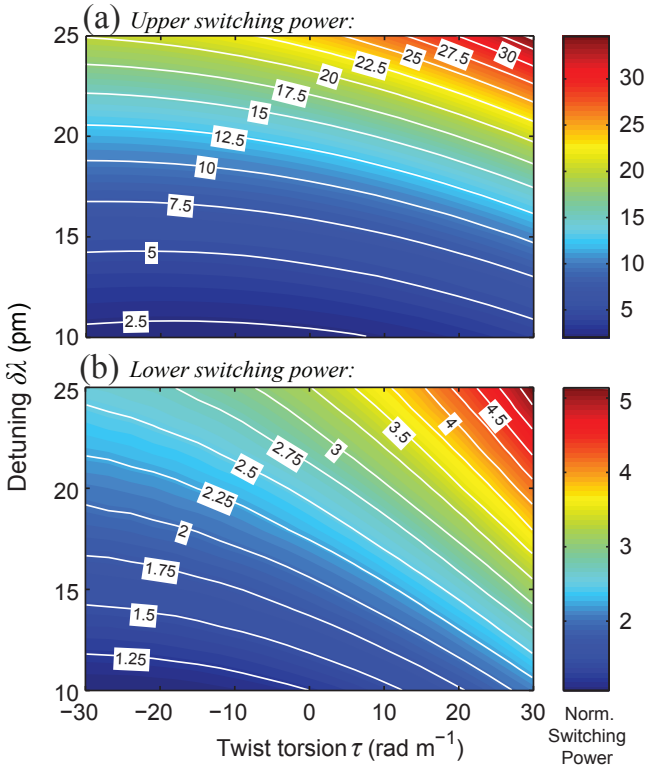

FIGURE 6.16: (a) The upper and (b) lower nonlinear switching powers for different twist τ and detuning $\delta\lambda$ values. Coil parameters same as Fig. 6.14.

From Fig. 6.14(a) it is clear that although the input is linearly polarised at $\pi/4$ rad, propagation through the coil has resulted in a net power transfer from $P_y \rightarrow P_x$ (for negative τ, the opposite holds true), for the reasons explained earlier in section 6.2.1. The effects are most obvious near the resonance wavelengths λ_y and λ_x as shown in Figs. 6.14(b) and (c), where the light becomes trapped and traverses a longer effective path length within the OMR, thus allowing a greater interaction length for the cross polarisation coupling. To study the nonlinear behaviour, we therefore focus on wavelengths slightly red-detuned from one of the resonances such that $\lambda = \lambda_{x,y} + \delta\lambda$, so the hysteresis will involve an interplay between the nonlinearity, twist and birefringence.

Firstly, the effect of detuning will be studied. Figure 6.15(a-d) plots the power hysteresis curve for detuning values of 5 pm $\leq \delta\lambda \leq$ 35 pm from λ_y for an OMR with the same parameters as that used in Fig. 6.14. The input power is normalised to be $P_{\text{in}} = |\mathbf{A}_{\text{in}}|^2$, and the transmissions are given by $T_{x,y} = P_{\text{out}}^{x,y}/P_{\text{in}}$ and $T_{\text{total}} = T_x + T_y$. When $\delta = 5$ pm, the detuning is similar to the linewidth of the resonance (9 pm at full-width half-maximum (FWHM)) and hence no hysteresis exists. Raising P_{in} to 2 will increase the nonlinear refractive index and nonlinear phase shift until the y-resonance condition is satisfied which consequently extinguishes the y-polarised output, after which any further increase in P_{in} will move the microcoil out of resonance. Note that these changes in T_x and T_y can be understood intuitively by comparison with Fig. 6.14(b); increasing the power from a low to high value is analogous to moving from the original detuned wavelength to a shorter wavelength in the direction of the resonance. For this reason, the x-polarised output is seen to sharply increase before falling gradually with P_{in}.

A more interesting response is seen when the detuning is greater as shown in Figs. 6.15(b-c) for $\delta\lambda = 15$ and 25 pm respectively. The transmission curves T_{total} show a bistability characteristic similar to the standard microcoil [30], with two stable levels connected by a third branch. As with ring resonators, the intermediate branch solutions are unstable and so cannot be observed in practice [104]; indeed, if one attempts to solve for these solutions by repeated Runge Kutta iterations (see Appendix section C.2, the amplitudes will only converge to either the upper or lower branch, even if the starting amplitudes were initially chosen to reside on a valid solution from the middle branch.

Resolving the transmission into its constituent x and y components confirms that the hysteresis is primarily due to the y-polarised light since the x-polarisation is off resonance. When P_{in} is decreased from an initially high value, the transmission follows the lower branch wherein the recirculation of y-polarised light keeps the microcoil in the low transmission state until the lower switching power P_{SL} is passed. The T_y contrast ratio of $\eta_y = 71.4$ measured at this lower switching point is independent of the detuning but instead corresponds to the linear resonance extinction ratio (ER) from Fig. 6.14(b). However, since the x-polarised light is coupled out, the overall output contrast is only $\eta_{\text{total}} = 1.4$.

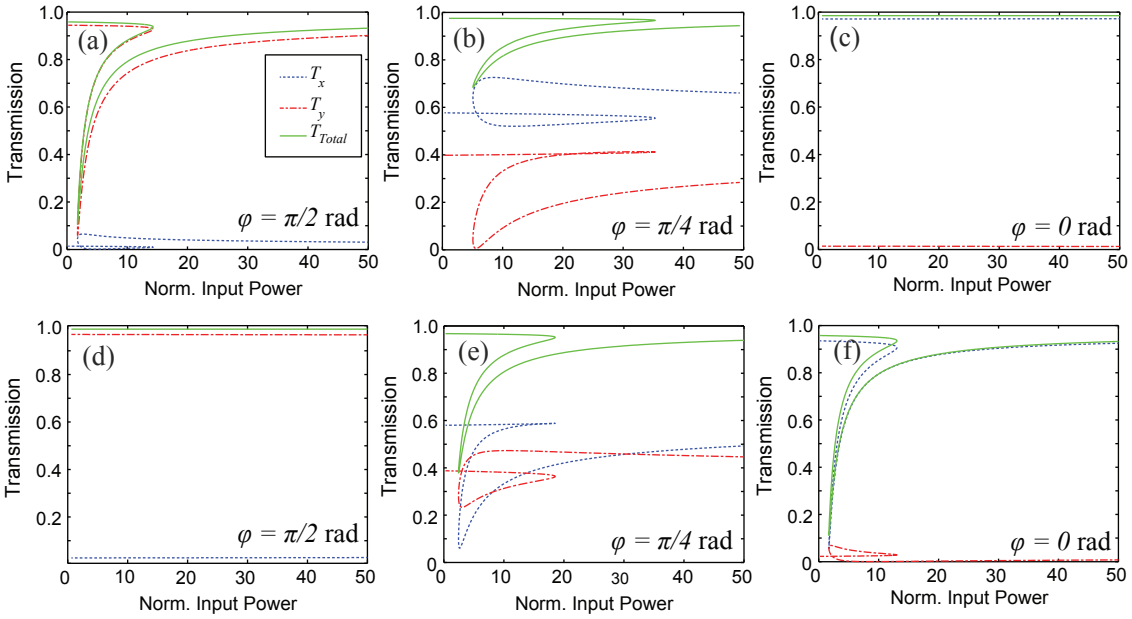

FIGURE 6.17: Nonlinear hysteresis characteristics for different input angles ϕ when detuned by $\delta = 25$ pm from (a-c) λ_y and (d-f) λ_x. Other parameters the same as Fig. 6.14.

For the largest detuning of $\delta = 35$ pm shown in Fig. 6.15(d), the wavelength is too far off resonance so the upper switching power P_{SU} exceeds the plotted range and hence the output would remain largely static unless a very large input $P_{\mathrm{in}} \geq 80$ is applied. Indeed, Fig. 6.16 confirms both that the lower and upper switching powers increase with $\delta\lambda$ as expected. From the same graph it is also evident that using a more positive τ (i.e. stronger twist) increases the switching powers, because more power is transferred into the off-resonance x-polarisation which quickly couples out of the coil and thus would not contribute significantly to any resonantly-enhanced nonlinear effects. Alternatively, if the wavelength had been detuned from λ_x the same mechanism would lead to a fall in P_{SU} and P_{SL}.

It should be noted that at high powers the solutions may not necessarily be stable in the time domain. Simulations modelling the full time propagation effects suggest that although the assumption of a steady-state solution is valid at low powers, increasing P_{in} may cause the output to become periodic or even chaotic [28] and so for these situations the temporary stability will be studied separately.

The hysteresis curve is also heavily dependent upon the input polarisation angle ϕ as summarised in Figs. 6.17 and 6.18. In particular, the contrast here varies with ϕ - for example, when detuned from λ_y with $\phi = \pi/2$ rad as in Fig. 6.17(a), the overall hysteresis characteristic T_{total} is predominantly determined by, and hence mirrors, that of T_y. The overall contrast is therefore high at $\eta_{\mathrm{total}} = 9.0$, although nonetheless lower than $\eta_y = 16.0$ due to the slight coupling into the non-resonant x-polarisation. At the

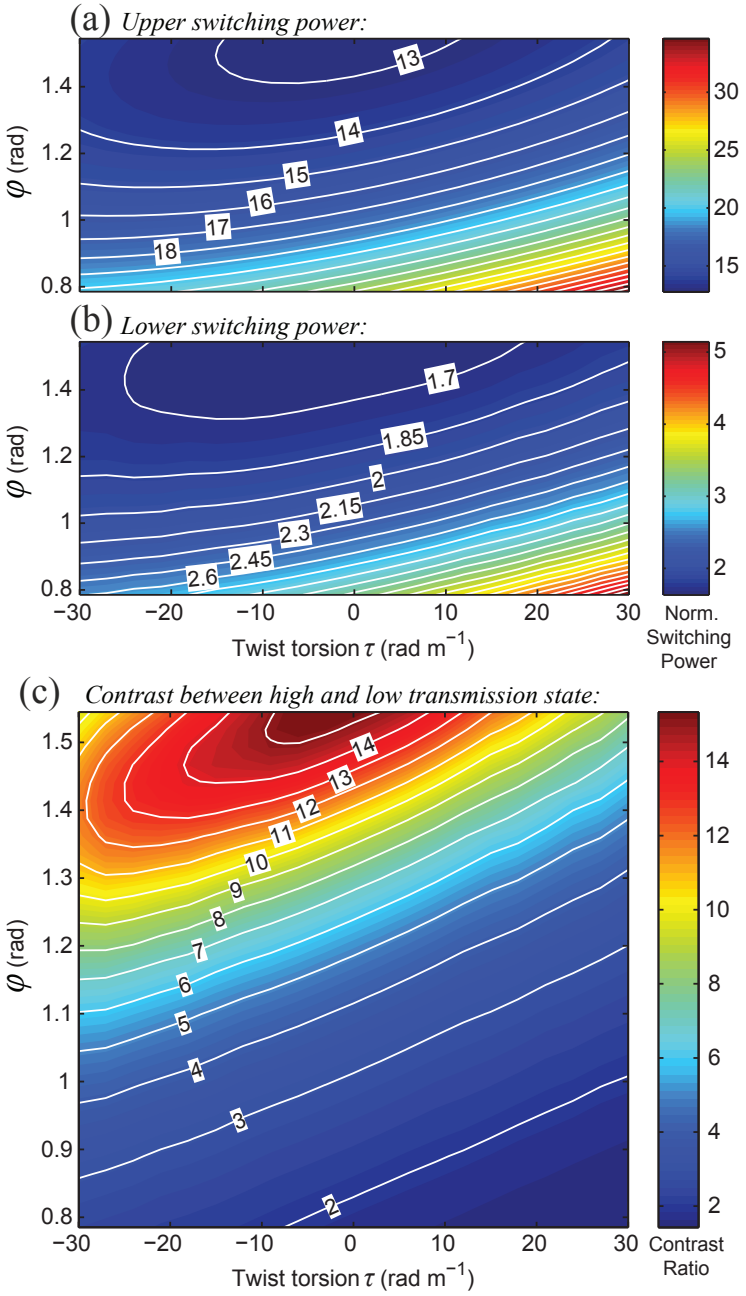

FIGURE 6.18: (a) The upper and (b) lower switching powers for different twist and input angle and (c) the corresponding contrast ratio at the lower switching point when detuned from λ_y. Other parameters the same as Fig. 6.14.

other extreme, if an x-polarised input is used, no hysteresis is observed since the amount of light coupled into the y-polarisation is too low to induce nonlinear switching.

It is also insightful to compare Figs. 6.17(b) and (e) which are detuned from λ_y and λ_x respectively but otherwise share the same simulation parameters. For the latter, the larger contrast η_{total} originates from its 28% higher linear ER (seen in Fig. 6.14(b-c)) whilst the higher switching powers are due to choice of twist which, as alluded to earlier, favours net coupling of power into A_x rather than A_y and consequently elongates the hysteresis loop.

This comparison highlights the importance of twist effects, which are analysed further in Figs. 6.18, where the switching powers and η_{total} are shown when the input angle is varied from $\pi/4$ rad (half x and half y-polarised) up to $\pi/2$ rad (purely y-polarised). The wavelength in both cases is detuned 25 pm from λ_y. When $\phi = \pi/4$, increasing τ from 0 to 30 rad m^{-1} will increase P_{SU} and P_{SL} as explained previously. This is also accompanied by a 2.7 dB reduction in the contrast to 1.4, due to the larger fraction of light being coupled out of the y-polarisation.

For $\phi \approx \pi/2$ rad however, both trends are no longer monotonic with τ but instead there exists a minimum switching power and maximum contrast level which occur at a certain value of torsion τ_c close to 0. This behaviour is best explained by considering the limit $\phi = \pi/2$ rad. If there is no twist ($\tau = \tau_c = 0$), all the power would remain y-polarised during propagation and hence remain stored in the coil at resonance, resulting in a strong overall extinction ratio and low switching powers. However, any deviation from $\tau_c = 0$ would couple light into the x polarisation and hence reduce the extinction ratio as well as increasing P_{SU} and P_{SL}. When ϕ is just below $\pi/2$, τ_c must be slightly offset negative so as to couple the small fraction of x-polarised light into the predominant and resonant y-polarisation.

Another unusual feature is observed at the other extreme in Fig. 6.17(f)when detuned from λ_x with $\phi \approx 0$. Here, the two polarisations can undergo nonlinear switching in the same direction - in particular, both T_x and T_y appear to switch down at P_{in} =14. In all the other cases analysed from Figs. 6.17 and 6.15, the nonlinear switching is always complementary in that if one polarisation switches up, its orthogonal counterpart will be forced to switch down and vice versa.

In the previous discussions, it has been assumed that the birefringence is large enough to separate the x and y resonances sufficiently such that the hysteresis will only depend on one of the resonances. However, for small birefringences, the separation becomes comparable to the resonance FWHM and so the nonlinear characteristics are affected by both polarisations' resonances. For the microcoil parameters in Fig. 6.14, this requires $B \approx 10^{-5}$. Alternatively, since the coupling is such that only one resonance exists per FSR, a similar situation arises if $B \approx m\lambda/S$ which effectively offsets the x and y-resonance spectra by a shift equal to m integer multiples of the FSR.

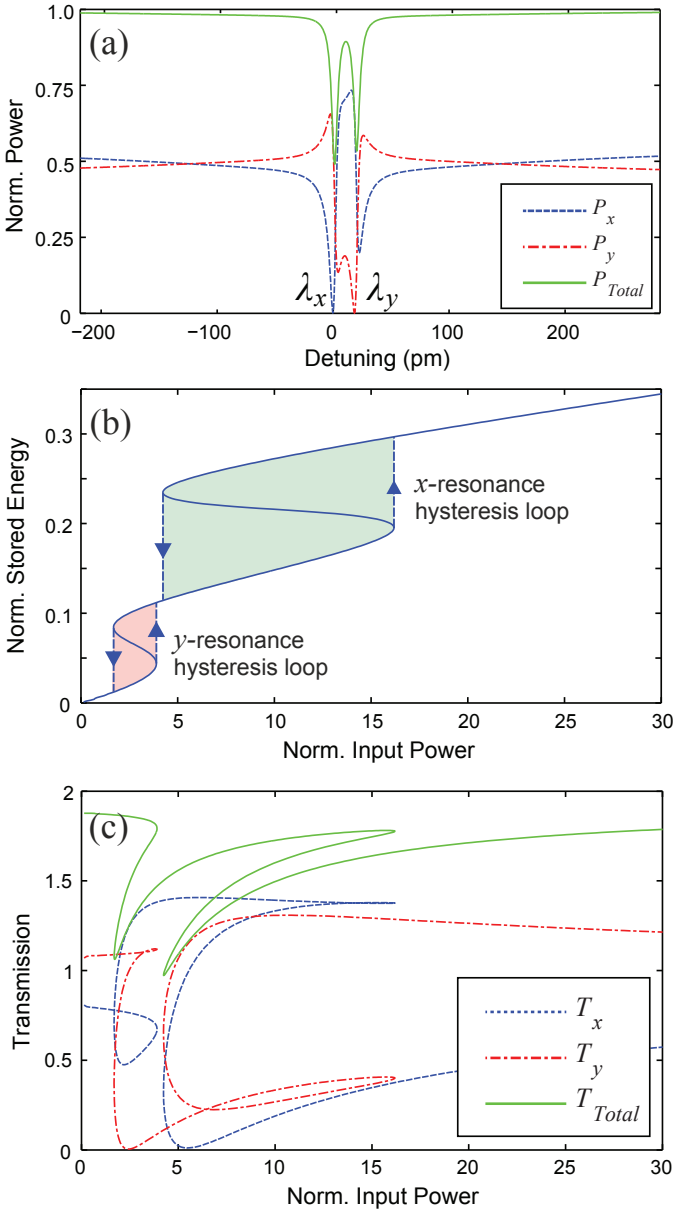

FIGURE 6.19: (a) Linear transmission spectrum for a coil with a weak birefringence of $B = 1 \times 10^{-5}$. (b) The energy stored in the OMR against the input power, showing the double nonlinear hysteresis loops when the input wavelength is red-detuned $\delta\lambda = 6$ pm from the y resonance λ_y. (c) The nonlinear transmission characteristic. Other parameters are the same as Fig. 6.14.

An example of this situation is illustrated in Fig. 6.19(a), which shows the linear output spectra for a coil with $B = 1 \times 10^{-5}$. Here, λ_x and λ_y are almost co-resonant with a separation of only 19 pm (note that due to twisting, this shift is slightly larger than the value of $\Delta\lambda = B\lambda/n$ expected when $\tau = 0$). When detuned by 6 pm from λ_y, plotting the stored energy against P_{in} reveals two hysteresis curves shown in Fig. 6.19(b) which correspond to each of the polarisations' resonances. Such a microcoil therefore exhibits multiple bistability similar to that reported in a birefringent Fabry-Perot cavity [105].

The dual bistability is also apparent from the nonlinear transmission characteristic in Fig. 6.19(c). Although somewhat more complex than those previously presented, it can nonetheless be resolved into the y and x-resonances' contributions, with T_y and T_x being extinguished at $P_{\text{in}} = 2.5$ and 5.2 respectively (due to the larger detuning for the latter). For this reason, the hysteresis curve resembles a combination of those shown in Figs. 6.17(b) and (e) but with slight disparities owing to their different linear transmission spectrum and detuning.

So far, the analysis has concentrated on $n = 3$ turn microcoils since these can be fabricated easily and consistently, whereas increasing the number of loops whilst maintaining a high uniformity becomes increasingly challenging and raises the overall loss without adding to the underlying physics. The nonlinear effects presented would nonetheless exist in OMRs with more turns, since their linear transmission is also polarisation dependent. However, their spectra are generally more complex, with each FSR containing several sets of resonances varying in extinction ratio and Q factor. The choice of resonance would thus significantly affect the switching powers and contrast, as would changing the proximity from critical coupling (which varies with n). This is illustrated in Fig. 6.20 which shows the spectrum for an $n = 5$ turn OMR along with the upper/lower switching powers associated with each resonance when detuned by 15 pm. Over one FSR, there are two sets of resonances ($\lambda^{(1)}$ and $\lambda^{(2)}$) each of which has its x and y resonances offset by birefringence. It is clear that the $\lambda^{(2)}$ resonances offer a higher ER and lower switching powers. Furthermore, the y resonances' switching powers are lower than those of the x resonances' (in contrast to the 3 turn case) - this is due to the larger number of turns increasing the path length such that the direction of net power transfer reverses to favour $P_x \rightarrow P_y$.

Similar polarisation dependencies would be expected for nonlinear bistability in other resonator architectures based on twisted/birefringent microfibre, for example in the loop resonator which is essentially a single turn microcoil, provided that the fibre is twisted at some point along the loop. However, due to the relatively short coupling region, either stronger twists or a higher Q-factor resonance would be needed to observe the same effects. The case of the knot resonator is more interesting since the intertwining of the microfibre at the coupling region will itself induce cross-polarisation coupling [86]. This inherent polarisation dependency would be present even when $\tau = 0$, but could

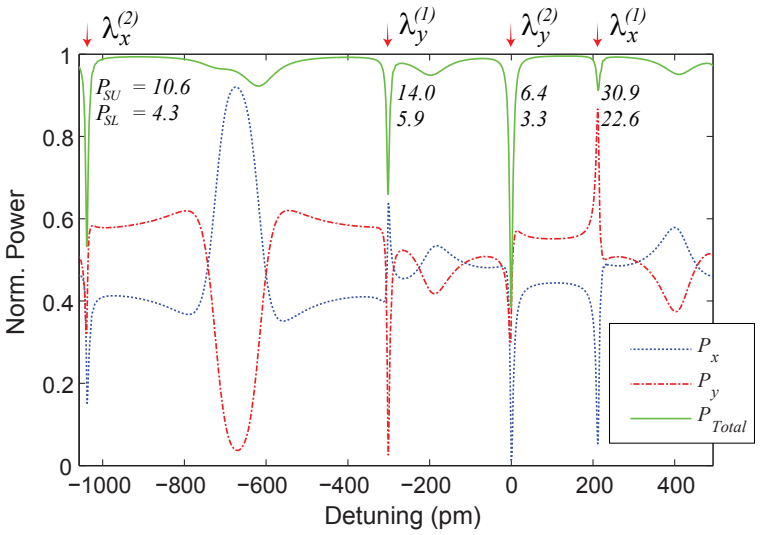

FIGURE 6.20: Linear transmission spectrum for an $n = 5$ turn microcoil, plotted over one FSR. The values indicate the upper and lower normalised switching powers P_{SU} and P_{SL} at each resonance when $\delta\beta = 15$ pm. $\kappa = 4200$ m^{-1} and other parameters are the same as Fig. 6.14.

be potentially increased or reduced by introducing a non-zero τ depending on the twist direction.

Finally, note that although the Berry's phase effects were excluded here since we are primarily interested in the effects of the fibre twist and birefringence, one could account for it by simply modifying the cross-polarisation coupling term in Eqn. 6.15, i. e. $i\kappa_{xy}A_j^y \rightarrow (i\kappa_{xy} + \tau_h)A_j^y$ (and similarly for κ_{yx}), where τ_h is the helix torsion defined earlier in Eqn. 6.8. The consequences would be somewhat similar to using a stronger or weaker twist, but would only be apparent near resonance.

6.3.3 Potential applications in signal processing

The nonlinear properties of the standard microcoil may be utilised for a variety of signal processing applications such as switching, boolean logic and memory, and in the twisted and birefringent microcoil, these can be expanded to offer polarisation dependent features. It is straightforward, for example, to adapt Fig. 6.15(a) into a Boolean NOT gate in which the logical input and output are designated by P_{in}^y and T_y respectively.

Although the Kerr effect itself is quasi-instaneous, the processing speed of such devices would be limited by the transit time of the signal pulse through the coil. This introduces a trade-off between the required threshold powers and signal bandwidth, since a higher Q resonance would offer lower switching powers, but also store a pulse for a longer duration. On the other hand, it is worth noting that a large delay would be attractive for all-optical delay line applications.

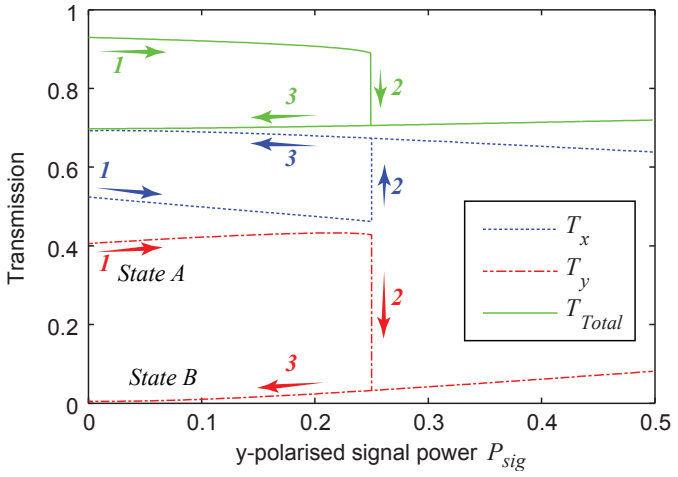

FIGURE 6.21: Simple memory latch operation using an OMR. At the input is a bias of $A_x = A_y = 1$ along with a y-polarised signal P_{sig} which is varied between 0 to 0.5. Detuning is 8 pm from λ_y and other parameters are the same as Fig. 6.14.

For memory devices, the OMR bistability can be employed, and Fig. 6.21 illustrates the use of hysteresis (from a coil similar to that discussed earlier for Fig. 6.15) as a basic memory unit. In this scheme, the input to the microcoil consists of two parts: P_{bias}, a constant which biases the microcoil onto the bistable region, and P_{sig}, which is the signal used to switch the power between the two stable states. The output is given by T_y with the high and low transmission states denoting two logical states A and B. When detuned 8 pm from the y-resonance the switching powers are low so only a weak bias amplitude of $A_x = A_y = 1$ is needed, and with $P_{\text{sig}} = 0$ the microcoil is initially in the high transmission state A at (1) with $T_y = 0.4$. If P_{sig} is then increased above $P_{\text{SU}} = 0.25$, the nonlinear switching at (2) toggles the microcoil into state B. When the signal power is returned to 0 again however, the microcoil remains latched in the same state

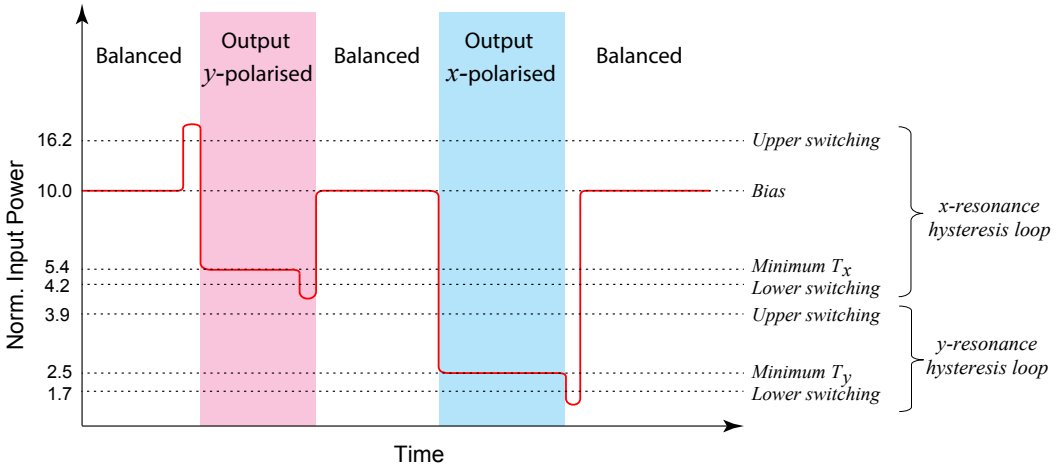

FIGURE 6.22: Possible use of dual hysteresis in a microcoil for nonlinear polarisation switching, whereby varying the P_{in} will change the output power to either the x, y, or both polarisations. The values of P_{in} ($\phi = \pi/4$ rad) on the y-axis correspond to those from Fig. 6.19 (not to scale). Coil parameters are the same as Fig. 6.19.

(3) until P_{bias} is temporarily reset low. The transmission contrast between the on-off states when $P_{\text{sig}} = 0$ is approximately 19 dB and hence the binary state can be clearly distinguished.

Crucially, the previous two devices are only sensitive to a y-polarised signal; using an x-polarised signal would not trigger switching and only a minor change in transmission would be detected. On the other hand, for certain situations it is desirable to interact with both polarisations - for example, the output of a polarisation switcher must be capable of alternating between either polarisation state. Such a device can be realised using the dual-bistable nature of Fig. 6.19(c) by noting that there exist two points where either T_x or T_y is extinguished, which can be reached by only changing P_{in}. Figure 6.22 illustrates one possibility where the microcoil is initially biased with $P_{\text{in}} = 10$, which ensures the microcoil state begins on the middle branch between the two hysteresis loops and furthermore provides an approximately balanced neutral output with $T_x/T_y = 1.07$ (the input power is equally distributed between the x and y polarisations). If P_{in} is increased above P_{SU} of the x-hysteresis loop and then lowered again, the microcoil will now operate on the lower transmission branch, and at $P_{\text{in}} = 5.4$ the output is almost entirely y-polarised with $T_y/T_x = 20.6$ dB. P_{in} can then either be reverted to the bias state or, alternatively, further reduced to enter the y-hysteresis loop's low transmission branch. At $P_{\text{in}} = 2.5$ the output is now largely x-polarised as $T_x/T_y = 24.0$ dB.

In addition to switching between polarisations, this OMR could also be used as a spatial switch if the output were coupled to a polarising beam splitter or similar device. Overall, the strength of nonlinear microcoils for such applications lies in the wide range of parameters which can be configured to adjust both the linear and nonlinear characteristics.

6.3.4 Summary

Cross polarisation coupling in birefringent and twisted fibre OMRs plays a crucial role in determining the nonlinear hysteresis characteristics. The switching power and bistability contrast, in particular, are highly dependent on the input polarisation angle and choice of x or y resonance.

Near a resonance, the input/ouput power transfer characteristic shows significant changes in both polarisations' output power which are to some extent dictated by the linear resonance spectrum - for example, the contrast is largely determined by the extinction ratio of the microcoil resonance. However, the nonlinear switching is predominantly driven by the recirculation of only the resonant polarisation, not the orthogonal (off-resonance) polarisation which is quickly coupled out. For this reason, by adjusting the twist and input polarisation angle, one may tailor both the upper and lower switching powers. For

weak birefringences ($B \approx 10^{-5}$), the x and y resonances are spectrally close enough for a red detuned wavelength to interact with both and thus experience multiple bistability.

Finally, we have shown that the hysteresis of the microcoil can be used as the basis for performing polarisation sensitive Boolean logic operations and rudimentary memory buffering, which might be realised in practice using powers down to tens of watts for silica coils.

6.4 Conclusion

Accounting for the polarisation dependent coupling mechanics between the x and y modes in microcoils reveals interesting behaviour in both the linear and nonlinear regimes. Even when the microfibre is only mildly twisted or birefringent, the transmission and resonance spectrum can be significantly altered which would be detectable as a change in the extinction ratio or Q-factor. We have also studied the magnification of the Berry phase in microcoils. In this case the OMR microfibre need not be twisted nor birefringent, but if the microcoil diameter is sufficiently narrow ($\sim$0.1 mm), the accumulated Berry's phase on resonance can be great enough to rotate the input polarisation considerably.

The anisotropy between the two polarisations' transmissions is also manifested in the nonlinear bistability and switching characteristics with different polarised inputs. Of particular interest is the ability to adjust the hysteresis loop shape by altering the twist and birefringence, since the nonlinear OMRs can potentially be used for nonlinear signal processing, such as performing Boolean logic on inputs represented by different polarisations.

Importantly, the predicted polarisation effects are sufficiently large that an experimental verification should be realistically possible using microcoils with parameters similar to those reported in literature, which can be fabricated using current technology. For the nonlinear case, the hysteresis should be observable with relatively low powers ranging between 10 to 100 W, which can be easily achieved with pulsed sources.

Chapter 7

Conclusions

7.1 Summary

In this thesis, we have shown how microfibres and their resonators exhibit a range of intriguing nonlinear phenomena which include intermodally phase matched third and second harmonic generation, as well as hysteresis and bistability in resonator architectures.

For third harmonic generation in uniform taper waists, we have obtained efficiencies up to $\eta = 3 \times 10^{-3}$ over 4 mm, an order of magnitude greater than currently reported in literature [15] despite pumping with a ten-fold lower peak power of 1.2 kW at a 1.55 μm wavelength. A more interesting situation arises when THG occurs instead in transition regions which have been purposely extended over several cm, so as to offer a considerably wider bandwidth than bulk or uniform waveguides, and using such tapers we have demonstrated a 5 dB bandwidth in excess of 36 nm.

Furthermore, reconfiguring tapers into loop resonators successfully improved the experimental efficiency of THG interactions by 7.7 dB greater than that of the original straight microfibre, with simulations suggesting that higher enhancements of 20 dB would be realistically achievable were the resonator closer to critical coupling. Importantly, a significant conversion of several percent is attainable using pump powers as low as 100 W and short loop lengths of several mm. This conversion can be increased further by coresonance of the harmonic and pump, such that the recirculated harmonic light acts as a seed for the incoming pump.

The second harmonic generation in microfibres was studied both theoretically and experimentally. Simulations show that over a 5 cm uniform microfibre, the efficiency can potentially reach several percent, but may be orders of magnitude lower in practice due to fabrication tolerances. We have therefore investigated resonant SHG in loop resonators as a means of overcoming this limit. To demonstrate the enhancement, the

efficiency of $\eta = 4.2 \times 10^{-8}$ in a straight taper (recorded with a peak pump power of 100 W and 200 μm interaction length) was found to increase by 7.6 dB when the taper was rearranged into a loop resonator.

We have also modelled the nonlinear response of microcoils based on twisted birefringent microfibres by incorporating a Kerr nonlinearity. Even in the linear regime, the OMR transmission varies strongly with twist which couples the two orthogonal polarisations in the microfibre to either enhance or dampen the resonance quality factor and extinction ratio. It is interesting to note that for narrower diameter microcoils, such effects can arise even without any twisting or birefringence, due to the polarisation rotation incurred when the generation of Berry's phase is magnified on resonance.

Likewise, the nonlinear hysteresis characteristics were found to be highly polarisation dependent, with both the switching powers and bistability contrast strongly influenced by the twist as well as the input polarisation angle. In addition, multiple bistability in OMRs can occur when the two orthogonal polarisations' resonances are spectrally close enough to influence the propagation of a slightly red detuned pump.

7.2 Outlook

A number of promising projects could explore and extend the currently presented work further.

One method to increase the third harmonic generation efficiency would be to use tapers pulled from soft glasses like tellurites or lead silicate. The effective nonlinearity γ of such tapers not only benefits from their larger nonlinear coefficients $n^{(2)}$ than silica, but also their higher linear refractive indices which allow tighter modal confinement. For example, the nonlinearity of chalcogenide microfibres can reach up to $\gamma = 90$ W^{-1}m^{-1} [49], two orders of magnitude greater than for silica microfibres. Indeed, both tellurite and chalcogenide microfibres were recently studied and proposed for harmonic generation [18].

The use of transition regions for broadband third harmonic generation also raises a compelling possibility – if the initial pump pulse is chirped, the different frequency components will be converted to their harmonic wavelength at different points in time and space. By designing an appropriate taper diameter gradient and pulse chirp, it should therefore be possible to simultaneously compress and frequency triple the pulse over the transition region. To model such an experiment would also require modifying the THG equations from Eqn. 3.7 to incorporate the time dependency of the amplitudes and dispersive terms.

It is worth noting that the same intermodal phase matching for THG may be adopted for the inverse process of one-third harmonic generation (OTHG), either for photon-triplet

generation to produce entangled photons, or for parametric downconversion [70, 106, 107]. The first process would be low in efficiency since the photons grow from quantum fluctuation noise, but nonetheless would be of interest for applications in quantum information processing and communication experiments. On the other hand, the parametric process, which uses essentially the same classical physics as THG, would be able to provide gain for a seed at the longer wavelength. Although parametric amplifiers already exist, they tend to generate longer wavelengths by converting two pump photons into a shorter wavelength signal and longer wavelength idler photon, whereas OTHG directly downconverts one pump photon to three idlers, thus providing a six-fold higher quantum efficiency. If implemented using tapers based on soft glasses with transparency windows extending far into the IR, such as chalcogenide, these OTHG processes would be particularly useful for generating or amplifying signals at wavelengths of several microns.

For second harmonic generation, the use of surface coatings based on molecules with a large electric dipole to increase the microfibre surface $\chi^{(2)}$ and efficiency is especially attractive if a high surface quality and uniformity of the coating can be maintained, possibly via a self-assembly process. In the case of resonantly enhanced harmonic generation, we expect that the efficiency can be increased up to 20 dB by refining or automating the loop manufacturing technique, for example by implementing a computer-controlled system to improve tolerance and control over loop geometry.

The work on microcoils in this thesis has been restricted to theoretical modelling, but in terms of experiments, it would be reasonably straightforward to first verify the predicted linear polarisation dependent properties by fabricating microcoils from elliptical birefringent microfibres [91, 92]. Observation of the nonlinear switching however requires a more careful experimental design. Whilst low peak pump powers of 100 W are sufficient, the repetition rate should ideally exceed 10 kHz in order to average out the slower thermal nonlinearities [69]. The use of long nanosecond pulses, measured on an oscilloscope before and after the microcoil, would allow easier identification of nonlinear switching points in order to eventually reconstruct the hysteresis characteristic.

Ultimately, these OMRs may be implemented as polarisation-sensitive devices in areas such as signal processing, whilst the harmonic generation processes could be exploited as a low cost means to provide wavelengths in ranges unavailable from standard sources. With a growing interest in microfibres from institutes around the world, it is envisaged that the research community will continue to offer novel insights into their optical properties and develop innovative applications over the coming years.

Appendix A

High Power 1.55 μm Pump Source

For the third and second harmonic generation experiments in Chapters 3-5, a tunable 1.55 μm wavelength pulsed source was constructed to use as a high power pump. The source was built using several components kindly loaned from Christophe A. Codemard (SPI Lasers, UK), who also provided useful advice on the design. Fig. A.1 shows the

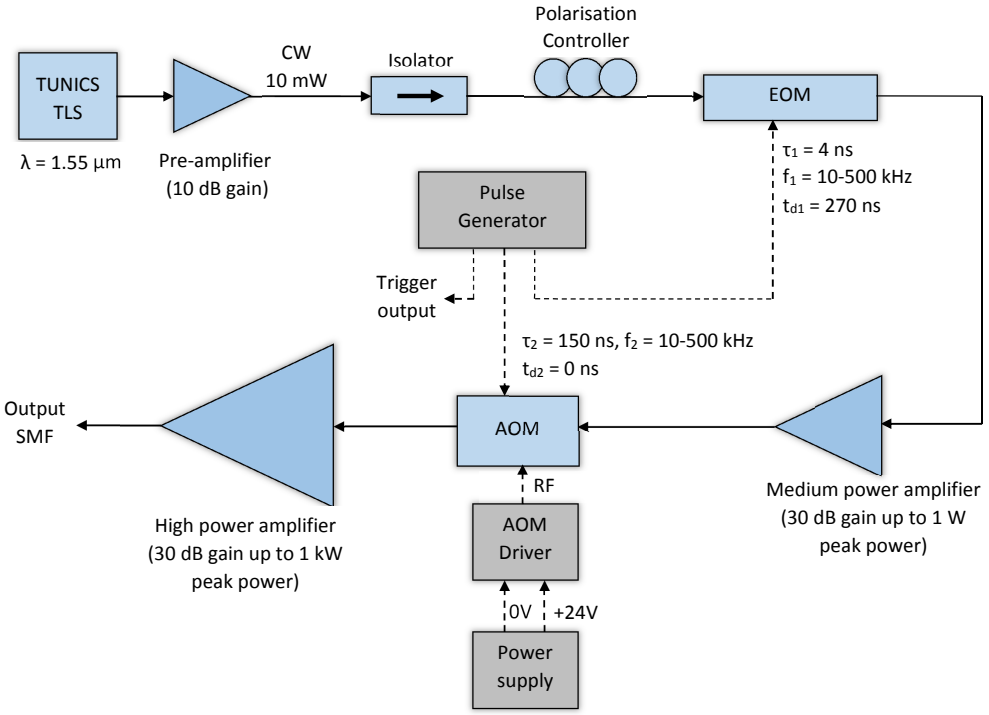

FIGURE A.1: Schematic of the 1.55 μm tunable wavelength source, used as the pump for the third and second harmonic generation experiments.

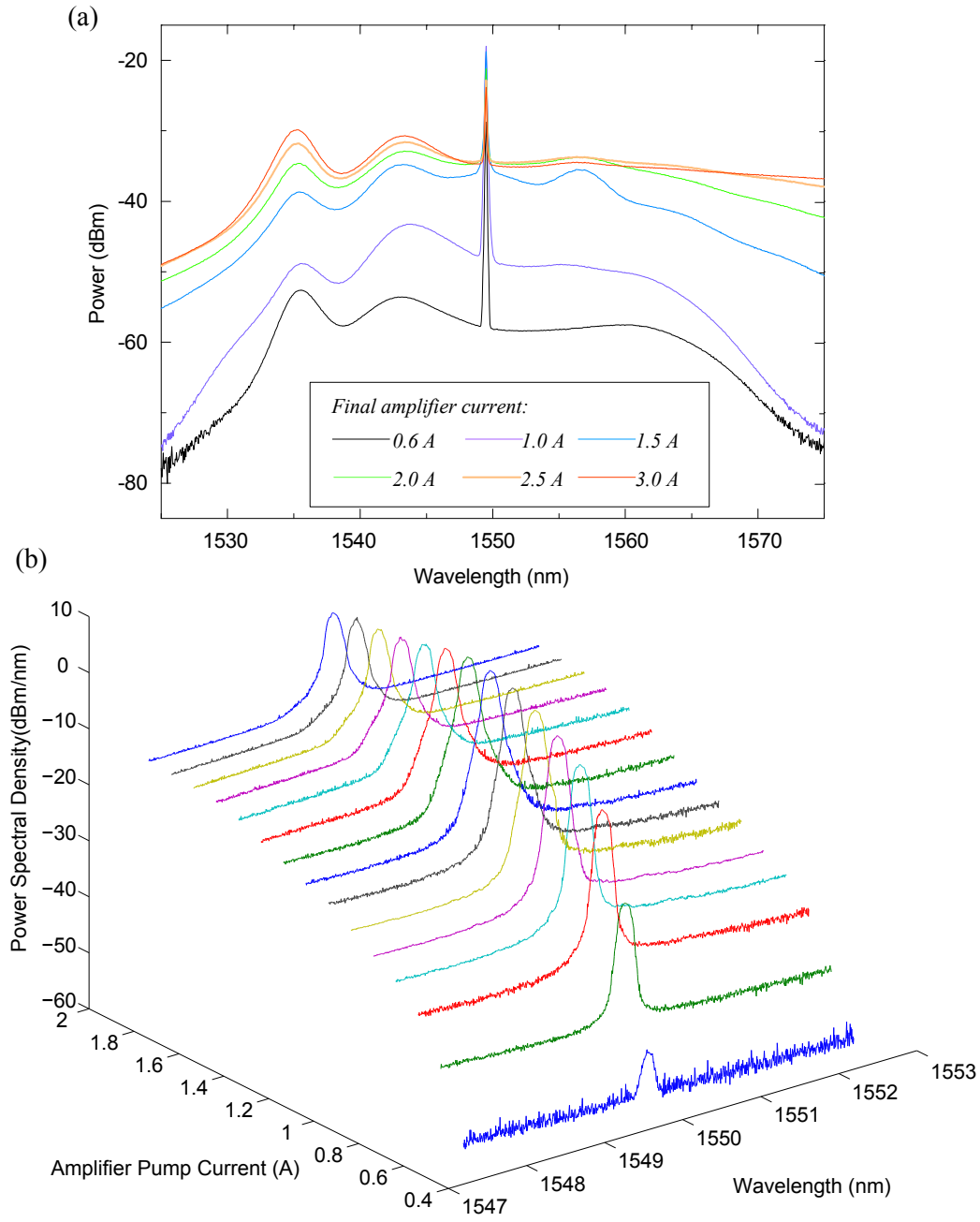

FIGURE A.2: (a) The output pump power spectrum and (b) a close up of the 1.55 μm pump peak power spectral density spectra and ASE level at different amplifier currents. Spectra were measured through a coupler with -25 dB attenuation. The highest current corresponds to a peak power of 1.3 kW.

schematic of the source, which follows a master-oscillator power-amplifier (MOPA) arrangement.

First, the seed light from the a tunable laser source (TLS) (Photonetics TUNICS-PR-1550) is pre-amplified with a 10 dB gain erbium doped fibre amplifier (EDFA) and passed through a $\tau_1 = 4$ ns electro optic modulator (EOM) to produce the seed pulse. The EOM is driven directly using the TTL output from a pulse generator, at a repetition rate

which can be adjusted between $f_1 = 10$ kHz up to 0.5 MHz. A polarisation controller before the EOM is necessary to maximise the output since the transmission of the electro optic media is polarisation dependent.

Since the pulse energy is only circa 10 mW, a second, medium power amplifier (Amonics C-band EDFA) is used to boost the peak power by 30 dB to roughly 1 W. The ASE from the EDFA introduces a background CW noise, which is subsequently removed by the acousto-optic modulator (AOM) driven using the same pulse generator and frequency $f_2 = f_1$, such that only the pulse can pass through the $\tau_2 = 150$ ns AOM window. Note that a small delay of $t_d = 270$ ns is required in between generating the EOM and AOM electrical pulses, to account for the pulse propagation time along the adjoining fibre.

Finally, the pulse is passed through a high power amplifier which was made by reconfiguring an old erbium doped fibre laser. The final gain exceeds 30 dB, which gives peak powers up to 1.3 kW at an amplifier pump current of 2 A (although the current can be increased further, the signal-to-noise ratio falls since the gain observed by the pulse begins to saturate whilst the background ASE continues to rise, which is undesirable).

The maximum average output power at an amplifier current of 2 A is 0.6 W, of which the 1.55 μm peak accounts for 0.5 W at a repetition rate of 100 kHz. If a weaker pulse power is used, the repetition rate can be increased up to 500 kHz to maintain a high signal to noise ratio (typically, in experiments we use $f = 100$ kHz for 1 kW peak powers, whilst 200 kHz or above can be used if only ~ 100 W peak powers are needed.

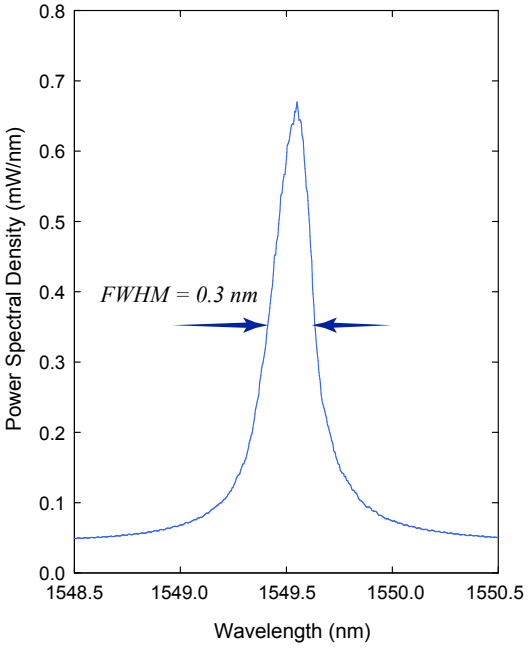

FIGURE A.3: Close up of the pump peak at a current of $I = 1.5$ A, measured through a -30 dB coupler. The pump peak power is 1 kW.

The output spectrum of the source shown in Fig. A.2 indicates the peak is roughly 100 times greater than the background ASE level. As the current approaches 2.0 A, the average power continues to increase roughly linearly with current due to the increase in ASE, but the power in the 4 ns pulse begins to plateau and the 1.55 μm peak experiences spectral broadening. For a 1 kW peak pulse power, the FWHM spectral width is typically 0.1 nm after leaving the source but broadens to 0.3 nm after 2 m of SMF patch-cord as illustrated in Fig. A.3. Using a much lower peak power of 100 W, the SPM is much weaker and so the FWHM is maintained at 50 pm even after several metres of SMF.

Appendix B

Third Harmonic Generation Equations

This appendix supplements Chapter 3 by outlining the derivation details for the third harmonic differential equations, which incorporate the vectorial nature of the fields. In addition, section B.2 determines which of the harmonic modes have a zero or non-zero overlap with the pump mode.

B.1 Derivation of differential equations

The calculation is based on the conjugated Lorentz reciprocity theorem, which relates two sets of fields $\{\widetilde{\mathbf{E}}_0(\mathbf{r},\omega_0),\widetilde{\mathbf{H}}_0(\mathbf{r},\omega_0)\}$ and $\{\widetilde{\mathbf{E}}^*(\mathbf{r},\omega),\widetilde{\mathbf{H}}^*(\mathbf{r},\omega)\}$. These can represent any two electromagnetic fields (provided they satisfy Maxwell's equations in their unconjugated and conjugated form respectively) which allows the theorem to be applied in diverse situations such as proof of modal orthogonality [31], difference-frequency generation [108] and nonlinear propagation in waveguides [19].

Here, we use $\{\widetilde{\mathbf{E}}_0,\widetilde{\mathbf{H}}_0\}$ to represent an unperturbed field propagating in the waveguide without nonlinearity with $\widetilde{\mathbf{P}}_{0,\mathrm{NL}}=0$, and $\{\widetilde{\mathbf{E}},\widetilde{\mathbf{H}}\}$ will represent its perturbed equivalent due to a nonlinearity introduced by a non-zero $\widetilde{\mathbf{P}}_{\mathrm{NL}}$. The theorem is applied firstly for the pump, i. e. where the unperturbed and perturbed fields model the pump, and then again for the harmonic. In this way, we can determine the propagation of the amplitudes for the perturbed pump and harmonic fields based on the interaction of the original unperturbed field with the nonlinear polarisation. We adopt a similar procedure and notation to that used in [19, 108], albeit modified to focus on third harmonic generation. The reciprocity method was also used by Grubsky et al. to obtain their differential equations for THG in reference [17], although the derivation details were largely omitted.

The theorem of reciprocity is given by:

$$\frac{\partial}{\partial z}\iint_{\infty}\mathbf{F}\cdot\hat{\mathbf{z}}dA=\iint_{\infty}\nabla\cdot\mathbf{F}dA \tag{B.1}$$

where the vector function $\mathbf{F}$ links the perturbed and unperturbed fields as follows:

$$\mathbf{F}=\tilde{\mathbf{E}}_0\times\tilde{\mathbf{H}}^*+\tilde{\mathbf{E}}^*\times\tilde{\mathbf{H}}_0 \tag{B.2}$$

The integrals are evaluated over the infinite transverse cross section of the waveguide. We first analyse the LHS of Eqn. B.1. For a microfibre, the unperturbed field will be one of the guided modes (mode ν) and in the frequency domain takes the form:

$$\widetilde{\mathbf{E}}_0(\mathbf{r},\omega_0)=\mathbf{E}_\nu(\mathbf{r}_\perp,\omega)e^{i\beta_\nu z} \tag{B.3a}$$

$$\widetilde{\mathbf{H}}_0(\mathbf{r},\omega_0)=\mathbf{H}_\nu(\mathbf{r}_\perp,\omega)e^{i\beta_\nu z} \tag{B.3b}$$

Here, the tilded notation $\widetilde{\mathbf{E}}_0(\mathbf{r},\omega_0)$ indicates that the field includes the fast oscillating phase term, whereas the untilded field $\mathbf{E}_\nu(\mathbf{r}_\perp,\omega)$ describes the modal field distribution at the given frequency. For example, if $\widetilde{\mathbf{E}}_0(\mathbf{r},\omega)$ represents the harmonic, then $\mathbf{E}_\nu(\mathbf{r}_\perp)$ might be the HE_{12} mode with $\omega_0=\omega_3$. On the other hand, the perturbed field must be expanded as a sum of all possible original unperturbed modes at that frequency since the perturbation may, in the general case, lead to the excitation of other modes:

$$\widetilde{\mathbf{E}}(\mathbf{r},\omega)=\sum_\mu A_\mu(z,\omega)\mathbf{E}_\mu(\mathbf{r}_\perp,\omega_0)e^{i\beta_\mu z} \tag{B.4a}$$

$$\widetilde{\mathbf{H}}(\mathbf{r},\omega)=\sum_\mu A_\mu(z,\omega)\mathbf{H}_\mu(\mathbf{r}_\perp,\omega_0)e^{i\beta_\mu z} \tag{B.4b}$$

where any frequency dependency is implicitly included in the amplitudes $A_\mu(z,\omega)$, and the mode distributions are each power normalised:

$$\frac{1}{4}\int_{A_\infty}(\mathbf{E}_\mu\times\mathbf{H}_\mu^*+\mathbf{E}_\mu^*\times\mathbf{H}_\mu).\hat{\mathbf{z}}\,dA=1 \tag{B.5}$$

Importantly, the modes are mutually orthogonal such that $\iint_\infty\mathbf{E}_\mu\times\mathbf{H}_\nu^*dA=0$ for $\mu\neq\nu$. Substituting Eqns. B.3, B.4 into the LHS of Eqn. B.1, and then applying Eqn. B.5 and the orthogonality relation gives:

$$\begin{aligned}\frac{\partial}{\partial z}\iint_{\infty}\mathbf{F}\cdot\hat{\mathbf{z}}dA&=\frac{\partial}{\partial z}\left[\sum_\mu A_\mu^*(z)e^{i(\beta_\nu-\beta_\mu)}\iint_\infty\left(\mathbf{E}_\nu\times\mathbf{H}_\mu^*+\mathbf{E}_\nu^*\times\mathbf{H}_\mu\right)\cdot\hat{\mathbf{z}}dA\right]\\&=4\frac{\partial}{\partial z}A_\nu^*(z,\omega)\end{aligned} \tag{B.6}$$

Next, we analyse the RHS of Eqn. B.1 by expanding the divergence term. Transforming Maxwell's equations into the Fourier domain conveniently simplifies the time differential

terms ($\partial t \to -i\omega$) to give:

$$\nabla \times \widetilde{\mathbf{E}}(\mathbf{r},\omega) = i\omega\mu_0\widetilde{\mathbf{H}}(\mathbf{r},\omega) \tag{B.7a}$$

$$\nabla \times \widetilde{\mathbf{H}}(\mathbf{r},\omega) = -i\omega\epsilon_0\widetilde{\mathbf{E}}(\mathbf{r},\omega) - i\omega\widetilde{\mathbf{P}}(\mathbf{r},\omega) \tag{B.7b}$$

Since the polarisation can be represented as $\widetilde{\mathbf{P}}(\mathbf{r},\omega) = \epsilon_0\chi^{(1)}\widetilde{\mathbf{E}}(\mathbf{r},\omega) + \widetilde{\mathbf{P}}_{\mathrm{NL}}(\mathbf{r},\omega)$, and $(1+\chi^{(2)}) = \epsilon_r = n^2$, Eqn. B.7b can be rewritten as:

$$\nabla \times \widetilde{\mathbf{H}}(\mathbf{r},\omega) = -i\omega\epsilon_0 n^2(\mathbf{r},\omega)\widetilde{\mathbf{E}}(\mathbf{r},\omega) - i\omega\widetilde{\mathbf{P}}_{\mathrm{NL}}(\mathbf{r},\omega) \tag{B.8}$$

Substituting the perturbed and unperturbed equivalents of Eqns. B.7a and B.8 into the integrand on the right hand side (RHS) of Eqn. B.1 and applying the vector calculus identity $\nabla.(\mathbf{A}\times\mathbf{B}) = \mathbf{B}.(\nabla\times\mathbf{A}) - \mathbf{A}.(\nabla\times\mathbf{B})$ gives:

$$\begin{aligned}\nabla\cdot\mathbf{F} = &- i\mu_0(\omega-\omega_0)\tilde{\mathbf{H}}\cdot\tilde{\mathbf{H}}_0 \\ &- i\epsilon_0\left[\omega n^2(\mathbf{r},\omega) - \omega_0 n^2(\mathbf{r},\omega_0)\right]\tilde{\mathbf{E}}^*\cdot\tilde{\mathbf{E}}_0 \\ &- (i\omega\tilde{\mathbf{E}}_0^*\cdot\tilde{\mathbf{P}}_{\mathrm{NL}} - i\omega_0\tilde{\mathbf{E}}\cdot\tilde{\mathbf{P}}_{0,\mathrm{NL}}^*)\end{aligned} \tag{B.9}$$

Assuming the fields are monochromatic (i.e. CW) at the pump/harmonic frequency and setting $\tilde{\mathbf{P}}_{0,\mathrm{NL}} = 0$ for the unperturbed field reduces Eqn. B.9 to:

$$\nabla\cdot\mathbf{F} = -i\omega\tilde{\mathbf{E}}_0(\mathbf{r},\omega)\cdot\tilde{\mathbf{P}}_{\mathrm{NL}}^*(\mathbf{r},\omega) \tag{B.10}$$

Substituting B.10 and B.6 into the reciprocity relation of Eqn. B.1, and taking the complex conjugate gives:

$$\frac{\partial}{\partial z}A_\nu(z,\omega) = \frac{i\omega}{4}\iint_\infty \tilde{\mathbf{E}}_0^*(\mathbf{r}_\perp,\omega)\cdot\tilde{\mathbf{P}}_{\mathrm{NL}}(\mathbf{r},\omega)dA \tag{B.11}$$

To find the time domain equivalent, both sides are multiplied by $\exp\left(-i(\omega_0-\omega)t\right)$ before taking their inverse Fourier transform to give:

$$\frac{\partial}{\partial z}A_\nu(z,t) = \frac{i\omega_0}{4}e^{-i(\beta_\nu z-\omega_0 t)}\iint_\infty \mathbf{E}_\nu^*(\mathbf{r}_\perp)\cdot\tilde{\mathbf{P}}_{\mathrm{NL}}(\mathbf{r},t)dA \tag{B.12}$$

where the corresponding unperturbed time domain electric fields have the time dependence $\exp(-i\omega_0 t)$:

$$\widetilde{\mathbf{E}}_0(\mathbf{r},t) = \mathbf{E}_\nu(\mathbf{r}_\perp)e^{i(\beta_\nu z-\omega_0 t)} + c.c. \tag{B.13}$$

Equation B.12 serves as a basic general first order differential equation describing the amplitudes' propagation. We now apply it to the specific case of third harmonic generation by considering a nonlinear polarisation $\tilde{\mathbf{P}}_{\mathrm{NL}}$ based on the third order nonlinearity:

$$\tilde{\mathbf{P}}_{\mathrm{NL}} = \frac{1}{2}\epsilon_0\chi^{(3)}_{xxxx}\left[(\tilde{\mathbf{E}}\cdot\tilde{\mathbf{E}}^*)\tilde{\mathbf{E}} + \frac{1}{2}(\tilde{\mathbf{E}}\cdot\tilde{\mathbf{E}})\tilde{\mathbf{E}}^*\right] \tag{B.14}$$

To obtain the full range of possible interactions between the pump and harmonic waves, we substitute into Eqn. B.14 a field which contains both frequencies. Strictly, this should be expressed as the summation of all possible supported modes, which would lead to large number of terms in Eqn. B.14. However, it is worth noting that due to non-degeneracy, any terms consisting of more than one type of mode will contain a phase matching requirement which is not satisfied, except for cross-phase modulation terms and intermodally phase matched third harmonic terms for which we assume $\beta_3 \approx 3\beta_1$ between only a specific pump mode (denoted henceforth as $\mu = 1$) and harmonic mode ($\mu = 3$). Also, a circularly symmetric microfibre is assumed so that nonlinear coupling between different polarisations of the same mode and frequency can be neglected. At this point, we therefore simplify this perturbed field:

$$\tilde{\mathbf{E}} = \mathbf{E}_1(\mathbf{r}_\perp)e^{i(\beta_1 z - \omega_1 t)} + \mathbf{E}_3(\mathbf{r}_\perp)e^{i(\beta_3 z - \omega_3 t)} + c.c. \tag{B.15}$$

To determine which phase matched terms with frequencies at ω_1 or ω_3 are of interest, we substitute Eqn. B.15 into the integrand $\tilde{\mathbf{E}}_0^* \cdot \mathbf{P}_{\mathrm{NL}}$ on the RHS of the reciprocity relation Eqn. B.12. We perform this firstly for the case when the perturbed and unperturbed fields represent the pump mode, i. e. $\tilde{\mathbf{E}}_0^* = \mathbf{E}_1^*$:

$$\begin{aligned} e^{-i(\beta_1 z - \omega_1 t)}\tilde{\mathbf{E}}_1^*.\tilde{\mathbf{P}}_{\mathrm{NL}} = \frac{1}{2}\epsilon_0\chi^{(3)}_{xxxx}\Bigg\{ & A_1|A_1|^4\left[|\mathbf{E}_1|^2 + \frac{1}{2}(\mathbf{E}_1)^2(\mathbf{E}_1^*)^2\right] \\ & + |A_3|^2 A_3\left[|\mathbf{E}_1.\mathbf{E}_3^*|^2 + |\mathbf{E}_1.\mathbf{E}_3|^2 + |\mathbf{E}_3|^2|\mathbf{E}_1|^2\right] \\ & + \frac{3}{2}(A_1^*)^2 A_3\left[(\mathbf{E}_1^*)^2(\mathbf{E}_3.\mathbf{E}_1^*)\right]e^{i(\beta_3 - 3\beta_1)z} \\ & + \text{other phase terms}\Bigg\} \end{aligned} \tag{B.16}$$

The first and second terms represent self and cross phase modulation respectively, which do not require phase matching, whilst the third term is responsible for THG and only becomes significant if $\beta_3 \approx 3\beta_1$. The remaining terms which are neglected, namely various four wave mixing terms, contain fast oscillating phase factors which are assumed to average out to zero. Repeating the same procedure with the harmonic field $\tilde{\mathbf{E}}_0^* = \tilde{\mathbf{E}}_3^*$ gives:

$$\begin{aligned} e^{-i(\beta_3 z - \omega_3 t)}\tilde{\mathbf{E}}_3^*.\tilde{\mathbf{P}}_{\mathrm{NL}} = \frac{1}{2}\epsilon_0\chi^{(3)}_{xxxx}\Bigg\{ & A_3|A_3|^4\left[|\mathbf{E}_3|^2 + \frac{1}{2}(\mathbf{E}_3)^2(\mathbf{E}_3^*)^2\right] \\ & + |A_1|^2 A_3\left[|\mathbf{E}_1^*.\mathbf{E}_3|^2 + |\mathbf{E}_1^*.\mathbf{E}_3^*|^2 + |\mathbf{E}_3|^2|\mathbf{E}_1|^2\right] \\ & + \frac{3}{2}A_1^3\left[(\mathbf{E}_1)^2(\mathbf{E}_1.\mathbf{E}_3^*)\right]e^{-i(\beta_3 - 3\beta_1)z} \\ & + \text{other phase terms}\Bigg\} \end{aligned} \tag{B.17}$$

Finally, integrating Eqns. B.16 and B.17 over the nonlinear microfibre cross-section, then substituting the results into the differential equation B.12 and applying the formula for nonlinear refractive index $n^{(2)} = (3/16)\epsilon_0\chi^{(3)}$ gives:

$$\frac{dA_1}{dz} = i\left(\frac{\epsilon_0}{\mu_0}\right)n^{(2)}k_1\left\{(J_1|A_1|^2 + 2J_2|A_3|^2)A_1 + J_3A_1^{*2}A_3e^{i\delta\beta z}\right\} \tag{B.18a}$$

$$\frac{dA_3}{dz} = i\left(\frac{\epsilon_0}{\mu_0}\right)n^{(2)}k_3\left\{(2J_4|A_1|^2 + J_5|A_3|^2)A_3 + J_3^*A_1^3e^{-i\delta\beta z}\right\} \tag{B.18b}$$

where the overlaps are integrated over the nonlinear cross section of the microfibre if it is surrounded in air:

$$J_1 = \frac{1}{3}\iint_{A_{NL}}\left(2|\mathbf{E}_1|^4 + |\mathbf{E}_1^2|^2\right)dA \tag{B.19a}$$

$$J_2 = \frac{1}{3}\iint_{A_{NL}}\left(|\mathbf{E}_1|^2|\mathbf{E}_3|^2 + |\mathbf{E}_1.\mathbf{E}_3|^2 + |\mathbf{E}_1.\mathbf{E}_3^*|^2\right)dA \tag{B.19b}$$

$$J_3 = \iint_{A_{NL}}\left((\mathbf{E}_1^*.\mathbf{E}_3)(\mathbf{E}_1^*)^2\right)dA \tag{B.19c}$$

$$J_3^* = J_3 \tag{B.19d}$$

$$J_4 = J_2^* = J_2 \tag{B.19e}$$

$$J_5 = \frac{1}{3}\iint_{A_{NL}}\left(2|\mathbf{E}_3|^4 + |\mathbf{E}_3^2|^2\right)dA \tag{B.19f}$$

These equations are equivalent to those reported in reference [17], although the electric fields there were normalised to the vacuum impedance i. e. $A_i(z,t) \rightarrow A_i(z,t)\sqrt{\epsilon_0/\mu_0}$, so the coefficient of (ϵ_0/μ_0) from Eqn. B.18 does not appear.

B.2 Determination of non-zero pump-harmonic overlaps

To ascertain which harmonic modes experience a non-zero J_3 overlap integral with the fundamental pump mode, we divide the integration area (i. e. the microfibre cross section) into a series of infinitely thin rings with width δr. From the field distributions in Eqns. 2.8, 2.11 and 2.12, the individual (r, ϕ, z) components of each mode are expressible in the separable form $E(r,\theta) = f(r)\sin(\nu\theta)$ or $f(r)\cos(\nu\theta)$ where ν is the azimuthal mode order number. For the fundamental pump, $\nu = 1$, whereas for the harmonic it will vary depending on the type of mode. Therefore, within each ring, the value of the integral for each component may be written as:

$$\delta J_3 = C(r)r\delta r\int_{-\pi}^{\pi}\sin^3(\theta)\sin(\nu(\theta+\Delta))d\theta \tag{B.20}$$

where Δ is the relative rotation angle between the pump and harmonic fields, and $C(r)r\delta r$ is constant along the ring (alternatively, cosine rather than sine functions can be used in the integrand). For TE and TM modes, the situation is trivial since the distributions of both modes are independent of θ, which implies $\nu = 0$ and so $\delta J_3 = 0$ since the integrand is an odd function of θ. It follows that the total value of $J_3 = \sum \delta J_3$ is identically zero for all transverse electric and magnetic third harmonic modes.

For harmonic hybrid modes with $\nu = 1$, applying trigonometric product-to-sum identities to the annular integral gives:

$$\begin{aligned}\delta J_3 &= C(r)r\delta r \int_{-\pi}^{\pi} \sin^3(\theta)\sin(\theta+\Delta)d\theta \\ &= C(r)r\delta r \frac{1}{32}\Big[2\sin(-2\theta+\Delta) - 6\sin(2\theta+\Delta) + \sin(4\theta+\Delta) + 12\theta\cos(\Delta)\Big]_{\theta=-\pi}^{\theta=\pi} \\ &= C(r)r\delta r \frac{3}{4}\pi\cos(\Delta)\end{aligned} \tag{B.21}$$

which confirms that the harmonic shares an overlap with the pump. Furthermore, it is evident that the overlap is largest when the two mode's polarisations are aligned so that $\Delta = 0$ or π rad, but will fall to zero the harmonic is rotated by $\Delta = \pm\pi/2$ rad. Similarly, the overlap for $\nu = 3$ hybrid modes is also non-zero:

$$\begin{aligned}\delta J_3 &= C(r)r\delta r \int_{-\pi}^{\pi} \sin^3(\theta)\sin(3\theta+\Delta)d\theta \\ &= C(r)r\delta r \frac{1}{96}\Big[18\sin(2\theta+\Delta) - 9\sin(4\theta+\Delta) + 2\sin(6\theta+\Delta) - 12\theta\cos(\Delta)\Big]_{\theta=-\pi}^{\theta=\pi} \\ &= C(r)r\delta r \frac{1}{4}\pi\cos(\Delta)\end{aligned} \tag{B.22}$$

For all other hybrid modes, the integral is evaluated from the more general form:

$$\begin{aligned}\delta J_3 &= C(r)r\delta r \int_{-\pi}^{\pi} \sin^3(\theta)\sin(\nu\theta+\Delta)d\theta \\ &= C(r)r\delta r \frac{1}{8}\Big[-\frac{\sin[(\nu-3)\theta+\Delta]}{\nu-3} + \frac{3\sin[(n-1)\theta+\Delta]}{n-1} \\ &\qquad - \frac{3\sin[(\nu+1)\theta+\Delta]}{\nu+1} + \frac{\sin[(\nu+3)\theta+\Delta]}{\nu+3}\Big]_{\theta=-\pi}^{\theta=\pi} \\ &= 0 \qquad (\nu \neq 1, 3)\end{aligned} \tag{B.23}$$

which proves that the only harmonic modes with a non-zero overlaps are the $\nu = 1, 3$ hybrid modes. Note that the presence of $(\nu - 1)$ and $(\nu - 3)$ in the denominators invalidates the above equation for the case of $\nu = 1, 3$; hence the reason for treating them separately earlier.

Appendix C

Solving the Microcoil Differential Equations

C.1 Overview

Two methods for solving the OMR differential equations are explained below:

1. The iterative Runge Kutta (RK) technique.
2. The modified Newton method [30].

The first algorithm adopts a more straightforward and intuitive approach, whilst the second is more complex but converges far quicker. In the simulations described in Chapter 6, the Newton method is used, but since this technique itself requires performing some RK iterations, we shall describe both numerical methods here.

For the following explanations, it is convenient to express the microcoil coupled mode differential equations and boundary conditions (Eqns. 6.1 and 6.4) in matrix form as:

$$\frac{d}{ds}\boldsymbol{A}(s) = \boldsymbol{C} \cdot \boldsymbol{A}(s) \tag{C.1a}$$

$$\boldsymbol{A}(0) = \boldsymbol{B} \cdot \boldsymbol{A}(L) + \boldsymbol{A}_{in} \tag{C.1b}$$

where $\boldsymbol{A}$ and $\boldsymbol{C}$ are the amplitude vector and coupling matrix respectively, whilst the input $\boldsymbol{B}$ is a matrix containing the phases accumulated from each turn. The input amplitude vector $\boldsymbol{A}_{in}$ is only non-zero for the elements corresponding to the first turn.

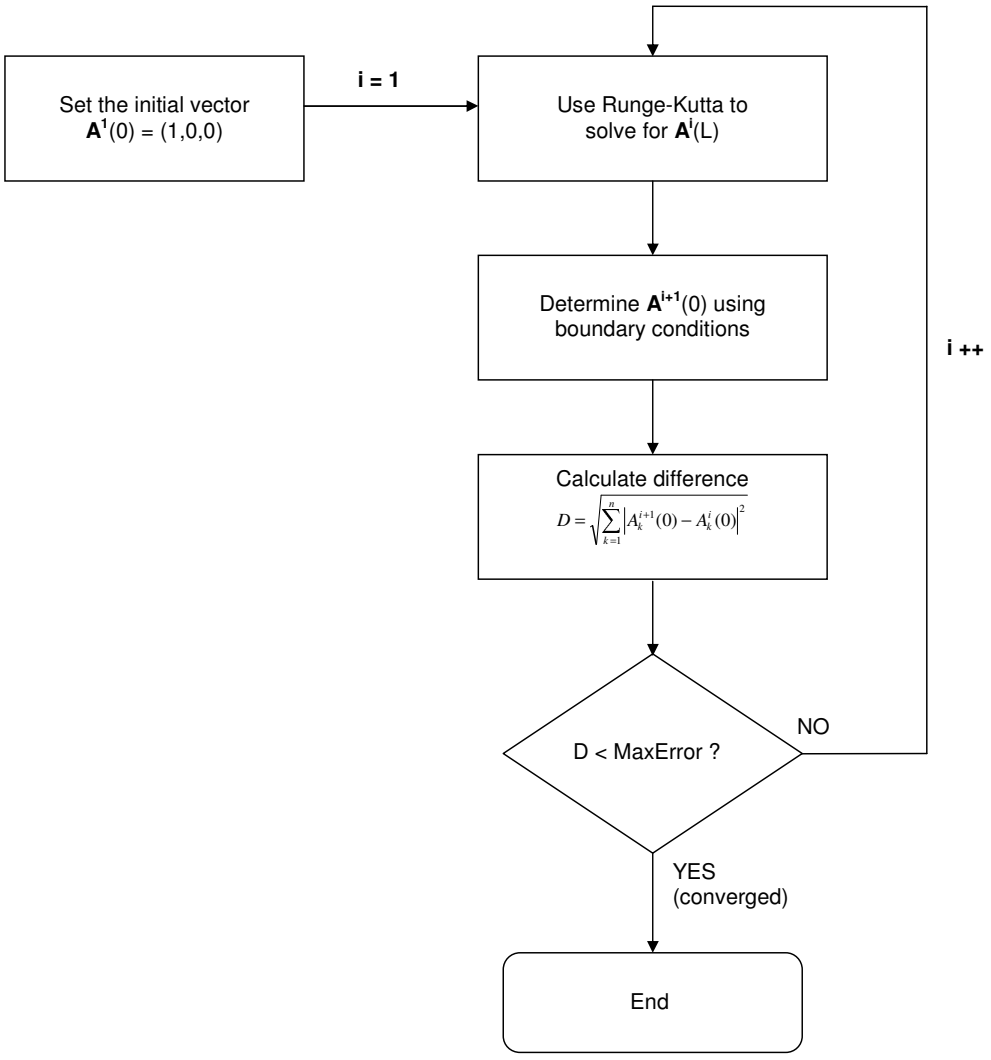

FIGURE C.1: Solving coupled mode microcoil ODEs by repeated Runge-Kutta iteration.

C.2 Iterative Runge Kutta method

The simplest procedure for solving these ODEs is outlined in Fig. C.1. First, the value of $\boldsymbol{A}(0)$ is initialised to a start vector of $(1, 0, \ldots, 0)$, and the ODEs are numerically integrated using the Runge-Kutta (RK) method to obtain the amplitudes $\boldsymbol{A}(L)$. Physically, the resulting $\boldsymbol{A}(s)$ solution would be similar to that obtained after allowing the light to propagate through one round trip. It follows that to obtain the steady solution, further RK iterations need to be undertaken until convergence, with the start vector updated according to Eqn. 6.4 after each iteration.

Once the difference between $\boldsymbol{A}(0)$ values from successive iterations falls below 10^{-5}, the simulation assumes the solution has converged and repeats the process for the next

wavelength. By extrapolating from the converged $\boldsymbol{A}(0)$ values of the previous three wavelengths, a start vector closer to the solution for the next wavelength can be found, and usually 30% fewer RK iterations are needed. In this way the transmission spectrum of the microcoil can be built up.

This method is consistently stable (in the absence of gain), and when the spectrum contains low Q, weak resonances, convergence can be attained within <100 iterations using MATLAB. However, if there are strong resonances (>10 dB extinction ratio) or if there are many turns the simulation tends to run far slower and may require up to $10^2 - 10^3$ iterations before convergence. The physical basis behind this is that for deeper resonances, the light is 'trapped' longer inside the coil and thus experiences a greater effective path length within the coil, so more iterations are needed.

C.3 Iterative modified Newton method

To improve the convergence rate, the Newton method illustrated in Fig. C.2 was implemented [30]. This technique is based on finding the value of $\boldsymbol{A}(0)$ which minimises the difference vector $\boldsymbol{R}(\boldsymbol{A}(0))$:

$$\begin{pmatrix} r_1(\boldsymbol{A}(0)) \\ r_j(\boldsymbol{A}(0)) \\ \vdots \\ r_n(\boldsymbol{A}(0)) \end{pmatrix} = \begin{pmatrix} A_1^{i+1}(0) \\ A_j^{i+1}(0) \\ \vdots \\ A_n^{i+1}(0) \end{pmatrix} - \begin{pmatrix} A_1^{i}(0) \\ A_j^{i}(0) \\ \vdots \\ A_n^{i}(0) \end{pmatrix} \tag{C.2}$$

where the values of $\boldsymbol{A}^{i+1}(0)$ are those obtained after one iteration of RK using $\boldsymbol{A}^{i}(0)$ as the start vector. Fig. C.3 explains how the zero for one element of $\boldsymbol{R}$ can be found by repeatedly iterating the Newton method from a nearby start point. r_j would of course depend on all the elements of $\boldsymbol{A(0)}$, although only one can be shown in the diagram. Furthermore, unlike the standard Newton method for a scalar function, here all elements of $\boldsymbol{R}$ must be simultaneously minimised by choosing an appropriate direction of descent $-\boldsymbol{\Delta A}$ to add to the current $\boldsymbol{A(0)}$:

$$\boldsymbol{A}^{k+1} = \boldsymbol{A}^{k} - \boldsymbol{\Delta A} \tag{C.3}$$

Since the amplitudes are complex valued, the corresponding direction vector for the real and imaginary parts must be treated separately. Thus, for an OMR of n turns, there will be $2(n-1)$ equations represented in Eqn. C.3 (the input to the first coil is already known and fixed). The direction $-\boldsymbol{\Delta A}$ is found from solving the simultaneous equations:

$$\boldsymbol{J} \cdot \boldsymbol{\Delta A} = \boldsymbol{R} \tag{C.4}$$

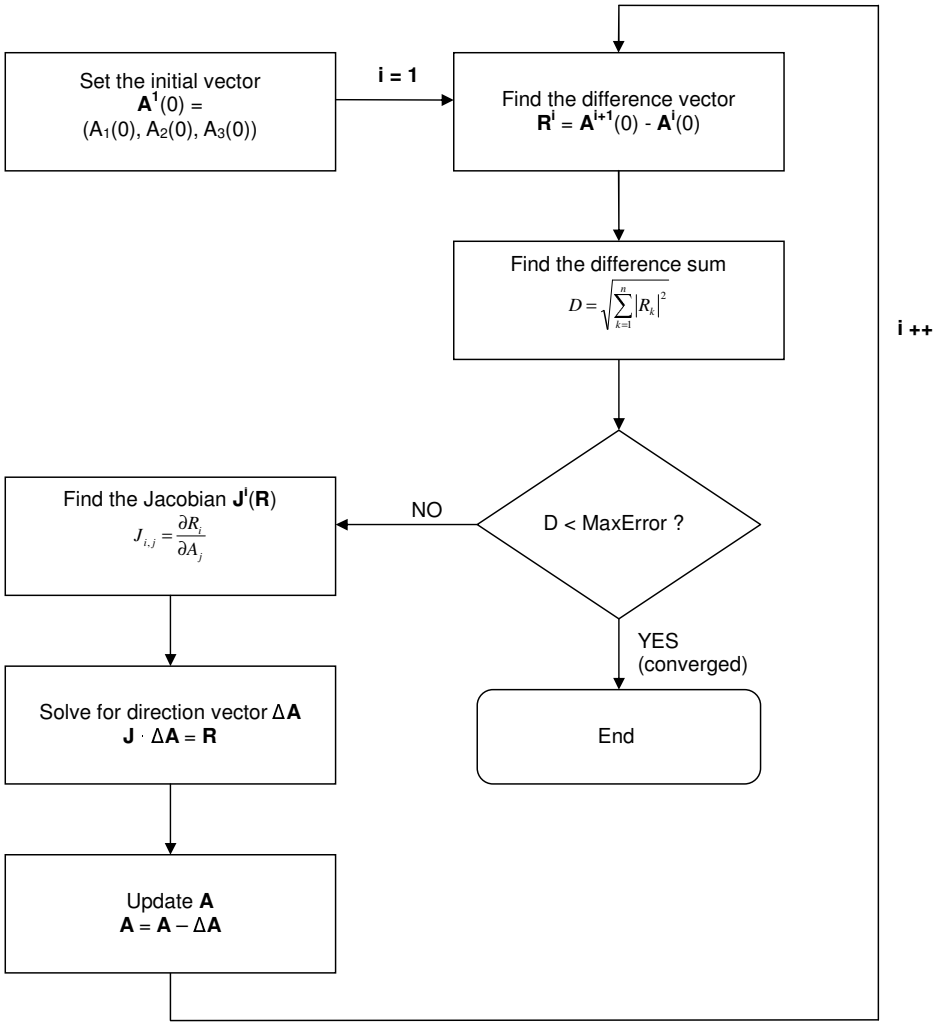

FIGURE C.2: Solving coupled mode microcoil ODEs by Newton method.

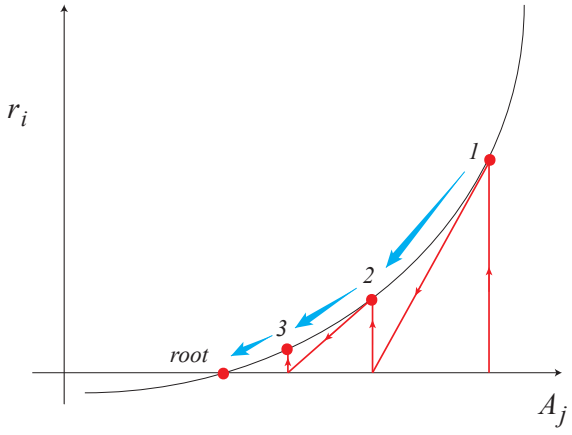

FIGURE C.3: Use of Newton method to find solution for r_i. N.B: r_i will actually depend on n variables $A_1 \ldots A_n$, although only one dimension is shown here.

where the values of $\boldsymbol{R}$ and the Jacobian matrix $\boldsymbol{J}$ are both evaluated at $\boldsymbol{A}(0) = \boldsymbol{A}^k$. Here, the Jacobian is a square matrix of numerically-computed first derivatives given by:

$$\boldsymbol{J}(\boldsymbol{R}) = \begin{pmatrix} \frac{\partial r_1}{\partial A_1} & \frac{\partial r_1}{\partial A_2} & \cdots & \frac{\partial r_1}{\partial A_n} \\ \frac{\partial r_2}{\partial A_1} & \frac{\partial r_2}{\partial A_2} & \cdots & \frac{\partial r_2}{\partial A_n} \\ \vdots & \vdots & & \vdots \\ \frac{\partial r_n}{\partial A_1} & \frac{\partial r_n}{\partial A_2} & \cdots & \frac{\partial r_n}{\partial A_n} \end{pmatrix} \tag{C.5}$$

(the actual Jacobian would have the real and imaginary parts of A_i and r_j and also their x and y amplitude components as separate variables, but here they are shown combined simply for clarity).

When solving the nonlinear equations as in section 6.3, simply stepping through and solving for an array of input amplitudes will almost certainly miss some solutions if the system is bistable, since the technique will generally converge to whichever solution is closest to the start vector. Instead, rather than stepping through different input amplitudes to find the hysteresis curve, we solve through a continuous range of stored microcoil energies E in order to obtain the complete transfer characteristic. To ensure that the Newton method converges to the desired stored energy, in the difference vector $\mathbf{R}$ we include an element $r_1(E) = E - E_0$, where E_0 is the target energy, since the Newton method must simultaneously minimise all elements of $\mathbf{R}$. The energy is defined by summing the powers in each turn:

$$E = \sum_{j=1}^{n} \left[\int_{s=0}^{L} |A_j^x(s)|^2 + |A_j^y(s)|^2 ds \right] \tag{C.6}$$

Incrementing and solving through an appropriate range of E_0 values produces the full hysteresis loop, including both stable states and the intermediate unstable state when the transfer characteristic is multi-valued.

Note that RK iterations still need to be performed using the Newton method, to obtain a suitable initial vector and also to evaluate values for $\boldsymbol{R}$. Nonetheless, this technique is superior to the RK looping method in terms of speed, and typically converges in a few dozen iterations rather than several hundred. Although there are more advanced methods which convergence in fewer iterations by computing the second derivatives of $\boldsymbol{R}$ to determine an improved direction vector [109], calculating the Hessian matrix would need 4 RK iterations per element which places a much greater workload on the algorithm with little benefit.

Appendix D

List of Publications

D.1 Journal articles

(1) M. A. Gouveia†, T. Lee†, R. Ismaeel†, M. Ding, N. G. R. Broderick, C. Cordeiro, and G. Brambilla, "Second harmonic generation and enhancement in microfibers and loop resonators," Appl. Phys. Lett. **102**, 201120 (2013). †Shared first authorship.

(2) P. Wang†, M. Ding†, T. Lee†, G. S. Murugan†, L. Bo, Y. Semenova, Q. Wu, D. W. Hewak, G. Brambilla, and G. Farrell, "Packaged chalcogenide microsphere resonator with high Q-factor," Appl. Phys. Lett. **102**, 131110 (2013). †Shared first authorship.

(3) T. Lee, N. G. R. Broderick, and G. Brambilla, "Resonantly enhanced third harmonic generation in microfiber loop resonators," J. Opt. Soc. Am. B **30**(3), 505–511 (2013).

(4) S. Afshar, M. A. Lohe, T. Lee, T. M. Monro, and N. G. R. Broderick, "Efficient third and one-third harmonic generation in nonlinear waveguides," Opt. Lett. **38**(3), 329–331 (2013).

(5) P. Wang, C. C. O'Mahony, T. Lee, R. Ismaeel, T. Hawkins, Y. Semenova, L. Bo, Q. Wu, C. McDonagh, G. Farrell, J. Ballato, and G. Brambilla, "Mid-infrared Raman sources using spontaneous Raman scattering in germanium core optical fibers," Appl. Phys. Lett. **102**(1), 011111 (2013).

(6) P. Wang, G. Brambilla, M. Ding, T. Lee, L. Bo, Y. Semenova, Q. Wu, and G. Farrell, "An enhanced refractometer based on periodically tapered small core singlemode fiber," IEEE J. Sens. **13**(1) 180–185 (2013).

(7) R. Ismaeel, T. Lee, M. Ding, M. Belal, and G. Brambilla, "Optical microfiber passive components," Laser & Photon. Rev. **7**(3), 350–384 (2013).

(8) R. Ismaeel†, T. Lee†, M. Ding, N. G. R. Broderick, and G. Brambilla, "Nonlinear microfiber loop resonators for resonantly enhanced third harmonic generation," Opt. Lett. **37**(24), 5121–5123 (2012). †Shared first authorship.

(9) T. Lee, N. G. R. Broderick, and G. Brambilla, "Nonlinear polarisation effects in optical microcoil resonators with fibre twist and birefringence," Opt. Commun. **285**(23), 4670–4676 (2012). Special Issue: Optical Micro/nanofibers: Challenges and Opportunities. Invited paper.

(10) G. Y. Chen, T. Lee, X. L. Zhang, G. Brambilla, and T. P. Newson, "Temperature compensation techniques for resonantly enhanced sensors and devices based on optical microcoil resonators," Opt. Commun. **285**(23), 4677–4683 (2012). Special Issue: Optical Micro/-nanofibers: Challenges and Opportunities. Invited paper.

(11) P. Wang, G. S. Murugan, T. Lee, M. Ding, G. Brambilla, Y. Semenova, Q. Wu, F. Koizumi, and G. Farell, "High-Q bismuth-silicate nonlinear glass microsphere resonators," IEEE J. Photon. **4**(3) 1013–1020 (2012).

(12) G. Y. Chen, T. Lee, R. Ismaeel, G. Brambilla, and T. P. Newson, "Resonantly enhanced Faraday rotation in a microcoil current sensor," IEEE Photon. Technol. Lett. **24**(10), 860–862 (2012).

(13) R. Ismaeel, T. Lee, F. Al-Saab, Y. Jung, and G. Brambilla, "A self-coupling multi-port microcoil resonator," Opt. Express **20**(8), 8568–8574 (2012).

(14) T. Lee, Y. Jung, C. A. Codemard, M. Ding, N. G. R. Broderick, and G. Brambilla, "Broadband third harmonic generation in tapered silica fibres," Opt. Express **20**(7), 8503–8511 (2012).

(15) P. Wang, T. Lee, M. Ding, A. Dhar, T. Hawkins, P. Foy, Y. Semenova, Q. Wu, J. K. Sahu, G. Farrell, J. Ballato, and G. Brambilla, "Germanium microsphere high-Q-resonator," Opt. Lett. **37**(4), 728-730 (2012).

(16) T. Lee, N. G. R. Broderick, and G. Brambilla, "Berry phase magnification in optical microcoil resonators," Opt. Lett. **36**(15), 2839–2841 (2011).

(17) M. Ding, P. Wang, T. Lee, and G. Brambilla, "A microfiber cavity with minimal-volume confinement," Appl. Phys. Lett. **99**, 051105 (2011).

(18) P. Wang, G. S. Murugan, T. Lee, X. Feng, Y. Semenova, Q. Wu, W. Loh, G. Brambilla, J. S. Wilkinson, and C. Farrell, "Lead silicate glass microsphere resonators with absorption-limited Q," Appl. Phys. Lett. **98**(18), 181105 (2011).

(19) T. Lee, N. G. R. Broderick, and G. Brambilla, "Transmission properties of microcoils based on twisted birefringent fibre," Opt. Commun. **284**(7), 1837–1841 (2010).

D.2 Conference papers

(1) T. Lee, M. I. M. Abdul Khudus, R. Ismaeel, C. A. Codemard, N. G. R. Broderick, and G. Brambilla, "$\chi^{(3)}$ processes in high numerical aperture optical fibres and fibre tapers," ECOC, London, 22–26 Sept 2013.

(2) M. I. M. Khudus, T. Lee, Q. H. Lam, M. S. Xuguang, P. P. Shum, and G. Brambilla, "UV and IR light generation in silica-based optical fibre tapers," ICMAT, Singapore, 30 June – 5 July 2013.

(3) R. Ismaeel, T. Lee, M. A. Gouveia, and G. Brambilla, "Enhanced second harmonic generation in microfiber loop resonators," CLEO/Europe-IQEC, Munich, 12–16 May 2013, CK–4.6.

(4) T. Lee, N. G. R. Broderick, R. Ismaeel, M. Gouveia, and G. Brambilla, "Resonantly enhanced second and third harmonic generation in microfibre loop resonators," CLEO/Europe-IQEC, Munich, 12–16 May 2013, CK-P.14.

(5) N. G. R. Broderick, M. A. Lohe, T. Lee, S. Afshar, and T. Monro, "Efficient third harmonic generation in photonic nanowires," Nanometa, Seefeld, Tirol, 3–6 Jan 2013, SAT5f.37.

(6) G. Y. Chen, T. Lee, R. Ismaeel, M. Belal, T. P. Newson, and G. Brambilla, "Optical microfiber sensors for the detection of current pulses," OSA Sensors, Monterey, CA, 24–28 June 2012, JW2A.3. Invited.

(7) G. Y. Chen, X. L. Zhang, T. Lee, G. Brambilla, and T. P. Newson, "Compact flexural disc accelerometers based on optical microfiber," OFS-22, Beijing, October 2012.

(8) T. Lee, Y. Jung, C. A. Codemard, M. Ding, N. G. R. Broderick, and G. Brambilla, "Silica microfibres for broadband third harmonic generation," CLEO/QELS, San Jose, 6–11 May 2012, CW1A.7.

(9) R. Ismaeel, T. Lee, F. Al-Saab, Y. Jung, and G. Brambilla, "A multi-port optical microfiber coil resonator," CLEO/QELS, San Jose, 6–11 May 2012.

(10) M. Ding, M. Belal, G. Y. Chen, R. Ismaeel, T. Lee, Y. Jung, P. Wang, X. Zhang, Z. Song, F. Xu, R. Lorenzi, T. Newson, and G. Brambilla, "Optical microfibre passive devices and sensors," Proceedings of the SPIE 2011 Vol.8307: Passive Components and Fiber-Based Devices VIII, Shanghai, 14–16 Nov 2011, 83070Y. Invited paper.

(11) M. Ding, M. Belal, G. Y. Chen, R. Al-Azawi, T. Lee, Y. Jung, P. Wang, X. L. Zhang, Z. Q. Song, F. Xu, R. Lorenzi, T. P. Newson, and G. Brambilla, "Optical microfiber devices and sensors," Asia Communications and Photonics Conference and Exhibition (ACP), Shanghai, 13–16 Nov 2011.

(12) M. Ding, P. Wang, T. Lee, and G. Brambilla, "Focused ion beam engraved phase-shifted Bragg grating microcavity resonator," MediNano4, Rome, 24–25 Oct 2011. Postdeadline.

(13) T. Lee, Y. Jung, C. A. Codemard, G. Brambilla, and N. G. R. Broderick, "Third harmonic generation in silica microfibers," NLO, Kauai, Hawaii, 17–22 July 2011, NTuD7.

(14) T. Lee, N. G. R. Broderick, and G. Brambilla, "Polarisation effects in optical microcoil resonators," IQEC/CLEO Pacific Rim, Sydney, 29 Aug – 1 Sep 2011.

(15) N. G. R. Broderick, G. Brambilla, and T. Lee, "Berry phase magnification and other polarisation effects in nonlinear microcoil resonators," IEEE Photonics Conference (PHO), 9–13 Oct. 2011, MI1.

(16) N. G. R. Broderick, M. A. Lohe, T. Lee, and S. Afshar, "Analytic theory of two wave interactions in a waveguide with a $\chi^{(3)}$ nonlinearity," IQEC/CLEO Pacific Rim, Sydney, 29 Aug – 1 Sep 2011.

(17) T. Lee, N. G. R. Broderick, and G. Brambilla, "Polarisation effects in nonlinear microcoils," CLEO/Europe-EQEC, Munich, 22–26 May 2011.

(18) G. Y. Chen, T. Lee, Y. Jung, M. Belal and G. Brambilla, N. G. R. Broderick, and T. P. Newson, "Investigation of thermal effects on embedded microcoil resonators," CLEO/Europe-EQEC, Munich, 22–26 May 2011.

(19) T. Lee, N. G. R. Broderick, and G. Brambilla, "Berry's phase magnification in microcoil resonators," CLEO/Europe-EQEC, Munich, 22–26 May 2011.

(20) T. Lee, N. G. R. Broderick, and G. Brambilla, "Polarization effects in microcoil resonators," Photon-10, Southampton, 23–26 August 2010.

References

[1] R. Ismaeel, T. Lee, M. Ding, M. Belal, and G. Brambilla, "Optical microfiber passive components," Laser & Photon. Rev. **7**, 350–384 (2013).

[2] M. A. Gouveia, T. Lee, R. Ismaeel, M. Ding, N. G. R. Broderick, C. M. B. Cordeiro, and G. Brambilla, "Second harmonic generation and enhancement in microfibers and loop resonators," Appl. Phys. Lett. **102**, 201 120 (2013).

[3] S. Afshar, M. A. Lohe, T. Lee, T. M. Monro, and N. G. R. Broderick, "Efficient third and one-third harmonic generation in nonlinear waveguides," Opt. Lett. **38**, 329–331 (2013).

[4] T. Lee, Y. Jung, C. A. Codemard, M. Ding, N. G. R. Broderick, and G. Brambilla, "Broadband third harmonic generation in tapered silica fibres," Opt. Express **20**, 8503–8511 (2012).

[5] R. Ismaeel, T. Lee, M. Ding, N. G. R. Broderick, and G. Brambilla, "Nonlinear microfiber loop resonators for resonantly enhanced third harmonic generation," Opt. Lett. **37**, 5121–5123 (2012).

[6] T. Lee, N. G. R. Broderick, and G. Brambilla, "Nonlinear polarisation effects in optical microcoil resonators with fibre twist and birefringence," Opt. Commun. **285**, 4670–4676 (2012), special issue: Optical micro/nanofibers: Challenges and Opportunities.

[7] T. Lee, N. G. Broderick, and G. Brambilla, "Transmission properties of microcoils based on twisted birefringent fibre," Opt. Commun. **284**, 1837–1841 (2011).

[8] T. Lee, N. G. R. Broderick, and G. Brambilla, "Berry phase magnification in optical microcoil resonators," Opt. Lett. **36**, 2839–2841 (2011).

[9] R. R. Gattass, G. T. Svacha, L. Tong, and E. Mazur, "Supercontinuum generation in submicrometer diameter silica fibers," Opt. Express **14**, 9408–9414 (2006).

[10] S. Leon-Saval, T. Birks, W. Wadsworth, P. Russell, and M. Mason, "Supercontinuum generation in submicron fibre waveguides," Opt. Express **12**, 2864–2869 (2004).

[11] A. Coillet, G. Vienne, and P. Grelu, "Potentialities of glass air-clad micro-and nanofibers for nonlinear optics," J. Opt. Soc. Am. B **27**, 394–401 (2010).

[12] S. Richard, "Second-harmonic generation in tapered optical fibers," J. Opt. Soc. Am. B **27**, 1504–1512 (2010).

[13] J. Lægsgaard, "Theory of surface second-harmonic generation in silica nanowires," J. Opt. Soc. Am. B **27**, 1317–1324 (2010).

[14] U. Wiedemann, K. Karapetyan, C. Dan, D. Pritzkau, W. Alt, S. Irsen, and D. Meschede, "Measurement of submicrometre diameters of tapered optical fibres using harmonic generation," Opt. Express **18**, 7693–7704 (2010).

[15] D. Akimov, A. Ivanov, A. Naumov, O. Kolevatova, M. Alfimov, T. Birks, W. Wadsworth, P. Russell, A. Podshivalov, and A. Zheltikov, "Generation of a spectrally asymmetric third harmonic with unamplified 30-fs Cr:forsterite laser pulses in a tapered fiber," Appl. Phys. B: Lasers and Optics **76**, 515–519 (2003).

[16] V. Grubsky and J. Feinberg, "Phase-matched third-harmonic UV generation using low-order modes in a glass micro-fiber," Opt. Commun. **274**, 447–450 (2007).

[17] V. Grubsky and A. Savchenko, "Glass micro-fibers for efficient third harmonic generation," Opt. Express **13**, 6798–6806 (2005).

[18] A. Coillet and P. Grelu, "Third-harmonic generation in optical microfibers: From silica experiments to highly nonlinear glass prospects," Opt. Commun. **285**, 3493–3497 (2012), special issue: Sub-wavelength Light Localization and Focusing.

[19] S. Afshar and T. M. Monro, "A full vectorial model for pulse propagation in emerging waveguides with subwavelength structures part I: Kerr nonlinearity," Opt. Express **17**, 2298–2318 (2009).

[20] C. Caspar and E. J. Bachus, "Fibre-optic micro-ring-resonator with 2 mm diameter," Electron. Lett. **25**, 1506–1508 (1989).

[21] M. Sumetsky, Y. Dulashko, J. Fini, A. Hale, and D. DiGiovanni, "The microfiber loop resonator: Theory, experiment, and application," J. Lightwave Technol. **24**, 242–250 (2006).

[22] X. Jiang, L. Tong, G. Vienne, X. Guo, A. Tsao, Q. Yang, and D. Yang, "Demonstration of optical microfiber knot resonators," Appl. Phys. Lett. **88**, 223 501 (2006).

[23] M. Sumetsky, "Optical fiber microcoil resonators," Opt. Express **12**, 2303–2316 (2004).

[24] G. Agrawal, *Nonlinear Fiber Optics* (Academic Press, San Diego, 2006), 4^{th} edn.

[25] P. Guyot-Sionnest and Y. Shen, "Bulk contribution in surface second-harmonic generation," Phys. Rev. B **38**, 7985–7989 (1988).

[26] F. J. Rodriguez, F. X. Wang, and M. Kauranen, "Calibration of the second-order nonlinear optical susceptibility of surface and bulk of glass," Opt. Express **16**, 8704–8710 (2008).

[27] F. Xu and G. Brambilla, "Demonstration of a refractometric sensor based on optical microfiber coil resonator," Appl. Phys. Lett. **92**, 101 126 (2008).

[28] N. G. R. Broderick and T. Ng, "Theoretical study of noise reduction of NRZ signals using nonlinear broken micro-coil resonators," IEEE Photon. Technol. Lett. **21**, 444–446 (2009).

[29] M. Sumetsky, "Uniform coil optical resonator and waveguide: transmission spectrum, eigenmodes, and dispersion relation," Opt. Express **13**, 4331–4340 (2005).

[30] N. G. R. Broderick, "Optical Snakes and Ladders: Dispersion and nonlinearity in microcoil resonators," Opt. Express **16**, 16 247–16 254 (2008).

[31] A. Snyder and J. Love, *Optical Waveguide Theory* (Springer, New York, 1983), 1st edn.

[32] K. Okamoto, *Fundamentals of Optical Waveguides* (Academic Press, San Diego, 2006), 2nd edn.

[33] H. Yu, S. Wang, J. Fu, M. Qiu, Y. Li, F. Gu, and L. Tong, "Modeling bending losses of optical nanofibers or nanowires," Appl. Opt. **48**, 4365–4369 (2009).

[34] Y. Jung, G. Brambilla, and D. J. Richardson, "Comparative study of the effective single mode operational bandwidth in sub-wavelength optical wires and conventional single-mode fibers," Opt. Express **17**, 16 619–16 624 (2009).

[35] Y. Jung, G. Brambilla, and D. J. Richardson, "Broadband single-mode operation of standard optical fibers by using a sub-wavelength optical wire filter," Opt. Express **16**, 14 661–14 667 (2008).

[36] F. Xu and G. Brambilla, "Preservation of micro-optical fibers by embedding," Jpn. J. Appl. Phys. **47**, 6675–6677 (2008).

[37] F. Xu and G. Brambilla, "Embedding optical microfiber coil resonators in Teflon," Opt. Lett. **32**, 2164–2166 (2007).

[38] F. Xu, V. Pruneri, V. Finazzi, and G. Brambilla, "An embedded optical nanowire loop resonator refractometric sensor," Opt. Express **16**, 1062–1067 (2008).

[39] J. Villatoro and D. Monzón-Hernández, "Fast detection of hydrogen with nano fiber tapers coated with ultra thin palladium layers," Opt. Express **13**, 5087–5092 (2005).

[40] R. Garcia-Fernandez, W. Alt, F. Bruse, C. Dan, K. Karapetyan, O. Rehband, A. Stiebeiner, U. Wiedemann, D. Meschede, and A. Rauschenbeutel, "Optical nanofibers and spectroscopy," Appl. Phys. B **105**, 3–15 (2011).

[41] A. Stiebeiner, O. Rehband, R. Garcia-Fernandez, and A. Rauschenbeutel, "Ultra-sensitive fluorescence spectroscopy of isolated surface-adsorbed molecules using an optical nanofiber," Opt. Express **17**, 21 704–21 711 (2009).

[42] L. Shi, Y. H. Xu, W. Tan, and X. F. Chen, "Simulation of optical microfiber loop resonators for ambient refractive index sensing," Sensors **7**, 689–696 (2007).

[43] J. Wo, G. Wang, Y. Cui, Q. Sun, R. Liang, P. P. Shum, and D. Liu, "Refractive index sensor using microfiber-based Mach–Zehnder interferometer," Opt. Lett. **37**, 67–69 (2012).

[44] L. Tong, R. R. Gattass, J. B. Ashcom, S. He, J. Lou, M. Shen, I. Maxwell, and E. Mazur, "Subwavelength-diameter silica wires for low-loss optical wave guiding," Nature **426**, 816–819 (2003).

[45] F. Kien, J. Liang, K. Hakuta, and V. Balykin, "Field intensity distributions and polarization orientations in a vacuum-clad subwavelength-diameter optical fiber," Opt. Commun. **242**, 445–455 (2004).

[46] M. D. Turner, T. M. Monro, and S. Afshar, "A full vectorial model for pulse propagation in emerging waveguides with subwavelength structures part II: Stimulated Raman Scattering," Opt. Express **17**, 11 565–11 581 (2009).

[47] S. Afshar, W. Zhang, and T. M. Monro, "Experimental confirmation of a generalized definition of the effective nonlinear coefficient in emerging waveguides with subwavelength structures," in *Conference on Lasers and Electro-Optics/International Quantum Electronics Conference* p. CThBB6 (2009).

[48] S. Afshar, W. Q. Zhang, H. Ebendorff-Heidepriem, and T. M. Monro, "Small core optical waveguides are more nonlinear than expected: experimental confirmation," Opt. Lett. **34**, 3577–3579 (2009).

[49] E. C. Magi, L. B. Fu, H. C. Nguyen, M. R. Lamont, D. I. Yeom, and B. J. Eggleton, "Enhanced Kerr nonlinearity in sub-wavelength diameter As2Se3 chalcogenide fiber tapers," Opt. Express **15**, 10 324–10 329 (2007).

[50] S. Afshar, M. A. Lohe, W. Q. Zhang, and T. M. Monro, "Full vectorial analysis of polarization effects in optical nanowires," Opt. Express **20**, 14 514–14 533 (2012).

[51] P. Klocek, *Handbook of infrared optical materials* (Marcel Dekker Inc., New York, 1991), 1st edn.

[52] G. Brambilla, F. Koizumi, V. Finazzi, and D. Richardson, "Supercontinuum generation in tapered bismuth silicate fibres," Electron. Lett. **41**, 795–797 (2005).

[53] L. Tong, J. Lou, E. Mazur, et al., "Single-mode guiding properties of subwavelength-diameter silica and silicon wire waveguides," Opt. Express **12**, 1025–1035 (2004).

[54] R. Boyd, *Nonlinear Optics* (Academic Press, San Diego, 2008), 3rd edn.

[55] G. I. Stegeman and R. H. Stolen, "Waveguides and fibers for nonlinear optics," J. Opt. Soc. Am. B **6**, 652–662 (1989).

[56] O. A. Kolevatova, A. N. Naumov, and A. M. Zheltikov, "Phase-matching conditions for third-harmonic generation revised to include group-delay effects and nonlinear phase shifts," Laser Phys. **13**, 1040–1045 (2003).

[57] M. Delgado-Pinar, Y. Li, D. M. Bird, T. A. Birks, and W. J. Wadsworth, "Third harmonic generation in uniform fibre nanotapers via intermodal coupling," in *Conference on Lasers and Electro-Optics* p. CWL4 (2010).

[58] M. Monerie, "Propagation in doubly clad single-mode fibers," IEEE Quantum Electron. **18**, 535–542 (1982).

[59] C. Y. H. Tsao, D. N. Payne, and W. A. Gambling, "Modal characteristics of three-layered optical fiber waveguides: a modified approach," J. Opt. Soc. Am. A **6**, 555–563 (1989).

[60] E. D. Palik, *Handbook of optical constants of solids* (Academic Press, New York, 1998), 1st edn.

[61] G. Brambilla, F. Xu, P. Horak, Y. Jung, F. Koizumi, N. Sessions, E. Koukharenko, X. Feng, G. Murugan, J. Wilkinson, et al., "Optical fiber nanowires and microwires: fabrication and applications," Adv. in Opt. and Photon. **1**, 107–161 (2009).

[62] T. Birks and Y. Li, "The shape of fiber tapers," J. Lightwave Technol. **10**, 432–438 (1992).

[63] P. Dumais, F. Gonthier, S. Lacroix, J. Bures, A. Villeneuve, P. Wigley, and G. Stegeman, "Enhanced self-phase modulation in tapered fibers," Opt. Lett. **18**, 1996–1998 (1993).

[64] M. A. Arbore, A. Galvanauskas, D. Harter, M. H. Chou, and M. M. Fejer, "Engineerable compression of ultrashort pulses by use of second-harmonic generation in chirped-period-poled lithium niobate," Opt. Lett. **22**, 1341–1343 (1997).

[65] J. S. Levy, M. A. Foster, A. L. Gaeta, and M. Lipson, "Harmonic generation in silicon nitride ring resonators," Opt. Express **19**, 11 415–11 421 (2011).

[66] Z. Yang, P. Chak, A. D. Bristow, H. M. van Driel, R. Iyer, J. S. Aitchison, A. L. Smirl, and J. E. Sipe, "Enhanced second-harmonic generation in AlGaAs microring resonators," Opt. Lett. **32**, 826–828 (2007).

[67] Z. F. Bi, A. W. Rodriguez, H. Hashemi, D. Duchesne, M. Loncar, K. M. Wang, and S. G. Johnson, "High-efficiency second-harmonic generation in doubly-resonant $\chi(2)$ microring resonators," Opt. Express **20**, 7526–7543 (2012).

[68] T. Carmon and K. J. Vahala, "Visible continuous emission from a silica microphotonic device by third-harmonic generation," Nat. Phys. **3**, 430–435 (2007).

[69] G. Vienne, Y. Li, L. Tong, and P. Grelu, "Observation of a nonlinear microfiber resonator," Opt. Lett. **33**, 1500–1502 (2008).

[70] N. G. R. Broderick, M. A. Lohe, T. Lee, and S. Afshar, "Analytic theory of two wave interactions in a waveguide with a $\chi(3)$ nonlinearity." in *Proceedings of the International Quantum Electronics Conference and Conference on Lasers and Electro-Optics Pacific Rim 2011* p. I366 (2011).

[71] N. Bloembergen, R. Chang, S. Jha, and C. Lee, "Optical second-harmonic generation in reflection from media with inversion symmetry," Phys. Rev. **174**, 813–822 (1968).

[72] P. Guyot-Sionnest, W. Chen, and Y. Shen, "General considerations on optical second-harmonic generation from surfaces and interfaces," Phys. Rev. B **33**, 8254–8263 (1986).

[73] R. Terhune and D. Weinberger, "Second-harmonic generation in fibers," J. Opt. Soc. Am. B **4**, 661–674 (1987).

[74] W. Margulis and U. Osterberg, "Second-harmonic generation in optical glass fibers," J. Opt. Soc. Am. B **5**, 312–316 (1988).

[75] N. Bloembergen and P. S. Pershan, "Light waves at the boundary of nonlinear media," Phys. Rev. **128**, 606–622 (1962).

[76] C. Wang and A. Duminski, "Second-harmonic generation of light at the boundary of alkali halides and glasses," Phys. Rev. Lett. **20**, 668–671 (1968).

[77] Y. Shen, "Optical second harmonic generation at interfaces," Annu. Rev. Phys. Chem. **40**, 327–350 (1989).

[78] R. A. Myers, N. Mukherjee, and S. R. J. Brueck, "Large second-order nonlinearity in poled fused silica," Opt. Lett. **16**, 1732–1734 (1991).

[79] J. Scheuer and M. Sumetsky, "Optical-fiber microcoil waveguides and resonators and their applications for interferometry and sensing," Laser & Photon. Rev. **5**, 465–478 (2011).

[80] P. Wang, T. Lee, M. Ding, A. Dhar, T. Hawkins, P. Foy, Y. Semenova, Q. Wu, J. Sahu, G. Farrell, J. Ballato, and G. Brambilla, "Germanium microsphere high-Q resonator," Opt. Lett. **37**, 728–730 (2012).

[81] P. Wang, G. S. Murugan, T. Lee, X. Feng, Y. Semenova, Q. Wu, W. Loh, G. Brambilla, J. S. Wilkinson, and G. Farrell, "Lead silicate glass microsphere resonators with absorption-limited Q," Appl. Phys. Lett. **98**, 181 105 (2011).

[82] M. Gorodetsky, A. Savchenkov, V. Ilchenko, et al., "Ultimate Q of optical microsphere resonators," Opt. Lett. **21**, 453–455 (1996).

[83] A. R. Nelson, "Coupling optical waveguides by tapers," Appl. Opt. **14**, 3012–3015 (1975).

[84] S. Dong, H. Ding, Y. Liu, and X. Qi, "Investigation of evanescent coupling between tapered fiber and a multimode slab waveguide," Appl. Opt. **51**, C152–C157 (2012).

[85] X. Jiang, Q. Song, L. Xu, J. Fu, and L. Tong, "Microfiber knot dye laser based on the evanescent-wave-coupled gain," Appl. Phys. Lett. **90**, 233 501 (2007).

[86] G. Wang, P. P. Shum, L. Tong, C. M. Li, and C. Lin, "Polarization effects in microfiber loop and knot resonators," IEEE Photon. Technol. Lett. **20**, 586–588 (2010).

[87] Y. Jung, G. Brambilla, G. S. Murugan, and D. J. Richardson, "Optical racetrack ring-resonator based on two U-bent microfibers," Appl. Phys. Lett. **98**, 021 109 (2011).

[88] G. Vienne, A. Coillet, P. Grelu, M. El Amraoui, J. Jules, F. Smektala, and L. Tong, "Demonstration of a reef knot microfiber resonator," Opt. Express **17**, 6224–6229 (2009).

[89] R. Ismaeel, T. Lee, F. Al-Saab, Y. Jung, and G. Brambilla, "A self-coupling multi-port microcoil resonator," Opt. Express **20**, 8568–8574 (2012).

[90] Y. Jung, G. Senthil Murugan, G. Brambilla, and D. Richardson, "Embedded Optical Microfiber Coil Resonator With Enhanced High-Q," IEEE Photon. Technol. Lett. **22**, 1638–1640 (2010).

[91] Y. Jung, G. Brambilla, K. Oh, and D. Richardson, "Highly birefringent silica microfiber," Opt. Lett. **35**, 378–380 (2010).

[92] H. Xuan, J. Ju, and W. Jin, "Highly birefringent optical microfibers," Opt. Express **18**, 3828–3839 (2010).

[93] Y. Jung, G. Brambilla, and D. J. Richardson, "Polarization-maintaining optical microfiber," Opt. Lett. **35**, 2034–2036 (2010).

[94] R. Ulrich and A. Simon, "Polarization optics of twisted single-mode fibers," Appl. Opt. **18**, 2241–2251 (1979).

[95] T. S. Narasimhamurty, *Photoelastic and Electro-Optic Properties of Crystals* (Plenum Press, New York, 1981), 1st edn.

[96] K. Huang, S. Yang, and L. Tong, "Modeling of evanescent coupling between two parallel optical nanowires," Appl. Opt. **46**, 1429–1434 (2007).

[97] M. V. Berry, "Interpreting the anholonomy of coiled light," Nature **326**, 277–278 (1987).

[98] R. Y. Chiao and Y. S. Wu, "Manifestations of Berry's topological phase for the photon," Phys. Rev. Lett. **57**, 933–936 (1986).

[99] A. Tomita and R. Y. Chiao, "Observation of Berry's topological phase by use of an optical fiber," Phys. Rev. Lett. **57**, 937–940 (1986).

[100] I. Golub, "Berry's phase amplification by a ring resonator," Opt. Lett. **31**, 3342–3344 (2006).

[101] I. Golub, T. Audet, and L. Imobekhai, "Observation of Berry's phase amplification by a ring resonator," J. Opt. Soc. Am. B **27**, 1698–1700 (2010).

[102] P. Senthilkumaran, G. Thursby, and B. Culshaw, "Fiber-optic tunable loop mirror using Berry's geometric phase," Opt. Lett. **25**, 533–535 (2000).

[103] R. Ulrich, S. C. Rashleigh, and W. Eickhoff, "Bending-induced birefringence in single-mode fibers," Opt. Lett. **5**, 273–275 (1980).

[104] H. M. Gibbs, *Optical Bistability: Controlling Light with Light* (Academic Press, San Diego, 1985), 1st edn.

[105] R. Cush and C. Kirkby, "Polarization bistability in a nonlinear birefringent Fabry-Perot cavity," Opt. Commun. **60**, 399–404 (1986).

[106] M. Corona, K. Garay-Palmett, and A. B. U'Ren, "Experimental proposal for the generation of entangled photon triplets by third-order spontaneous parametric downconversion in optical fibers," Opt. Lett. **36**, 190–192 (2011).

[107] M. Corona, K. Garay-Palmett, and A. B. U'Ren, "Third-order spontaneous parametric down-conversion in thin optical fibers as a photon-triplet source," Phys. Rev. A **84**, 033 823 (2011).

[108] Z. Ruan, G. Veronis, K. L. Vodopyanov, M. M. Fejer, and S. Fan, "Enhancement of optics-to-THz conversion efficiency by metallic slot waveguides," Opt. Express **17**, 13 502–13 515 (2009).

[109] J. Nocedal and S. Wright, *Numerical Optimization* (Springer, New York, 2006), 2nd edn.